UNIVERSITÄT GRAZ
UNIVERSITY OF GRAZ

Florian Koller, BSc

Stellar activity of late-type main-sequence stars in SDSS data

Master's Thesis

to achieve the university degree of

Master of Science

Master's degree programme: Physics

submitted to

University of Graz

Supervisor

Assoz. Prof. Mag. Dr.rer.nat. Manuela Temmer

Co - Supervisor
Mag. Dr.rer.nat. Martin Leitzinger

Institute for Physics
Head: Univ.-Prof. Dipl-Ing. Dr.techn. Martin Sterrer

Graz, November 2019

Abstract

The numerous detections of exoplanets in recent years lead to an increasing interest in habitability and the evolution of atmospheres of exoplanets, which are highly dependent on the stellar activity of their host star. Constraining parameters of stellar flares and stellar coronal mass ejections (CMEs) is crucial for evaluating thermal and non-thermal planetary atmosphere escape. Especially stellar CMEs have been so far detected very rarely. Their contribution to stellar mass and angular momentum loss remains up to now also unknown.
This work aims to search and classify flares and potential CMEs using optical spectra provided by the Sloan Digital Sky Survey (SDSS) Data release 14. The sample is constrained to all F, G, K and M main-sequence type stars, resulting in more than 630000 stars which translates to a total observing time of $\sim$ 120 years. This work makes use of the single component spectra provided by SDSS, yielding usually 3 – 5 exposures for a star with exposure times between 10 and 25 minutes. An automatic flare search is performed by detecting significant peak changes in the $H\alpha$ and $H\beta$ lines after fitting a Gaussian to the line core. CMEs are searched by identifying asymmetries in the Balmer lines arising due to the Doppler effect. 281 flares are identified on late type stars (K3 – M9 stars). 10 possible candidates for CMEs showing excess flux in Balmer line wings are presented as well as one possible CME showing blue wing absorption in $H\alpha$ only. All stars are crossmatched with the latest GAIA data release 2 data to infer stellar distances. Flaring energies in $H\alpha$ are calculated and masses of the CME candidates are estimated.
The reported $H\alpha$ flaring energies range from $10^{29} - 10^{33}$ erg. The detected $H\alpha$ flaring energy increases with earlier types, while the fraction of flaring times increases with later types. Mass estimations for the CME candidates are in the range of $10^{15} - 8 \times 10^{18}$ g with maximum projected velocities of $\sim 300 - 700$ km/s. The low detection rate of CMEs, as found in the present study, is in agreement with several other studies which tried to determine the CME frequency of late-type main-sequence stars.

Kurzfassung

Die zahlreichen Detektionen von Exoplaneten in den vergangenen Jahren führten zu einem steigenden Interesse bezüglich der Bewohnbarkeit sowie die Beschaffenheit und Entwicklung der Atmosphären dieser Planeten. Die Atmosphären werden maßgeblich von der stellaren Aktivität des Sternes beeinflusst. Um Abschätzungen bezüglich des thermischen und nicht-thermischen Atmosphärenverlustes von Exoplaneten zu treffen, ist es notwendig, stellare Flares und Coronale Massenauswürfe (coronal mass ejection, CMEs) zu parametrisieren. Stellare CMEs im speziellen wurden bislang nur selten detektiert, wodurch deren Beitrag zu stellarem Massen- und Drehimpulsverlust noch nicht geklärt ist.
Das Ziel dieser Arbeit ist die Suche und Klassifikation von Flares und CMEs in optischen Spektren der 14. Datenfreigabe des Sloan Digital Sky Survey (SDSS). Die Auswahl der Sterne wurde auf späte Hauptreihensterne der Typen F, G, K und M eingeschränkt, was zu einer Gesamtanzahl an über 630000 Sterne führte. Dies entspricht einer Gesamtobservationszeit von $\sim$ 120 Jahren. Die Einzelaufnahmen der SDSS Spektren wurden genutzt um zeitliche Entwicklungen zu detektieren. Die Anzahl der Einzelaufnahmen pro Stern beläuft sich für gewöhnlich auf 3 bis 5 Aufnahmen mit je 10 bis 25 Minuten Belichtungszeit. Für die Flare Suche wird ein automatischer Algorithmus angewendet, der signifikante Änderungen der Höhe der $H\alpha$ und $H\beta$ Linien detektiert, nachdem jeweils eine Gaußkurve an den Kern der Linie gefittet wird. Für die Detektion von CMEs werden Asymmetrien in den Balmer Linien, die durch die Doppler-Verschiebung entstehen, identifiziert.
281 Flares bei späten Hauptreihensternen (Typ K3 bis M9) wurden identifiziert. 10 mögliche CME Kandidaten, die einen zusätzlichen Fluss in den Flügel von Balmer Linien zeigen, wurden gefunden. Ein Spezialfall eines potentiellen CMEs wurde detektiert, der eine Absorption im blauen Flügel der $H\alpha$ Linie zeigt. Für alle Sterne wurden assoziierte Distanzen mithilfe des 2. Datensatzes des GAIA Satelliten gesucht. Die Energien der Flares in $H\alpha$ werden bestimmt und die Massen der CMEs werden abgeschätzt.
Die $H\alpha$ Flare-Energien liegen im Bereich von $10^{29} - 10^{33}$ erg. Die Flares früherer Sterne sind energiereicher, während spätere Sterntypen häufiger Flares zeigen. Die Massenabschätzungen der CMEs liegen im Bereich von $10^{15} - 8 \times 10^{18}$ g mit maximalen projizierten CME Geschwindigkeiten von 300 – 700 km/s. Die geringe Detektionsrate von CMEs, die in dieser Arbeit präsentiert wird, deckt sich mit zahlreichen Studien, die die CME-Frequenz von späten Hauptreihensternen zu bestimmen versucht haben.

Acknowledgements

First of all I would like to thank my supervisors Assoz. Prof. Manuela Temmer and Dr. Martin Leitzinger for the possibility to work on this project. Their guidance, advice, discussions and patience were indispensable for the progress of this work.

I would also like to thank the whole astrophysics group at IGAM for their help and support during my work on this project and for including me into the group like a family.

Many thanks to my former bachelor's thesis supervisor Dr. Thorsten Ratzka for helping me with my first steps into the scientific world of astrophysics.

I am thankful to all my peers on both the University of Graz and the Technical University of Graz that helped me throughout my Bachelor's and Master's program with their support, their productive discussions and also with their highly contagious motivation.

Last but not least, I thank my close friends and my family for supporting me over the course of the past years and for helping me chasing my dreams.

Data providing acknowledgements:
Funding for the Sloan Digital Sky Survey (SDSS) has been provided by the Alfred P. Sloan Foundation, the Participating Institutions, the National Aeronautics and Space Administration, the National Science Foundation, the U.S. Department of Energy, the Japanese Monbukagakusho, and the Max Planck Society. The SDSS Web site is http://www.sdss.org/.The SDSS is managed by the Astrophysical Research Consortium (ARC) for the Participating Institutions. The Participating Institutions are The University of Chicago, Fermilab, the Institute for Advanced Study, the Japan Participation Group, The Johns Hopkins University, Los Alamos National Laboratory, the Max-Planck-Institute for Astronomy (MPIA), the Max-Planck-Institute for Astrophysics (MPA), New Mexico State University, University of Pittsburgh, Princeton University, the United States Naval Observatory, and the University of Washington.
This research has made use of the VizieR catalogue access tool, CDS, Strasbourg, France (DOI : 10.26093/cds/vizier). The original description of the VizieR service was published in 2000, A&AS 143, 23.

Contents

1. Introduction

Especially in the past years, due to improved methods, numerous exoplanets have been detected. Increased knowledge about stellar activity is therefore one of the key aspects for research on the habitability of exoplanets as their atmospheric response is strongly depending on the characteristics (radiation, activity, evolution and lifespan) of the host-star. Early type stars (O, B, A) have a high short wavelength emission as well as short lifespans where they stay in hydrostatic equilibrium, rendering them to be unsuitable to host planets with atmospheres suitable for life. Therefore the focus lies on late type main-sequence stars (F, G, K, M), which stay stable for several billion years (Gyrs) exhibiting radiation peaking in the optical or near infrared part of the electromagnetic spectrum. On these stars, habitability of planets is highly dependent on stellar activity. The influence on planetary atmospheres is caused either by continuous effects (continuum radiation and stellar wind) or by energetic short time events (stellar flares and coronal mass ejections (CMEs)). They lead to planetary atmospheric mass loss, which has a major impact on the evolution and habitability of the planet (Khodachenko et al., 2007; Lammer, Lichtenegger, et al., 2007).
Flares in particular are the source of high energy emissions (X-ray, soft X-ray and extreme ultraviolet (EUV) emission). They lead to ionization and dissociation of particles in the upper atmosphere of exoplanets, resulting in thermospheric heating and upper atmosphere expansion (among other effects). Thermospheric expansion beyond the protecting planetary magnetic field results in an eroding atmosphere that gets stripped away from the planet (Lammer, Güdel, et al., 2012). Non-thermal effects eroding planetary atmospheres are stellar wind and CMEs. Khodachenko et al. (2007) and Lammer, Lichtenegger, et al. (2007) estimated that CME-induced ion pick up may strip off the whole atmosphere of a planet at near orbital distance to a M-star. CMEs are also relevant regarding stellar mass- and angular momentum loss, impacting the stellar evolution and the spin down of the star.
It is therefore important to get knowledge on both stellar flares and stellar CME parameters. Long observation times are necessary to get statistical significance on occurrence rates and parameters, especially for the so-far sparsely detected CMEs.

The activity of the present day Sun (a typical G2 main sequence star) is well investigated, but there remains ambiguity of how active the Sun was in its earlier life, which affects the evolution of the planetary atmospheres in the solar system.

Observing solar-like stars with different ages would therefore give an idea on the "Sun in time", meaning the evolution of solar-like stars throughout their lifespan. The Sun shows weak activity compared to observations of young main-sequence stars. While solar flares are observed frequently, they would be hardly detectable using optical disk-integrated measurements. Highly energetic stellar flares on late-type stars have been observed numerously, with later types (M dwarfs) showing more flaring activity than earlier ones.
While solar CMEs have also been detected frequently over the past decades, the number of reported CME detections on other stars have been sparse so far. On the Sun, there exists a high correlation between high energetic flares and CMEs, reaching $\sim 100\,\%$ for the strongest flares (Yashiro and Gopalswamy, 2009). Assuming the same correlation on stars would severely affect the habitability of exoplanets, as much more energetic flares on stars have been frequently observed leading to a high number of massive CMEs. Extrapolating this correlation to highly active stars also lead to an estimation of stellar mass-loss rates exceeding observed total mass-loss rates, implicating that this association might be more uncertain (Drake, Cohen, et al., 2013; Odert, Leitzinger, Hanslmeier, et al., 2017).

As direct observation of stellar CMEs is not feasible with current instrumentation, the detection of CMEs is based on indirect methods. CMEs that have been reported so far were mainly found using signatures such as X-ray absorption and Doppler-shifts Moschou et al. (2019). One method yielding reportings of CME events is based on space-borne measurements of X-ray absorptions. The decay of the absorbing column density is interpreted as a rising CME above an active region. These events were reported e.g. by Favata and Schmitt (1999) or Haisch, Linsky, et al. (1983). (See Moschou et al. (2019) and references therein for a more complete overview on CME reportings in literature so far.)

The other method uses enhancements in the blue/red wings in spectral lines, implicating that this flux comes from ejected material moving along the direction of the line-of-sight (towards or away from the observer). Thus, all inferred velocities determined by this method are projected velocities. Only the erupting filament/prominence is visible as a Doppler feature, which build the cores of CMEs. The first CME reported by this method was presented by Houdebine, Foing, and Rodono (1990), showing a large blue wing enhancement in $H\gamma$ with a projected velocity up to $5800\,\mathrm{km\,s^{-1}}$. There are several other reportings of blue shifted emission, possibly arising from a CME (Guenther and Emerson, 1997; Gunn et al., 1994; Fuhrmeister and Schmitt, 2004; Leitzinger, Odert, Ribas, et al., 2011; Vida, Kriskovics, et al., 2016). The reported velocities range from $\sim 100\,\mathrm{km\,s^{-1}}$ up to several thousand $\mathrm{km\,s^{-1}}$, with the event reported by Houdebine, Foing, and Rodono (1990) being the fastest one. The estimated CME masses from these reportings range from 10^{15} g up to 10^{19} g. Vida, Leitzinger, et al. (2019) searched for asymmetries in Balmer lines in both wings on near M-dwarfs. They reported projected velocities ranges of $100 - 300\,\mathrm{km\,s^{-1}}$ and estimated masses of

$10^{15} - 10^{18}$ g. CMEs may produce an absorption feature if the erupting filament lies directly in front of the stellar disk. Den and Kornienko (1993) and Ding et al. (2003) made estimations on an erupting filament on the Sun which was observed as a blue wing absorption in $H\alpha$, while also noting, that some parts of the material shows emission instead of absorption. So far, no absorption feature reminiscent of an erupting prominence has been reported on stars other than the Sun.

Both the flare and CME search have in common, that stellar observations over long time periods are necessary in order to detect these events. Therefore, one approach is to use time-resolved observations of stars in data archives to achieve the long observation time necessary for detecting such sporadic stellar activity phenomena.

The aim of this work is to search and find stellar activity phenomena like flares and CMEs on late-type main-sequence stars (F - M) using optical spectra of Sloan Digital Sky Survey (SDSS). Most of the stars in SDSS are observed several times in order to get a coadded spectrum with better signal-to-noise-ratio (SNR) than the single spectra. However, these single observations can be used to find temporal changes in the Balmer lines, indicating possible activity in the chromosphere. So far, only few works have used time-resolved optical SDSS spectra to infer stellar activity (Kruse et al., 2010; Hilton et al., 2010; Bell et al., 2012). Hilton et al. (2010) searched for flares on M dwarfs in optical SDSS spectroscopic data. While this goal is overlapping with the goals of the presented work, there are significant differences in this work: a) the present SDSS dataset is newer and therefore larger, b) the methodology is different, c) a different approach to pre-select the target sample was used, d) F, G and K type stars were also included, e) asymmetry/CME search was performed in addition to flares and f) the findings were crossmatched with GAIA DR2 values (Gaia Collaboration et al., 2018) giving distances to the stars, which were used to calculate absolute values of $H\alpha$ flaring energies and mass estimations for CME candidates.

2. Theoretical description

This chapter covers the basics behind stellar activity in general, starting with the Sun as an ordinary star and its activity related phenomena, in particular solar wind structures, flares and CMEs. Afterwards, the basics of late-type main-sequence stars and their difference to the Sun, especially regarding their stellar activity, will be elaborated. The theoretical description concludes with observational techniques to detect stellar activity, some of which are applied in this work.

2.1. Stellar activity of the Sun

The proximity to the Sun, the host star of the planet Earth, allows us to study its properties and behaviour in great detail. With it being a main-sequence star of type G2V one can use it as a first approximation to describe other stars, especially solar-like stars, on the main sequence.
The Sun exhibits several phenomena which can be summarised in the term "Solar activity". Short term activity includes flares and CMEs, while long term activity reflects itself in the solar cycle. This cycle takes 11 years, going through a solar minimum (weak activity, lower luminosity, no sunspots) and a solar maximum (high activity, higher luminosity, several sunspots).
The main focus of this work lies on the investigation and description of stellar short term activity phenomena and basic stellar parameters.

2.1.1. Basics of the Sun as a star

Stars in general are spherical astronomical objects consisting of plasma. They mostly consist of the basic elements of the universe (Hydrogen and Helium), but the abundances as well as the metallicity (meaning the abundance of all elements heavier than Helium) change depending on the age and the population of the star. The emitted energy of the star is produced in the core, where, due to high density and pressure, nuclear fusion is constantly producing heavier elements while emitting high energy photons in the process. Stars are in a state of hydrostatic equilibrium in most phases of their evolution, meaning that the

radiation pressure from the inside is balanced by the gravitational force of the star's mass:

$$\frac{dP}{dr} = -\frac{GM\rho}{r^2}, \tag{2.1}$$

where P denotes the pressure, r the radius, G the gravitational constant, M the mass of the star and ρ the star's overall density.

The Sun falls into the category of being an ordinary star, one of several hundreds of billion stars in the Milky Way. The Sun formed around 4.6×10^9 years ago (Bonanno, Schlattl, and Paternò, 2002) due to the gravitational collapse of a molecular cloud. It is now in its main-sequence stage, where its core is producing energy by nuclear fusion of Hydrogen to Helium. The star stays stable during this phase for several billion years. The evolution of a star is mostly governed by its mass; the Sun's mass (which will be denoted as one solar mass ($M_\odot$)) is 1.989×10^{30} kg [1]. The mean radius of the Sun is given by $R_\odot = 695700$ km [1]. It's surface gravity therefore amounts to $274\,\mathrm{m/s^2}$ which equals to $log(g) = 4.44$ (cgs units), while the escape velocity on its surface amounts to $v_{esc} = 617\,\mathrm{km/s}$.

Inner Structure and differential rotation

The Sun's interior is divided into three different parts: core, radiation zone and convection zone. Due to the nuclear fusion in the core, highly energetic photons (Gamma rays) are produced, which are then transported outwards. The core is surrounded by the radiation zone, extending out to 0.7 solar radii. Here, the high energy Gamma rays get scattered due to high density and short mean free paths. Therefore, this zone is completely ionized with radiation transport being the dominant transport mechanism for energy. The subsequent scattering of the photons lead to energy loss (from Gamma to X-rays to EUV down to optical wavelengths).
The outermost part of the internal solar structure is the convection zone. The Hydrogen in this zone is partially ionized, making radiation transport difficult as the radiation energy gets absorbed by ionizing the Hydrogen. Thus, the dominant mechanism of transporting the energy outwards is particle motion (or convection).
The transition zone between the radiation and convection zone is called the tachocline. It undergoes high shear forces due to the convection zone having a differential rotation depending on solar latitude and depth, while the underlying radiation zone rotates as a rigid body. This is hypothesised to be the main driver of the solar dynamo, resulting in solar activity phenomena.
The differential rotation leads to a winding up of the initially poloidal magnetic field, leading to an increased magnetic pressure. Due to the pressure balance and

[1] https://nssdc.gsfc.nasa.gov/planetary/factsheet/sunfact.html

temperature equilibrium, a magnetic flux tube (with higher magnetic pressure on the inside) possesses a lower density than its surrounding and thus rises inside the convection zone (which is called magnetic buoyancy). The emerging flux tube will get visible on the photosphere in the form of sunspots (spots of lower emission due to the aforementioned decrease in density). They usually appear in pairs of opposite polarity, but more complex groups of sunspots are also common.
These spots and their strong magnetic fields build the cores of active regions on the Sun (and its atmosphere).

Sun's atmosphere

The outer part of a star is the stellar atmosphere. This atmosphere gives rise to the stellar spectrum that we observe. The solar atmosphere is structured as follows:

- Photosphere: a thin layer that defines the "surface" of the star and is the source of the continuous emission that is visible in visual and infrared wavelength ranges.
- Chromosphere: the layer above the photosphere, where the temperature rises from 6000K up to several ten thousand Kelvin. $H\alpha$ emission arises from this layer, giving it a reddish color.
- Transition region: the thin region between chromosphere and corona, showing a steep rise in plasma temperature.
- Corona: the outermost layer, consisting of highly ionized plasma with temperatures up to a few million Kelvin. Its structure is depending on active regions and is usually observed in Ultraviolet (UV), EUV and X-ray wavelength ranges.

Solar activity phenomena can be observed in the solar atmosphere. Active regions are visible on the photosphere as dark sunspots and faculae (regions of enhanced intensity, usually near sunspots), while UV and EUV observations reveal plages (large, bright structures) in the chromosphere and coronal loops (arc-like structures outlining the closed magnetic field lines of active regions) in the corona. Prominences and filaments (visible in $H\alpha$) can be found at the magnetic polarity inversion line in active regions. Frequent flaring activity is found in proximity to these regions.

Spectrum of the Sun and line formation

This section is following the work of Rutten (2003) and Pradhan and Nahar (2011).

The continuous emission of a star is described by black body radiation, given here as spectral radiance distribution in terms of wavelength λ:

$$B_\lambda(T_*) = \frac{2hc^2}{\lambda^5} \frac{1}{exp(hc/\lambda k T_*) - 1} \tag{2.2}$$

where h denotes the Planck constant, c the speed of light, k the Boltzmann constant and T_* the temperature of the star. The peak of the wavelength at a certain temperature is given by Wien's law:

$$\lambda_p = \frac{2.8978 \times 10^7 \text{Å} K}{T_*}. \tag{2.3}$$

The Sun with a surface temperature of approximately 5770 K has its spectral radiance peaking in the visible wavelengths around 500 nm, with a sharp decrease in the UV regions and a long tail into the infrared and longer wavelengths.

Stellar atmospheres lead to absorption and emission of radiation due to matter in the path to the observer. These can be described by transfer equations, which basically quantify the emission and absorption of intensity along a distance s:

$$\frac{dI_\nu}{ds} = -\kappa_\nu (I_\nu - S_\nu) \tag{2.4}$$

$$\frac{dI_\nu}{d\tau_\nu} = I_\nu - S_\nu \tag{2.5}$$

$$\tau_\nu = -\int_0^s \kappa_\nu ds \tag{2.6}$$

Several variables have been introduced: the absorption coefficient (opacity) κ_ν which quantifies the amount of absorption, the value of intensity I_ν, the optical depth τ_ν describing the transparency of a medium up to a certain distance, and the source function S_ν which is defined as $S_\nu = \eta_\nu/\kappa_\nu$, the ratio between emissivity and opacity. If one assumes local thermodynamic equilibrium (LTE), the source function is given by Planck's law B_ν. Media with an optical depth of $\tau_\nu << 1$ are transparent (corona, chromosphere) while large optical depth $\tau_\nu >> 1$ are opaque, which is the case in photosphere. One can rewrite the transfer equation to

$$\left(\frac{d}{d\tau_\nu} I_\nu e^{-\tau_\nu}\right) = -S_\nu e^{-\tau_\nu} \tag{2.7}$$

and bring it into the integral form

$$I_\nu(\tau_\nu) = I_\nu(0) e^{-\tau_\nu(D)} + \int_0^{\tau_\nu} S_\nu(t_\nu) e^{-(\tau_\nu - t_\nu)} dt_\nu \tag{2.8}$$

with $I_\nu(0)$ being the initial intensity. Using the simple assumption that the source function does not vary with the location, the calculation of the intensity through a medium with thickness D leads to

$$I_\nu(D) = I_\nu(0)e^{-\tau_\nu(D)} + S_\nu\left(1 - e^{-\tau_\nu(D)}\right). \tag{2.9}$$

For optical thick media it reduces to

$$\tau_\nu >> 1 \qquad \Rightarrow \qquad I_\nu(D) \approx S_\nu \tag{2.10}$$

which, in LTE, leads to the black body radiation.
For optical thin media, using the approximation $exp(-\tau_\nu) \approx 1 - \tau_\nu$ equation 2.9 changes to

$$\tau_\nu << 1 \qquad \Rightarrow \qquad I_\nu(D) \approx I_\nu(0) + (S_\nu - I_\nu(0))\,\tau_\nu(D) \tag{2.11}$$

which leads to a simple explanation for the formation of spectral lines in spectra: assuming LTE, the source function is given by black body radiation and therefore only depends on the temperature. If the temperature is increasing outwards, then S_ν is higher than the initial intensity $I_\nu(0)$, leading to an additional flux at this frequency. On the other hand, if the temperature gradient is negative, then $S_\nu < I_\nu(0)$ is valid, leading to a decrease of the initial flux.

Spectral lines itself are defined as energy that is either removed or added to the continuum emission. Their shape depend on the atomic transition as well as the plasma environment. The line gets broadened by the following mechanisms:

- Natural broadening / radiation damping:
  Due to the Heisenberg uncertainty principle the energy levels are not exact, leading to a natural broadening of the spectral lines. This mechanism leads to a Lorentzian function, which is, in general, described by the following equation:
  $$\Phi_\nu = \frac{\Gamma/(4\pi^2)}{(\nu - \nu_0)^2 + (\Gamma/4\pi)^2} \tag{2.12}$$
  where Γ describes the quantum mechanical damping constant, ν and ν_0 the frequency and the line-centre frequency, respectively. The final absorption coefficient is described by
  $$a_\nu = a_0\Phi_\nu \tag{2.13}$$
  where a_0 is a set of frequency-independent constants. The extend of natural broadening is usually much smaller than the other two mechanisms described herein.
- Thermal (Doppler) broadening:
  The velocities of photon - emitting atoms and molecules towards or away from the observer lead to a Doppler-shift in the frequency of said photons. These Doppler-shifts are therefore dependent on the temperature (or better

thermal motion) of the emitting particles. Thus, the velocity distribution is given by the Maxwellian distribution at a certain kinetic temperature T_k

$$f(v)dv = \left(\frac{m}{2\pi k T_k}\right)^{1/2} \quad exp\left(-\frac{mv^2}{2kT_k}\right) dv \tag{2.14}$$

with v the velocity and m the mass of the particle. This is the distribution along one axis, as only the motion along the line-of sight to the observer is of interest. Using the Doppler-shift in frequency ($\nu = \nu_0(1 + v/c)$) and inserting it into equation 2.14, one obtains the distribution depending on the frequency, which is a Gaussian profile:

$$f(\nu)d\nu = \frac{1}{\sqrt{\pi}\Delta v_D} \quad exp\left[\left(-\frac{\nu - \nu_0}{\Delta v_D}\right)^2\right] d\nu \tag{2.15}$$

$$\Delta v_D = \frac{\nu_0}{c}\sqrt{\frac{2kT}{m}} \tag{2.16}$$

Here, ν_0 denotes the rest frequency and v_D the Doppler width. The final absorption coefficient is again given by $a_\nu = a_0\Phi_\nu$, where Φ_ν equals the right-hand side of Eq.2.15.
Doppler broadening mainly affects the core of a spectroscopic line compared to the other mechanisms, which dominate the wings of the line.

- Pressure or collisional broadening:
  At high densities, the interaction of atoms with other particles lead to a broadening of lines by perturbing the energy levels. Pressure broadening is described by the electromagnetic perturbation due to Stark effect, resonances or van der Waals force, all of which result in a Lorentzian shape of the line broadening. The resulting line profiles follow equation 2.12, with Γ being functions depending on the local density. In-depth analysis of collisional broadening is made using quasi-static approximations, utilizing a probability function for electric fields caused by near perturbators. Both line broadening and line shifting are possible. Pressure broadening is dominating the wings of spectroscopic lines.

The combination of natural, Doppler and pressure broadening results in the Voigt function, which is the folding of a Gaussian and Lorentzian function and can be generally described by

$$\Phi(\nu - \nu_0) = \frac{1}{\sqrt{\pi}\Delta v_D} H\left(a, \frac{\nu - \nu_0}{\Delta v_D}\right) \tag{2.17}$$

with H being the Voigt function which can be calculated numerically and follows the Doppler broadening in the core and a damping profile in the wings. The Voigt function may be approximated using pseudo-Voigt functions, utilizing a linear combination of both Gaussian and Lorentzian function.

The strength of an absorption line is usually described by the equivalent width, which is the width of the rectangle with the same area as the spectral line while its height is equal to the continuum level. Plotting the equivalent width with respect to the column density (N) leads to the so-called curve of growth: The equivalent width increases linearly with the density up to the point of saturation (where nearly all photons of the continuum are absorbed in the line core). A further increase of the equivalent width is mainly related to Doppler broadening and is proportional to $\sqrt{ln(N)}$. After the saturation of the whole line core a further increase of the equivalent width is happening by damped wings and is proportional to $\sqrt{N}$.

Interactions between photons, electrons and atoms / ions are the source of absorption and emission lines. These are broadly simplified in the concept of LTE, while a more detailed formulation is given by non - local thermodynamic equilibrium (NLTE) calculations.
LTE is based upon following assumptions (following Pradhan and Nahar (2011)):

- Maxwell-Boltzmann statistics: Equal population probability of quantum states with equal energy; state population probability at temperature T and energy ϵ is given by $exp(-\epsilon/kT)$; only one electron can occupy a quantum state.
- Boltzmann equation: Describes the energy level populations of an atom (or ion) at a certain temperature:

$$\frac{n_i}{n_j} = \frac{g_i}{g_j} exp\left(\frac{-E_{ij}}{kT}\right) \tag{2.18}$$

  Here, i and j describe specific energy levels of the atom, n the population number, g are energy states per unit energy per volume (statistical weights), E_{ij} the energy difference between the two levels, k Boltzmann's constant and T the kinetic temperature. To calculate the ratio between a level and the total number of the atomic species, one needs the internal atomic partition function, which is a sum over all possible states of the atom.
- Saha equation: Describes the ratios of different ionization states of one element at a given temperature:

$$\frac{N_{m+1}}{N_m} = \frac{2}{\lambda^3 n_e} \frac{g_{m+1}}{g_m} exp\left(\frac{-I_{m+1,m}}{kT}\right) \tag{2.19}$$

$$\lambda = \sqrt{\frac{h^2}{2\pi m_e kT}} \tag{2.20}$$

  Here, m denotes a ionization level of the ion species, N the population number, λ the thermal de Broglie wavelength (determined by the Planck's constant h, the electron mass m_e, Boltzmann's constant k and the kinetic temperature T), g the specific statistical weights, and $I_{m+1,m}$ the ionization energy from ionization state $m+1$ to m.

Combining the equations 2.18 and 2.19 leads to a complete description of the excitation and ionization populations of one atomic species in the stellar atmosphere in LTE. These are good assumption for high electron densities.

In NLTE, one takes all radiative and collisional processes into account, requiring numerical solutions to determine atmospheric properties. Several atomic processes are possible:

- Photo excitation: A photon hitting an atom, leading to excitation of one of the electrons to a higher level. Reverse effect leads to an emitting photon by electron recombination to a lower level. (Bound - bound transition)
- Electron impact excitation: A free electron hitting an atom, transmitting energy to it and leading to a bound electron getting excited on a higher level. This is followed by radiative recombination.
- Photo ionization: A photon with sufficiently high energy hitting an atom and ionizing it by transferring its energy to a bound electron. The reverse effect emits a photon after a free electron combines with an ion. (Bound - free transition)
- Autoionization: A loosely bound electron on an excited atom breaking free while the excited electron decays to a lower level without emitting a photon (Auger-Meitner effect).
- Dielectric recombination: A captured low energy free electron recombines into a stable bound state while emitting a photon, resulting in a negatively charged ion.
- Electron impact ionization: A free electron with sufficiently high energy hitting an atom and ionizing it by transferring its energy to a bound electron, leading to two free electrons an an ion.

Additional important processes for determining opacity are electron scattering (Thomson scattering, elastic scattering of electron and photon, changing their direction while maintaining their energies) and free - free absorption (Bremsstrahlung, a photon gets absorbed/loses energy by an electron that is passing by a nucleus; inverse process radiates a photon by decelerating in an electric field). Molecular absorption are prevalent in cool stars (photon excites vibrational or rotational modes in molecules and gets thereby absorbed).

2.1.2. Solar wind

The solar wind is a continuous outflow of particles on "open" magnetic field lines ("open" because these magnetic field lines close in the outer part of the heliosphere). The solar wind is made up of plasma, with its main constituents being electrons, protons and $\alpha-$particles. Their origin lie in the corona, where they have to be constantly replenished from lower atmosphere layers. A mass

loss of $\sim 10^9\,\mathrm{kg\,s^{-1}}$ is observed on the sun due to the solar wind (Maciel, 2014). The solar wind drags the frozen-in magnetic field line with it and thus creates the interplanetary magnetic field, which interacts with the magnetospheres of the planets in the solar system.
Solar wind comes in two variations:

- **Slow solar wind:** With speeds of 300 to 400 km/s, this type of solar wind has its origins in coronal streamers.
- **Fast solar wind:** With speeds of 500 to 800 km/s, this type of solar wind has its origins in coronal holes.

Thus, the solar wind changes during the solar cycle depending on the latitude of coronal streamers (near ecliptic at solar minimum, migrate to higher latitudes at higher activity) and coronal holes (most prevalent at the poles at solar minimum, but can expand from there or develop at any other latitude).

Source of this section: lecture notes from 'Introduction to Solar Physics' from lecturer Assoz. Prof. Astrid Veronig at the Karl-Franzens Universität Graz.

2.1.3. Solar flares

Flares are sudden enhancements of radiation due to sudden rearrangement of magnetic field configuration in or in the proximity of active regions. Flares are observed over the entire spectrum covering wavelength ranges from short (X-ray, EUV, UV) to long (optical, infrared, radio). In the visible spectrum, the flare is prominent in specific absorption lines due to enhanced Doppler and pressure broadening.
Flares are explained using magnetic reconnection theory: complex magnetic field-lines may reconnect in the solar atmosphere, converting magnetic energy into kinetic energy and heating up the plasma in the process. For reconnection to happen, there have to be magnetic field lines of opposite direction getting close to each other. Due to Ampere's law ($\nabla \times B = \mu_0 J$, rotor of magnetic field B yields a current density J times a constant μ_0) a current sheet is building between the regions. This current sheet locally breaks ideal MHD, making the (otherwise neglected) plasma resistivity a significant factor in the so called diffusion region. Within this region, the oppositely directed field-lines reconnect to a lower topology, releasing stored energy as thermal energy in the plasma. Reconnection models (standard models are Sweet-Parker and further Petschek) describe the magnetic reconnection as process during which two anti-parallel fields pushed together by an outside force, forming a strong current sheet in between. The reconnection in this region leads to plasma flowing out of both ends of the diffusion region with high velocities. At the lower part (towards solar surface) this causes heating and becomes visible as solar flare, on the upper part the closing of magnetic field lines leads to the generation of a coronal mass ejection. Hence,

the two phenomena are usually coupled but may also occur independent of each other (keyword: stealth CME, confined flare).
Figure 2.1 shows the evolution of a flare (adopted from Magara et al., 1996). Flares on the sun typically show two phases, the onset of reconnection of a coronal loop starts the fast impulsive phase. The reconnection heats and accelerates plasma particles out of the diffusion region, ejecting the upper, reconnected fields with its plasma (plasmoid) outwards. The inward directed accelerated and heated particles build a front on top of the lower, reconnected loop, emitting hard X-rays in the process. Accelerated Electrons directed outwards produce radio type III bursts by emission at the electron plasma frequency (which is a function of local density). Inward directed accelerated electrons follow the field lines down (producing gyro-synchrotron emission observable in radio wavelengths on their way) where they hit the much denser chromosphere, emitting hard X-rays by non-thermal Bremsstrahlung at the footpoints of the reconnected loop. Most of the energy of the fast electrons gets thermalized, heating up the chromospheric material and building up pressure, which is called chromospheric evaporation. $H\alpha$ ribbons at the footpoints of the loop are generated in the process.
After this impulsive phase follows the gradual phase: the heated chromospheric material is conducted ("evaporated") into the loop and therefore migrates up into the corona, emitting soft X-rays, EUV, UV and $H\alpha$ radiation. The resulting flaring loop grows upwards (indicating that the reconnection point is moving higher up) and stays visible for several minutes up to hours (Fletcher et al., 2011). The strongest flares may even produce flare ribbons visible as white light emissions, enhancing the whole continuum in addition to spectroscopic lines.

Solar flares are usually categorized using soft X-ray measurements ($1 - 8$ Å) from the Geostationary Operational Environmental Satellite (GOES) satellites. The classification consists of a letter (A, B , M , C or X), each corresponding to an order of magnitude ($X = 10^{-4}\,\mathrm{W\,m^{-2}}$, times a multiplication factor. E.g. the largest flare of the previous solar cycle was classified as a X9.3 class flare[2].
Another characterization of flares observed in $H\alpha$ (called the $H\alpha$ importance classes) uses the area of the flare compared to the total solar disk area.
Typical flare energies released by $H\alpha$ emission on the Sun is found in the range of $10^{26} - 3 \times 10^{30}$ ergs (Antia, Bhatnagar, and Ulmschneider, 2003).

Main sources of this section: Aschwanden (2019), Foukal (2004), lecture notes from 'Introduction to Solar Physics' from lecturer Assoz. Prof. Astrid Veronig at the Karl-Franzens Universität Graz.

[2] https://www.spaceweather.com/solarflares/topflares.html

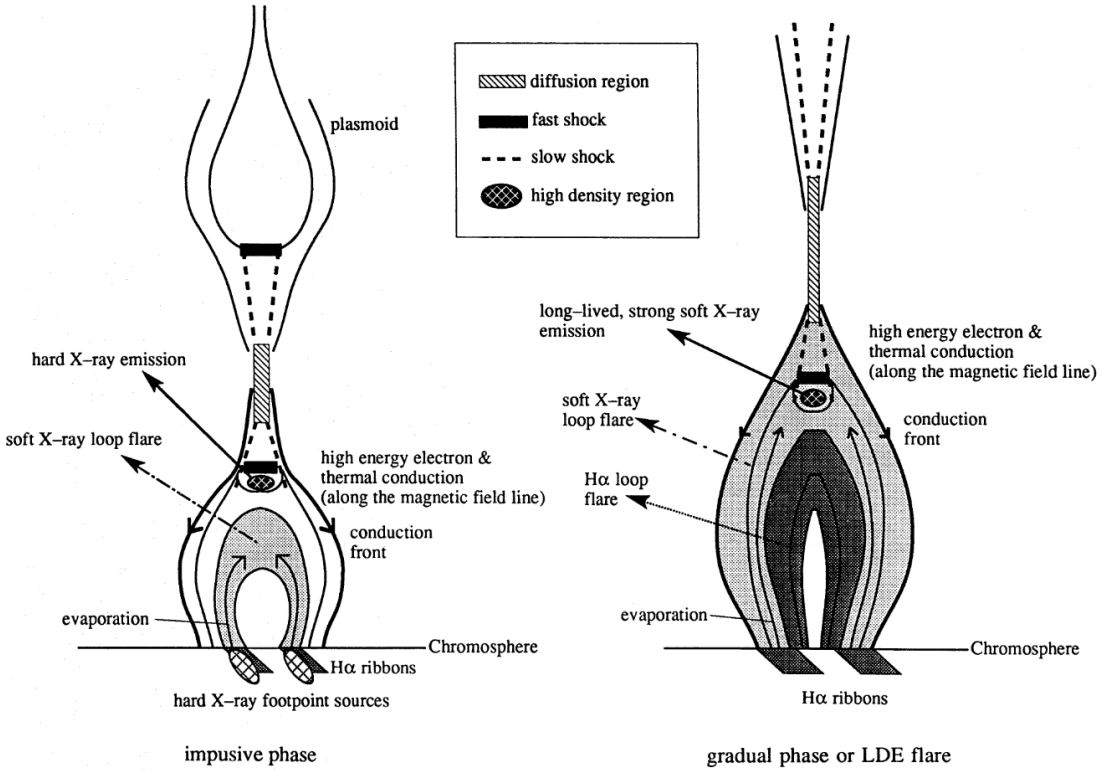

Figure 2.1.: Evolution of a classical two ribbon flare on the sun. Adopted from Magara et al. (1996)

2.1.4. Solar CMEs

CMEs are clouds of magnetized plasma expelled from the star. Theses eruptions can have velocities of the ejected material up to several thousand kilometers per second (Gopalswamy et al., 2010) and typical masses of $10^{13} - 10^{16}$ g (Vourlidas et al., 2010).
CMEs show a three-part structure (see Figure 2.3), visible as a bright front, a dark cavity and a bright core in the images of coronagraphs. The bright front is consisting of streamer and/or coronal material, visible as a bright loop. The dark cavity is explained as being the inner part of a magnetic flux rope (twisted field lines with the footpoints on the sun). As the overall pressure stays in equilibrium, the additional magnetic pressure inside the rope (given by $P_m = B^2/8\pi$, with B being the magnetic field) diminishes the gas pressure ($P_g = n\,k\,T$, with n being the density, k the Boltzmann's constant and T the temperature). Thus, the density inside the cavity is lower, making it darker in appearance. The bright core of the flux is made up of erupting prominence material.
The expansion of a CME is typically self-similar, showing a constant width during the radial expansion. These CMEs show significantly higher speeds with mean values around 1000 km/s opposed to the average CME speed of 475km/s (Gopalswamy et al., 2010). It is important to note that the average CME speed is lower than the escape velocity of the Sun (617 km/s), indicating that CMEs are

not ballistic.
Their masses are calculated using measured flux in white light images made by coronagraphs. The visible emission arises from Thomson scattering, which is proportional to the density. The occurrence rate of CMEs are mostly dependent on the solar cycle, with rates of ~ 1 CME/day during thew minimum up to ~ 10 CMEs/day at the solar maximum (Lamy et al., 2019).

CMEs are associated with flares, consisting with the standard model for erupting flares that explains it as two results of the same process. The association rate of flares and CMEs reaches more than 90 % for highly energetic X-class flares (Yashiro and Gopalswamy, 2009). Other associated phenomena are radio type II bursts, which may be emitted by electrons at the local electron plasma frequency due to a shock driven by a CME moving through the solar atmosphere. Other waves associated with CMEs are Moreton waves (shock waves visible as a chromospheric signature) and Coronal EUV waves. Coronal dimmings on the other hand are interpreted as missing coronal material that got evacuated by the CME (Dissauer et al., 2018).

CME models can be divided into models with or without reconnection. The standard model (tether cutting) explains the building of a CME flux rope by an arcade of coronal loops that reconnect, forming the rope out of the remaining plasmoids which subsequently gets expelled outwards. Meanwhile, the usual flare happens underneath it. This model is displayed in Figure 2.2, adopted from Masson, Antiochos, and DeVore (2013).
A second model is called the breakout model, which, in contrast to the tether cutting model, has reconnection above the CME. It demands a multipolar topology with a highly sheared arcade. The magnetic tension of an unsheared overlying field gets reduced by the reconnection, paving the way for an eruption of the sheared arcade. Tether reconnection behind the rising arcade is necessary in addition.
There are models using ideal MHD, which work without magnetic reconnection and a pre-existing flux rope. The torus instability model has a flux rope erupting depending on how steep the decrease of the Lorentz force of the overlying field is (Kliem and Török, 2006).
The kink instability model explains the CME by a pre-existing flux rope that gets twisted beyond a critical threshold, leading the whole flux rope to kink and rise upwards. These ideal models are important for triggering a CME, but they do not supply enough energy to produce fast CMES (while models with reconnection do).
Important to note is that one eruption can lead to several additional CMEs being ejected due to the interaction with large scale magnetic fields in the corona.
The speed of a CME is determined by Lorentz force and gravitation in vicinity to the Sun during the acceleration phase, while drag dominates the speed in the interplanetary space. The drag force is depending on whether the CME is faster

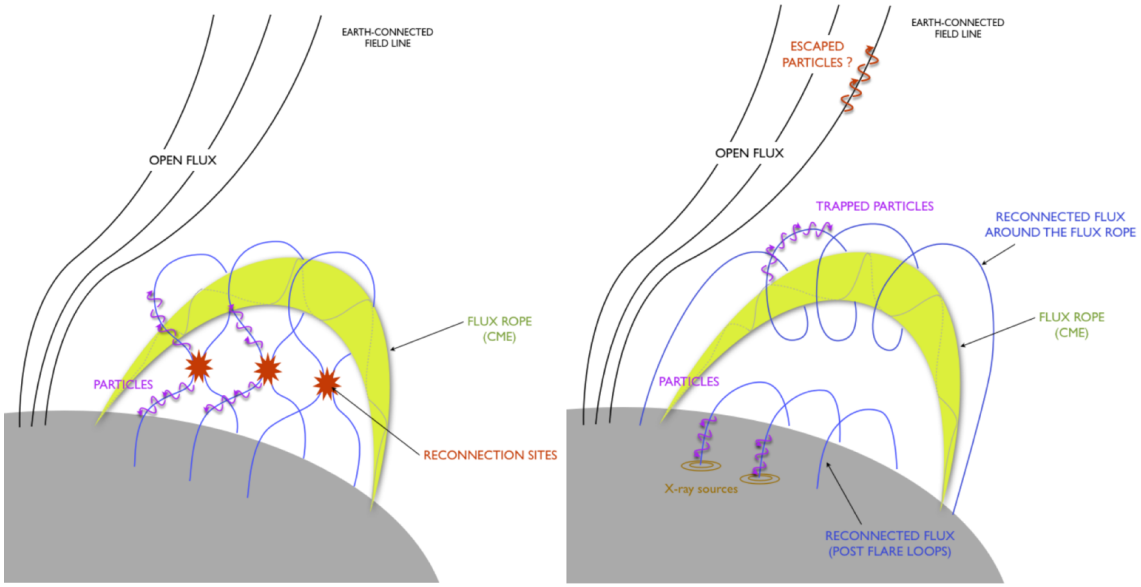

Figure 2.2.: Standard model of flare and CME onset (tether cutting). Adopted from Masson, Antiochos, and DeVore (2013).

or slower than the surrounding solar wind (Vršnak et al., 2013).
There exists the possibility of CMEs not breaking free even with high energy flares happening at an active region in the Sun. This can be explained by a strong overlying magnetic field, suppressing the ejection of material (Thalmann et al., 2015; Sun et al., 2015).

Main sources of this section: Aschwanden (2019), Foukal (2004), lecture notes from 'Introduction to Solar Physics' from lecturer Assoz. Prof. Astrid Veronig at the Karl-Franzens Universität Graz.

2.2. Late - type main sequence stars

This section considers stars of the main-sequence of types F, G, K and M, as these are the main focus of this work.

2.2.1. Stellar evolution

In general, stars are divided into classes based on the spectrum of the star's emitted light. The common classification system is called the Morgan-Keenan - classification, where the spectral classes are denoted with letters (O, B, A, F, G, K, M). These spectral classes correspond to the star's photospheric temperature,

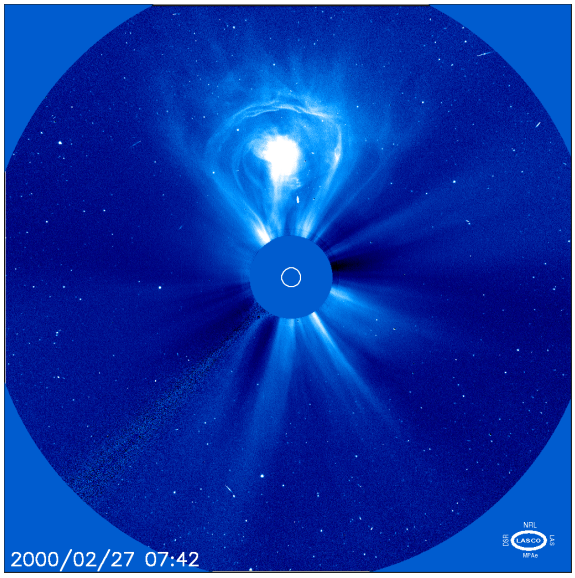

Figure 2.3.: CME with typical three-part structure observed with the Large Angle and Spectrometric Coronagraph Experiment (LASCO) (Credit: NASA, https://soho.nascom.nasa.gov/hotshots/2000_02_26/).

where the class O stars are the hottest (> 30000 K, Habets and Heintze, 1981) while the class M stars are the coldest ($\sim 2400 - 3700$ K, Habets and Heintze, 1981). These classes are divided into subtypes using arabic numerals from 0 to 9, indicating a lower temperature with a higher number (a G9 star is colder than a G5 star). The classification system includes several other types, like white dwarfs (denoted with the letter D), carbon stars (letters C and S) or brown dwarfs (letters L and T). The exact classification is defined by the strength of certain spectral lines in the spectrum of each star.

In addition to the spectral classification, stars are also divided into different luminosity classes. The basis of this differentiation is the surface gravity of each star, which is different for dense dwarfs stars than for giants. Information on the surface gravity can be gathered from analysing the pressure broadening of spectral lines. This differentiation also corresponds to the luminosity of the star. The luminosity classes (and their respective roman numerals) are: hypergiants(0), supergiants(I), bright giants(II), giants(III), sub-giants(IV), dwarfs or main-sequence-stars(V), sub-dwarfs(VI). White dwarfs can also be denoted with the numeral VII.

A common way to visualise the classification of stars is the Hertzsprung-Russel-Diagram (HRD). This diagram shows the spectral type or effective temperature on the x-axis (from hottest / bluest on the left to coolest / reddest on the right), while its y-axis shows the luminosity or absolute magnitude of the stars. Putting all known stars in this plot gives us clear branches where most stars lie: the majority of the stars lie in the main sequence, which is seen as a diagonal from the upper left to the lower right corner of the diagram. The conclusion is, that stars are most of their lifetime on the main sequence as dwarf stars, where they

stay stable for hundreds of millions up to several billions of years depending on their spectral type. On the upper right part of the diagram lies the horizontal branch, consisting of giants, bright giants and supergiants, while White dwarfs with their high temperature and low luminosity can be found on the lower left part of the diagram.

Stars undergo different evolutionary states. All stars begin with the gravitational collapse of a molecular cloud, breaking into small fragments, that become more and more dense. The critical mass enforcing this collapse is given by the Jeans mass, which is the result of the condition, that the free fall time due to gravity needs to be shorter than the time that the speed of sound needs to cross the cloud.
The temperature increases during the collapse (due to the conversion of gravitational potential energy into kinetic energy) as well as the pressure, forming a so-called protostar, which is a huge rotating sphere of hot gas. The rotation is a direct result of the conservation of angular momentum.
An accretion disk forms around the star, which gets blown away later due to the radiation pressure emitting from the newborn star. At this phase the star is called a pre-main-sequence star. These are divided into following groups: T Tauri stars, which have lower to middle masses, and Herbig ae/be stars, having higher masses. T Tauri stars are also divided into classical T Tauri stars (CTTS, showing strong $H\alpha$ emission) and weak line T Tauri stars (WTTS, showing weak or no emission lines).
After accreting enough mass the star contracts, reaching core pressure and density levels high enough to start nuclear fusion of hydrogen. This marks the zero age main sequence of the star.
The ongoing evolution of a star on the main sequence and beyond is determined by its mass. We distinguish by three evolution types:

- Low mass stars (masses below $\sim 0.5\,M_\odot$): These stars stay on the lower right part of the HRD, indicating cool dwarf stars (late K, M and L types). They produce energy by nuclear fusion of hydrogen to helium, keeping up the hydrostatic equilibrium. The relative rate at which the hydrogen is burnt into helium is comparatively low. No star of this type ever reached the phase beyond the fusion of hydrogen due to the fact that this would take longer than the current age of the universe. Stars with the lowest masses show a fully convective internal structure, making them highly magnetically active due to the movements of electric charges.
- Medium mass stars (masses between $\sim 0.5\,M_\odot$ and $\sim 8\,M_\odot$): These stars stay on the main sequence for several billion years before the amount of hydrogen in the core gets too low to maintain the fusion process. Subsequent contraction starts a hydrogen burning shell, while a helium core gets build up. This causes the star to expand and cool down, becoming a subgiant on the red giant branch (RGB). Eventually, the core becomes hot enough to start nuclear fusion of helium, which is called the helium flash. This sets

the star on the horizontal branch (HB), were the star gets temporarily hotter before the core again starts to run out of fuel, expanding again after forming a helium burning shell. This makes the expanding star cooler and more luminous, reaching the asymptotic giant branch (AGB). The star loses large amount of its mass during this phase due to stellar wind, finally building a planetary nebula and leaving behind the star's core as a white dwarf (consisting of degenerated electrons).

- High mass stars (masses above $\sim 8\,M_{\odot}$): These stars have shorter lifetimes due to their higher rates of nuclear fusion. They start at the main-sequence as O or B stars with high temperatures and luminosities. They evolve along the horizontal branch in the HRD and end either as a neutron star or as a black hole, due to their cores being too massive to be uphold by electron degeneracy in contrast to medium sized stars.

Main sources of this section: de Boer and Seggewiss (2008), Meadows (1978), lecture notes from 'Stellar Structure and Stellar Evolution' from lecturer Dr. Thorsten Ratzka at the Karl-Franzens Universität Graz.

2.2.2. Solar versus stellar activity

While the Sun is the obvious example for G type stars, the differences in the other discussed spectral types (F, K and M) need to be pointed out.
Stellar activity in late type stars is generally attributed to an outer convection zone and differential rotation, resulting in high magnetic activity. There is also the clear relation between higher rotation rates, stellar age and stellar activity, rendering young and fast rotating objects far more active than older ones. Findings of large stellar spots (indicating magnetic activity) have been reported on late-type stars, with F7 - K2 type stars showing variability due to stellar spots similar to the solar phenomenon (Berdyugina, 2005).

F-type stars posses an outer (albeit shallower) convection zone, while usually showing faster rotation than stars of a later type. Wolff, Boesgaard, and Simon (1986) reported, based on measurements of the He I line (5876 Å), that later F types (down to F5) show activity that could be explained with the solar dynamo model. Earlier type F stars were found to be highly active with a smaller range of activity levels, questioning whether another heating mechanism other than the magnetic dynamo takes place. The observation of activity by measuring the filling in $H\alpha$ was discarded due to rotational broadening and / or small contrast between the emission in photosphere and chromosphere (Wolff, Boesgaard, and Simon, 1986).
Later types than the Sun exhibit larger convective zones, leading to the valid assumption, that they show high magnetic activity. There also appears to be a trend of decreasing differential rotation with decreasing effective temperature, implying that the dynamo mechanism on lower-mass stars operates differently

than the one the Sun (Barnes et al., 2005). M dwarf stars exhibit high magnetic activity which reflects itself in emission in chromospheric lines. The late type M dwarfs (M5 or later) posses, in contrast to the Sun, a fully convective internal structure. This gives rise to strong magnetic fields due to turbulent motions. This kind of turbulent dynamo is also considered to be the main driver in fully convective T Tauri stars. West, Hawley, Walkowicz, et al. (2004) found the rise in magnetic activity for the fully convective late-type M stars, with the fraction of active stars peaking at spectral types M7 to M8.

2.3. Observational techniques for stellar activity

While activity related phenomena on the Sun (solar wind, flares, CMEs) can be spatially resolved and thus observed in great detail, the same does not hold for other stars due to their large distances. Stars appear as point-like sources, and therefore one can only observe the electromagnetic radiation which is already integrated over the whole disk of the star. This simple fact gives rise to obvious limitations on the observation of stellar activity phenomena:

- Due to the observational constraints one may only observe the phenomena resulting in the highest difference in electromagnetic radiation (dependent on the SNR of the observational data).
- The ratio between the integrated flux of the star's disk and the flux from the activity phenomena is crucial. It is more probable to detect a flare on a star with lower luminosity than a flare of the same energy on a star with higher luminosity.

This second fact combined with the knowledge of low mass stars being fully convective results in the reasonable assumption that one may observe more stellar activity phenomena on late-type stars like M or K stars than earlier types like G or F.

Observation of stellar wind

Stellar wind is low in density and more or less a constant outflow, making it hard to differentiate this flow from the star's spectrum. In optical spectra, stellar wind is not providing a time-evolving difference in radiation that is big enough for observations. Indirect evidence of stellar wind is the loss of rotational energy during the stellar evolution and influences on the stellar environment.
Exceptions from these rules are very hot and evolved cool stars, showing massive stellar winds. The stellar wind of hot stars has high velocity and consists of the partially or highly ionized material of the star's surface and are driven by the high radiation pressure of the star. This is visible in the absorption of UV lines (Maciel, 2014). Cooler, evolved stars on the RGB also drive their stellar wind

trough radiation pressure, which consists of atoms and molecules. It cools down and condensates as this material gets further away from the star. Stars on the RGB show high mass-loss rates from stellar winds, up to $10^{-6}\,M_{\odot}$/year (Maciel, 2014).
Non-detections of stellar winds on low mass stars using free-free thermal radiation at radio wavelengths led to upper constraints on the mass loss rates (Fichtinger et al. (2017) and reference therein). Another possible measurement can be done by measuring the accretion of mass on a DAZ star (white dwarf showing metal lines) coming from a low mass companion (Debes, 2006). Alternatively, the detection of X-ray emission arising from ionised wind particles interacting with neutral hydrogen poses another option for the detection of stellar wind (Johnstone et al., 2015). *Lyα* absorption arising from heated neutral hydrogen due to the interaction with stellar wind poses another possibility to observe stellar wind on stars (for stars that are surrounded by interstellar medium (ISM) containing large amount of neutral hydrogen) (Wood et al., 2001).
Stellar wind may heavily influence the atmospheres of planets, rendering it an important factor in the evolution of exoplanets.

Observation of stellar flares

Stellar flares can be observed as sudden enhancements in the electromagnetic radiation. One can use either photometric observation of the star in a specific wavelength range (using a filter) resulting in a lightcurve or analyzing the spectrum of the star at different times and look at spectral lines indicating flaring activity. Both require several and, if possible, continuous observations of one and the same star.
Flares are found on many types of stars across the HRD. There have been reports of flares on all stars on the main sequence, with the majority of flares coming from dKe and dMe stars (Pettersen, 1989). Flares are fairly common among young stellar objects (pre-main-sequence / T Tauri stars). Under the evolved stars, close binary systems and systems containing a white dwarf often exhibit flares. RS CVn stars (binaries with at least one component being a subgiant) are known for showing high flaring activity across the spectrum (Pettersen, 1989; Haisch, Strong, and Rodono, 1991). In general, stars with outer convection zones on or above the main sequence are most likely to show flaring activity (Pettersen, 1989).

The effects of flares can be observed in the whole range of the electromagnetic spectrum:

- Similar to the Sun, stellar flares can be observed using the *Hα* Balmer line. During stellar flares, the equivalent width of the line may increase up to an order of magnitude when considering dMe stars. Line broadening up to several hundreds of km/s are connected to turbulent mass motions or Stark broadening arising from increased electron densities (Haisch, Strong, and

Rodono, 1991; Kowalski, Hawley, Wisniewski, et al., 2013).
While flares are especially prominent in $H\alpha$, they also highly increase the emission in other chromospheric lines (Balmer series, Ca II H and K or He I), which have typical temperature ranges from 6000 up to 20000 K (Kowalski, Hawley, Wisniewski, et al., 2013). The search for these flares using Balmer lines on dMe stars is one of the main goals of the present work.

- While white light flares on the Sun are rare (and the disk-integrated additional flux of flares on the Sun are barely resolvable), there have been numerous detections of optical flares on other stars. dMe stars show optical flares that are up to 10 - 1000 times more energetic than their solar counterparts (Haisch, Strong, and Rodono, 1991).
- Solar flares observed in soft X-ray ranges ($1 - 8$ Å) build the basis of the solar flare classification (Haisch, Strong, and Rodono, 1991). A large variety of X-ray flares have been observed on stars using space borne telescopes (Güdel, 2004), ranging from extremely high fluxes (up to $10^{33}\ erg/s$, Preibisch, Neuhaeuser, and Alcala, 1995) to flares with durations of several days (Graffagnino, Wonnacott, and Schaeidt, 1995). The emission of X-rays during a flare is linked to coronal line emission with temperatures up to several million Kelvin (Welsh et al., 2006).
- Flares greatly enhance the UV and EUV emissions, as is observable on the Sun and other stars using space borne UV observatories (like the Solar Dynamic Observatory (SDO) for the Sun or GALEX for stars). UV radiation during flares corresponds to chromospheric and transition region temperatures up to 10^5 Kelvin (Welsh et al., 2006).
- Flares on both the Sun and stars are also visible in the radio ranges of the electromagnetic spectrum, arising from plasma properties in the stellar atmosphere (see for example Haisch, Strong, and Rodono, 1991 or Güdel, 2002).

Regarding their evolution, flare light curves usually exhibit two phases: the impulsive phase indicated by a fast rise, peak and fast decay (within several seconds) and a gradual decay phase afterwards (lasting for minutes up to hours). The Balmer lines show the same fast rise, but typically peak several minutes later than U-band emission peak. The flaring Ca II K line usually arrives at its peak later than the Balmer lines, while the latter are already at the gradual decay phase (Kowalski, Hawley, Wisniewski, et al., 2013).

Recently, high cadence and continuous photometric observations using spacecrafts in order to detect exoplanets (by transition method) gave rise to numerous observed flares (for example from Kepler or TESS , Balona, 2015; Davenport, 2016; Yang and Liu, 2019; Günther et al., 2019)

Observation of stellar CMEs

Observation of stellar CMEs proves to be far more difficult than flares. So far, there have been only few reportings of CMEs in the literature. Several methods were proposed and utilised to detect CMEs on stars:

- Doppler shifted signatures in emission or absorption lines:
  The idea is to find signatures corresponding to mass with velocities above the escape velocity of the star. A CME that is directed towards the observer should, in principle, result in an additional, blue shifted signature next to an emission or absorption line that is related to the CME. The observed velocity is in fact the line-of-sight or projected velocity given by the Doppler effect:
  $$v_{CME,projected} = c\frac{\Delta\lambda}{\lambda} \tag{2.21}$$
  Here, c denotes the speed of light, λ the wavelength of the related absorption or emission line and $\Delta\lambda$ the difference in wavelength between signature and the line.
  The real velocity is given by $v_{CME,real} = v_{CME,projected} / \ |cos(\theta)|$, with θ being the angle between the line-of-sight and the CME direction. CMEs that are directed perpendicular to the line-of-sight show no Doppler shifted signature and thus are not detectable by this method, even though they could create enhanced wings of the related absorption / emission line due to CME expanding in volume over time.
  In the optical wavelength range, prominent chromospheric lines like the Balmer lines are used to search for stellar CMEs, which is the method that is utilized in this thesis. The cores of CMEs are believed to be erupting prominences which consist of cool, chromospheric plasma visible in the Balmer lines. The same method can be utilised using (F)UV lines (as was done in Leitzinger, Odert, Ribas, et al., 2011). Here, it is assumed (as is valid for solar CMEs) that the stellar CME takes with it not only prominence material, but highly ionized coronal material as well. Thus, inferring mass estimation from Balmer lines alone underestimates the total mass of the CME, as it is only valid for the chromospheric plasma in the core.
  An important factor in searching for CMEs is the fact that flares can, on their own, produce line asymmetries due to chromospheric evaporation or condensation, while flares are the starting point to search for CMEs due to the high correlation between solar high energetic flares and CMEs (Yashiro and Gopalswamy, 2009). The distinction between asymmetry arising from a flare and a highly projected CME feature is therefore an issue.
- X-ray absorptions:
  Active regions visible in X-rays may get obscured by overlying mass of plasma. If this plasma is rising as part of a CME, the expansion gives a characteristic decay of the absorbing column density (Moschou et al., 2019).

- Coronal dimmings:
  On the Sun, EUV and X-ray dimmings are found in association with CMEs and are interpreted as density depletion during the beginning phase of a CME due to evacuation of plasma (e.g. Dissauer et al., 2018). However, this effect could also be explained by a temperature change of the coronal material.
- Type II bursts:
  Observable in radio wavelength ranges, type II bursts are recognised to be shockwaves in the solar atmosphere, possibly driven by the onset of a CME. So far, no type II radio bursts have been detected on stars other than the Sun (Moschou et al., 2019 and references therein).
- Pre- flare "dips" (following Osten and Wolk, 2017):
  Dimming of the star's light shortly before the start of a flare, explained by destabilization of an off-limb filament, bringing material in front of the stellar disk. A decrease in chromospheric line emission and Balmer continuum emission is expected. However, this feature could be explained otherwise (for example increase in H^- opacity during chromospheric heating).
- CME effects on stellar environments (following Osten and Wolk, 2017):
  Sudden disappearance of debris disk material in the stellar environment which could not be explained by radiation alone, as was reported by Melis et al. (2012).

There is also the possibility of no erupting CMEs at stars at all, which would render the activity in stellar atmospheres quite different compared to the Sun. Strong overlying magnetic fields on highly magnetically active stars may suppress CMEs, similar to some active regions observed on the Sun (see for example Thalmann et al., 2015). The possibilities of no CMEs and CMEs not being visible in the Balmer lines are elaborated in the discussion section of this work (Chapter 6).

3. Data

3.1. SDSS spectroscopic data overview

This work makes use of the optical spectroscopic data of the SDSS Data Release 14 (Abolfathi et al., 2018). The spectra were restricted to all stars of subtype F, G, K and M. The SDSS spectral classification was used, while all found objects showing high stellar activity were crosschecked for spectral classification from different catalogues. The provided SDSS spectra were available as .fits files [1]. Overall, 630162 spectra were available for the analysis. Stars that are specifically marked with luminosity class I, II, III as well as White dwarf stars were sorted out for this work. Every spectrum is a combination (co-added spectrum) of one or more single spectra. These spectra were usually observed within one hour up to several weeks. Only those spectra were used, where there are at least 3 spectra observed at different times to get information on the time evolution. Several co-added spectra of the same objects are possible, taken at different months or weeks. The exposure times are in the range of roughly 10 to 25 minutes for each single spectrum. The spectra are provided in units of spectral flux density $[10^{-17}\,\mathrm{erg\,s^{-1}cm^{-2}\AA^{-1}}]$ and the wavelength axis is given in vacuum wavelengths in the heliocentric frame (Stoughton et al., 2002).

The SDSS Data release 14 includes all the data from previous data releases, covering a wide range of different surveys and programs. Two spectrographs were used: the SDSS spectrograph covering Data Releases 1 - 8, including the original SDSS spectroscopical survey as well as both SEGUE surveys (Sloan Extension for Galactic Understanding and Exploration), and the BOSS (Baryon Oscillation Spectroscopic Survey) starting with Data Release 9. SDSS measures many targets at once using a plate with pre-drilled holes for each object on the observed sky patch. Optical fiber cables get plugged into each hole, which transfer the light-sources to the spectrograph. The original spectrograph could observe 640 objects at the same time with an optical range of $3800 - 9200$ Å. The BOSS spectrograph is able to observe 1000 objects at once with a slightly larger optical range of $3650 - 10400$ Å. Both give a spectral resolution of 1500 at 3800 Å and 2500 at 9000 Å. The red and blue part of the optical data is split at around 6000 Å (Ahn et al., 2012). One example of such a spectrum is displayed in Figure 3.1.

[1] Downloaded from https://data.sdss.org/sas/

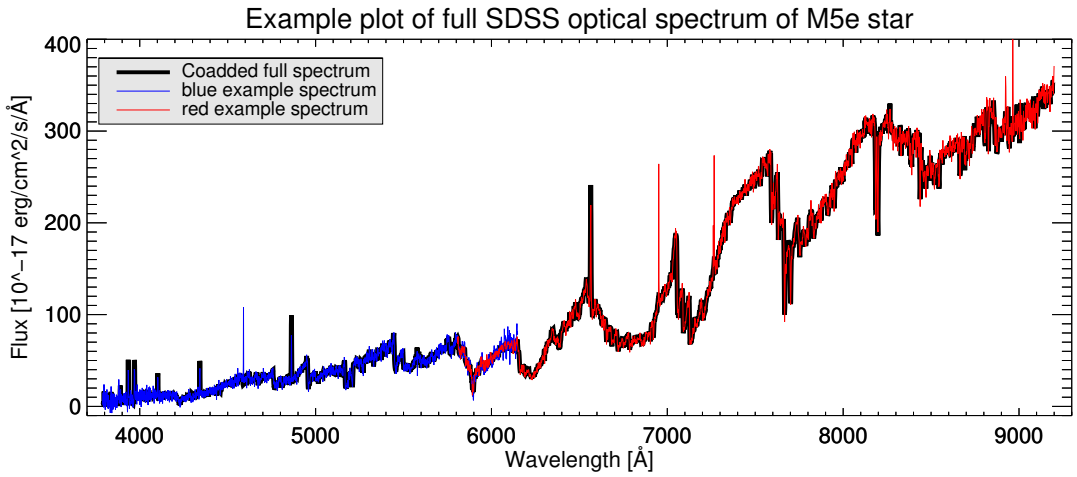

Figure 3.1.: Full SDSS optical range example plot of a magnetically active M4 star. The coadded spectrum (black) consists of several added spectra which are divided into a red and a blue part, overlapping around 6000 Å. One blue and one red single spectrum was plotted. Cosmic rays in the single spectra are visible.

Stellar Subtype	Summed exposure times per SNR bin [years] High SNR	Middle SNR	Low SNR	Worst SNR	Sum [years]
M	1.39	1.69	2.11	12.56	17.75
K	13.86	4.97	3.67	9.40	31.9
G	4.75	2.26	2.61	6.70	16.32
F	22.55	10.36	12.16	20.10	65.17
Sum	42.55	19.28	20.55	48.76	131.14

Table 3.1.: Summed exposure times of all stars in the dataset divided into stellar subclasses and SNR bins. The cutoff values defining each bin are given in section 3.3

Due to the high number of stars being observed simultaneously, the long runtime of surveys and cumulative datasets, the overall summed observation time of the stars in the present dataset amounts to more than 100 years. All pure exposure times of the files were summed and are listed in Table 3.1. Differences in exposure times between the red and blue spectrograms amount to overall difference in exposure times that is less than 0.01%.

3.2. Spectral classification

Both spectrographs used specific spectral templates for each stellar subtype, taking the template that's closest to the spectrum at hand to classify the star. While the original SDSS legacy surveys and the SEGUE had templates for dwarf stars of subtype of M0 - M9, BOSS only used a template for dwarfs stars of M1 type in the same classification region, leading to less late type M stars since SDSS

data release 9. All spectra were pre-selected by sorting out the luminosity classes I, II and III as well as all subdwarfs. It is noted, however, that most SDSS spectral classifications do not explicitly give a luminosity class.
The spectral type of every star that was found by the stellar activity search was checked using the catalogue by Skiff (2014) on VizieR [2], which works as a collection of known spectral classifications of different literature sources for each star. Using this catalogue, most objects were matched with the spectral classification of West, Morgan, et al. (2011), containing a catalogue of the SDSS M dwarfs up to data release 7 and used visual inspection of each object to determine the spectral type. The same catalogue was also frequently used for getting a rough value on distances if an object was not covered by GAIA data.

3.3. SNR bins

As this work mainly focuses on the variability of the Balmer lines, all the spectra were classified into different SNR bins by defining a SNR within +/- 200 Å of the $H\alpha$ line. The focus was laid on $H\alpha$ due to the better spectral resolution as well as more flux for late-type stars in this area, making the line more prominent above the noise of the continuum. The SNR was calculated by dividing each flux value point with its affiliated standard deviation and subsequently taking the mean of these SNR values over the aforementioned range. This was done for each single spectrum of a file. These SNR of the single spectra were averaged and afterwards classified into the following 4 bins:

- HIGH SNR bin: Averaged single spectrum SNR around $H\alpha \geq 20$ resulting in 197047 stars
- MIDDLE SNR bin: Averaged single spectrum SNR around $H\alpha$ between < 20 and ≥ 15 resulting in 88144 stars
- LOW SNR bin: Averaged single spectrum SNR around $H\alpha$ between < 15 and ≥ 10 resulting in 90119 stars
- WORST SNR bin: Averaged single spectrum SNR around $H\alpha \leq 10$ resulting in 254852 stars

Figure 3.2 shows the abundances according to the SDSS spectral classification for each SNR bin. For this work in particular, a closer look into the abundances of later K and M subtypes is of substantial importance. Figure 3.3 shows the number of stars according to their K and M star spectral subtype classification. As was mentioned in section 3.2, this classification is dependent on the spectral templates used by SDSS. Since BOSS changed the spectral templates, some subtypes are either over- or underrepresented in the data. Both Figures 3.2 and 3.3 show, that the later spectral subtypes are mostly prevalent with bad SNR, as was expected

[2] https://vizier.u-strasbg.fr/viz-bin/VizieR

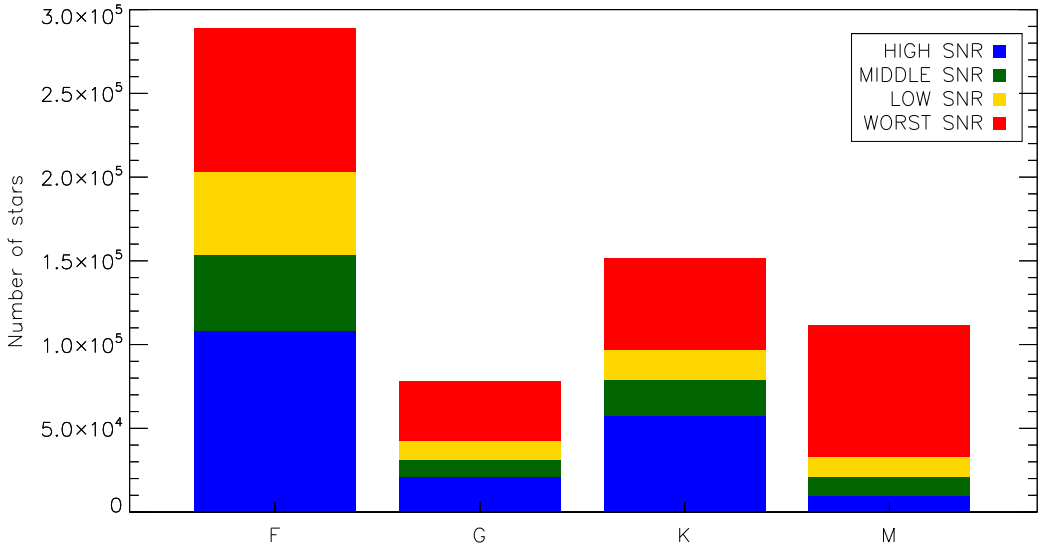

Figure 3.2.: Abundances of stellar subtypes per each SNR bin. Spectral classification according to SDSS.

from their low luminosities. This fact renders statements regarding their activity statistics more difficult.

3.4. Resolution, Cosmic rays and flags

As the main goals of the past and current SDSS programs did not focus on late type dwarf stars, the resolution of the available spectra is not optimized to analyse stellar activity. Nevertheless, This survey was chosen due to the large quantity of available spectra and the dataset has already been proven to be suitable to find stellar activity (e.g. by Hilton et al., 2010). This work mainly focuses on the analysis of the $H\alpha$ and $H\beta$ lines due to the better SNR in those ranges (valid for late type star spectra). With a given approximated spectral resolving power R = 2000 within both Balmer line ranges, we get a resulting minimal spectral resolution of $\sim$ 3.3 Å around $H\alpha$ and $\sim$ 2.4 Å around $H\beta$ (approximately two times oversampled in both ranges). The exposure times are, as already mentioned, in the range of 10 - 25 minutes. Several consecutive 10 minutes exposures are therefore the best time resolution possible in the data, while spectra of the same object at a different time may be used as reference for the quiescent spectrum.
Cosmic rays are visible in the data, usually compromising two consecutive datapoints. In further analysis, every spectrum was analysed by eye to rule out cosmic rays giving false positives in the stellar activity search. SDSS is providing flags for each datapoint, giving information on occurring problems. These flags are resourceful in noting big cosmic rays as well as spectra with general problems

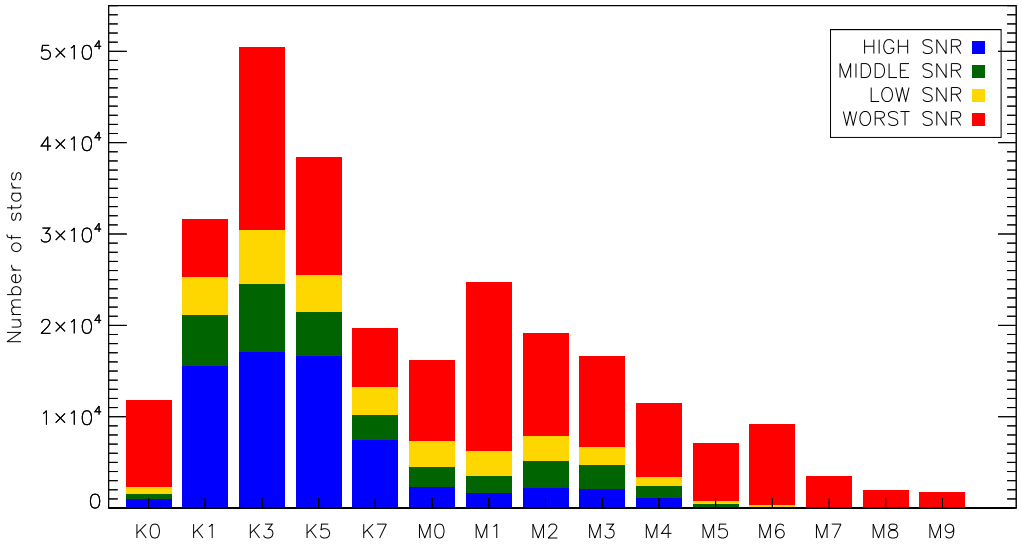

Figure 3.3.: Abundances of stellar K and M subtypes per each SNR bin. Spectral classification according to SDSS.

while, on the other hand, stellar activity is also flagged (due to sudden changes from one spectrum to another, as well as big differences to the reference spectrum). Therefore, the consideration of flags and ruling out of cosmic rays was done after the first search for stellar activity, as the SDSS pipeline does not take activity into account. More background information on the pipelines, calibration and flags of the spectroscopic data can be found in Stoughton et al. (2002).
Errors in the spectra are estimated as 1σ standard deviations per pixel, assuming a normal distribution for each pixel. These errors are available as inverse variances in the .fits files.
The given wavelength solution for the datapoints is using a vacuum wavelength scale (important vacuum wavelengths: $H\alpha = 6564.61$ Å, $H\beta = 4862.68$ Å, $H\gamma = 4341.68$ Å, Stoughton et al., 2002). The spectra were slightly adjusted to match telluric lines and to correct to the heliocentric frame, reporting an accuracy of the wavelength calibration of 10 km s^{-1} or better (Stoughton et al., 2002).

3.5. Affiliated GAIA Dr2 data

In addition to the information that SDSS provides for each object, this work makes use of the second GAIA data release [3]. GAIA DR2 gives information on position and apparent G magnitudes for approximately 1.7 billion sources, parallaxes of 1.3 billion sources as well as apparent red and blue broad band color magnitudes

[3] http://cdsweb.u-strasbg.fr/gaia

for 1.4 billion sources (Gaia Collaboration et al., 2018). Only sources brighter than 21 magnitudes are considered.
To match each of the 630162 spectroscopic sources from SDSS with their GAIA DR2 counterparts, a VizieR search within the GAIA DR2 catalogue was conducted for the position of every single SDSS source. The used search radius was 4 arcseconds. GAIA G magnitude information is available for approximately 591000 stars in our sample (corresponds to $\sim$ 94 %), while BP-RP color information is available for $\sim$ 90 % of the stars in the sample . Apparent G band magnitudes and parallaxes combined are available for approximately 480000 stars ($\sim$ 76 %).
Figure 3.4 shows the HRD color plot of our sample. Here, the respective errors for both the BP - RP color as well as the absolute magnitude were restricted to be less than 1 magnitude. This restriction reduces the plotted sample to approximately 121000 stars or $\sim$ 19 %. It is important to note, that this plot represents the HRD of our sample only. It is not suited to make assumptions on galaxy wide stellar populations in general due to the sorting effect of only using specific SDSS spectra (see sections 3.2 and 3.3).
The distances were calculated using the simple relation of inverting the GAIA DR2 parallax (in units of arcseconds) to get the distance (in units of parsecs). While there are more sophisticated methods to get the correct distance from GAIA DR2 data (see Bailer-Jones et al., 2018), the resulting difference in values between this work and the one from Bailer-Jones et al. (2018) are all expected to lie within the parallax errors provided by GAIA DR2. These parallax uncertainties are used throughout this work.
While the crossmatching of our objects with the GAIA DR2 catalogue is valid for the majority of the stars, some special cases prevail (e.g. the possibility of two GAIA sources within 4 arcseconds). In the following analysis of stars with found stellar activity, every object was analysed in detail to rule out or otherwise note such cases.

3.6. Data preparation

The searching methods (see next chapter) were implemented using fitting algorithms for Balmer lines. To correctly perform these fits, the spectroscopic lines were normalized to a constant continuum (equaling 1).
Ranges where the line region and the surrounding continuum regions are lying were defined. These regions were adopted from Hilton et al. (2010) and are listed in Table 3.2.

For each Balmer line, the mean value of both associated continuum regions were taken and used to calculate the linear normalization line. The measured flux values were divided by this line, leading to a normalized profile of the Balmer line (see Figure 3.5).
Problems using the normalization occurred at spectra with low flux close to zero.

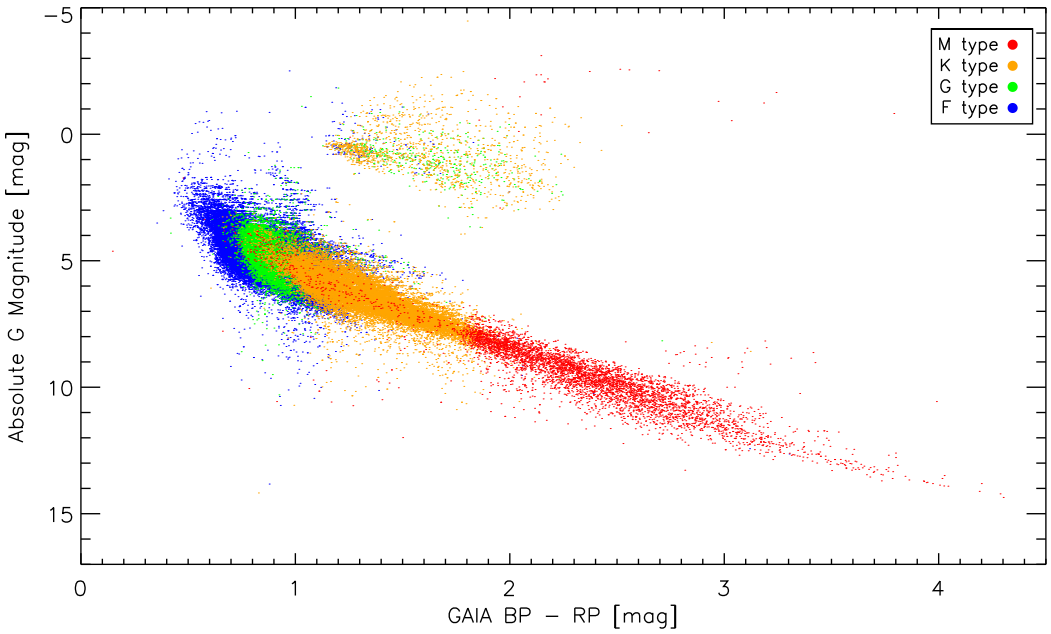

Figure 3.4.: HRD of the SDSS sample with errors < 1 mag in both axes.

Line	Continuum 1 (Å)	Line region (Å)	Continuum 2 (Å)
$H\alpha$	6500 - 6550	6557.61 - 6571.61	6575 - 6625
$H\beta$	4810 - 4850	4855.72 - 4870.00	4880 - 4900
$H\gamma$	4270 - 4320	4331.69 - 4350.00	4360 - 4410

Table 3.2.: Line and Continuum regions for Balmer lines, adopted from Hilton et al. (2010)

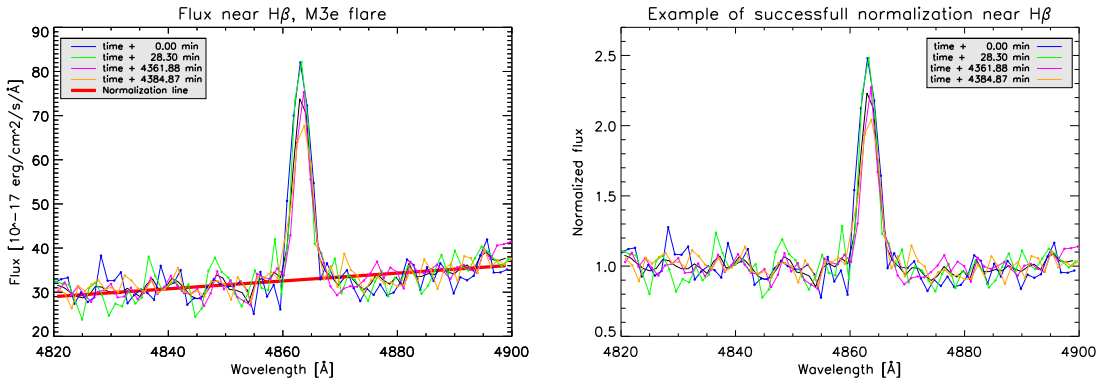

Figure 3.5.: Example of successful normalization. The normalization line is plotted in red.

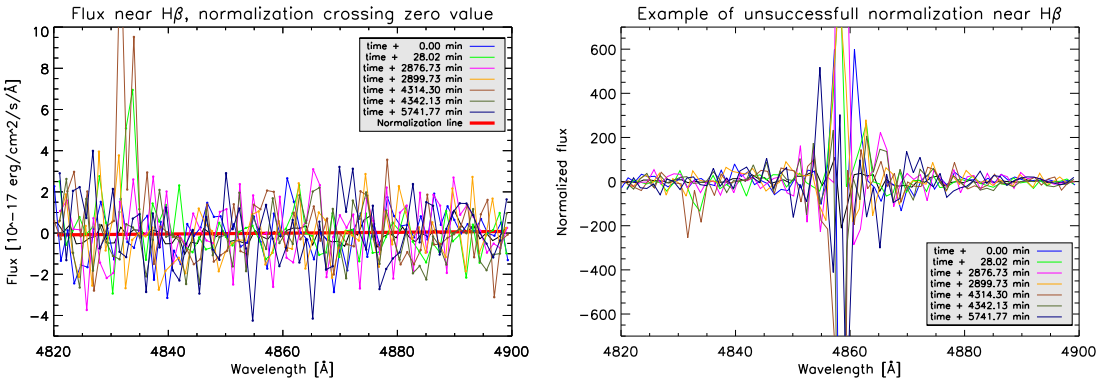

Figure 3.6.: Example of unsuccessful normalization. The low flux leads to the normalization line (red) crossing the zero-value, causing huge normalized values.

Noise even gave rise to nonphysical values below zero. The normalization line (indicating the level and slope of the continuum) therefore lies around the value of zero, sometimes even crossing the zero axis. Division by this normalization causes the resulting normalized spectrum to have a huge jump due to division of values near zero (see Figure 3.6).

4. Methods

The available SDSS spectra in form of .fits files were analysed using Interactive Data Language (IDL). Object oriented programming was used, creating a new class object for each SDSS spectrum, which automatically reads in all single spectra with their header information as well as normalizing the Balmer lines in every single spectrum. Get-functions were used to read out the values and errors as well as exposure times, spectral type and flagging bitmasks. The .fits files have several Header Data Units (HDUs) which were all necessary to read in for the data analysis, therefore the usage object oriented programming simplified and streamlined the search and evaluation algorithms. Files were identified by using the SDSS designation of Plate-MJD-Fiber numbers, giving a clear identification for each combined spectrum.
Several programs for different tasks were made (e.g. calculating and sorting for SNR bins, searching methods for flares and CMEs, visual inspection programs, energy and error calculations, plotting algorithms). All programs are available in the IGAM (Institutsbereich für Geophysik, Astrophysik und Meteorologie) archive.

4.1. Flare detection methods

4.1.1. Peak variability search

Using the normalized co-added spectrum as well as the normalized single spectra, the $H\alpha$ and the $H\beta$ Balmer lines were fitted by a simple Gaussian curve for already normalized spectra:

$$I = 1 + I_0 \quad exp\left(\frac{(\lambda - \lambda_0)}{\sigma}\right)^2 \tag{4.1}$$

Here, I_0 denotes the line amplitude, λ_0 the wavelength of the line core and σ the width of the Gaussian. These 3 parameters were fitted and reasonable initial start values ($I_0 = 0.0$, $\lambda_0 =$ Balmer line core value, $\sigma = 4$ Å) were chosen. All values around 5 Å of the core wavelength of each Balmer line were used in the fit.

Activity in $H\alpha$ was defined as the change of the fitted Gaussian peak from one time instant to another above two times of the peak error that resulted from

the Gaussian fitting algorithm, using all errors from each considered datapoint. The peak error is determined by using Gaussian error propagation with the peak errors from both fitted Gaussian that are compared with each other. This is basically an algorithm that is using thresholding depending on the errors and significance of the Gaussian fit. To rule out nonphysical line fits, the resulting shift of the line core in the x-axis is demanded to be less than 2 Å from one time instant to another.
Due to low SNR, spectral resolution and the possibility of outliers in the data, a significant change of the $H\alpha$ line alone is not enough to sufficiently declare the spectrum as flaring. Therefore, the same algorithm was used on $H\beta$ as well. Due to higher noise around $H\beta$ compared to $H\alpha$, this second condition further lowers the number of eligible events compared to using only $H\alpha$. A star was defined to be in flaring state, if both the fitted $H\alpha$ and $H\beta$ lines show peak height variations above 2 times the peak error.

The reasoning behind using this method was based on following aspects:

- The cores of Balmer lines are following Gaussian curves arising from Doppler broadening.
- The fit is more robust against outliers (e.g. CRs) and is therefore a better representation of the overall line shape.
- Trends in the wings and outside of the Balmer lines are ignored. Especially late type M-stars show heavy contamination of other lines (e.g. molecular bands near $H\alpha$.
- It is highly unlikely that both $H\alpha$ and $H\beta$ change significantly above the peak change errors in the same time instance without flaring activity.

On the downside, the line core fitting algorithm overestimates its fit significance for spectra with really low SNR by ignoring the noise around the Balmer lines. False positives that were found this way were sorted out during the visual analysis of each event. The fit function could also lead to false fits due to big outliers, faulty or missing datapoints. Due to the spectral resolution of the SDSS spectra, the Balmer line cores (e.g. for M stars) usually consist of less than 10 datapoints. CRs usually affect between 2 and 4 pixels of the camera on the spectrograph. Depending on the position and size of the CR hit, false datapoints may have similarities to emission lines. The SDSS data pipeline flags outlying datapoints, often leading to the flaring pixels to be also flagged as false datapoints.

The same algorithm was performed with a lower threshold of 1.5 times of the resulting peak error, which resulted in a larger list of flaring stars (also containing the previously found ones). Afterwards, a visual inspection of the flares was done to check each event in more detail (see section 4.1.4).

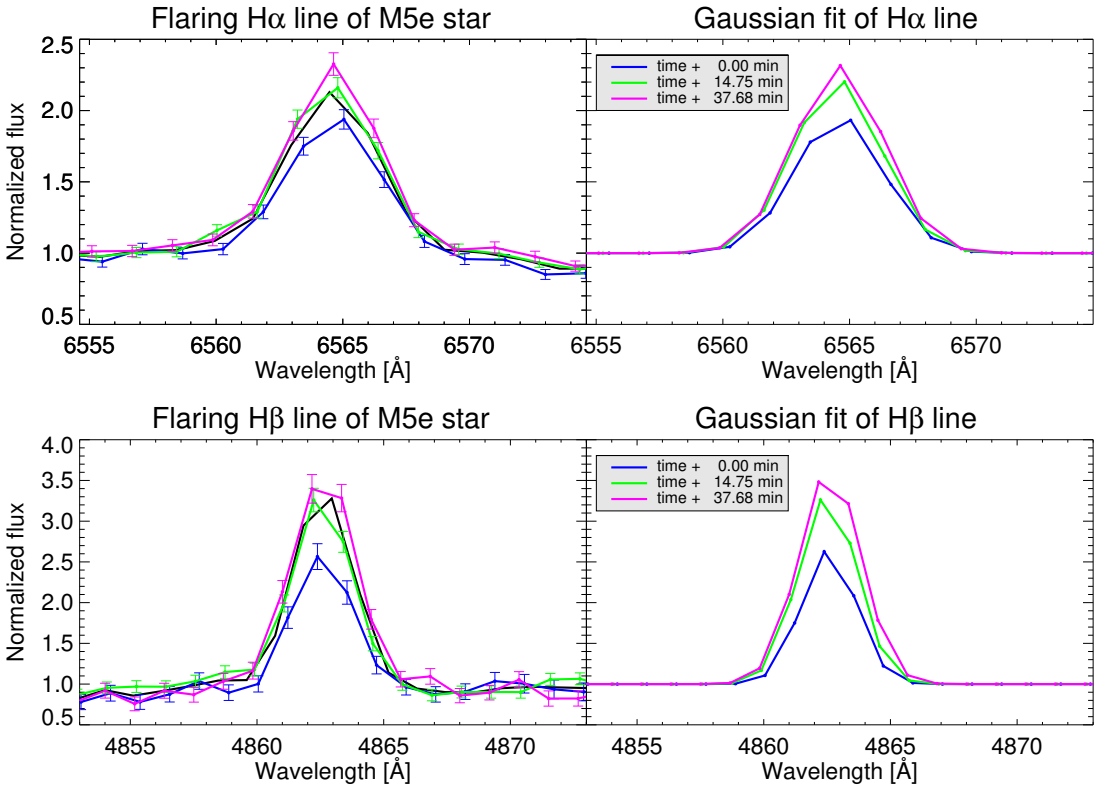

Figure 4.1.: Example of a flare detected on a M5e star in both $H\alpha$ and $H\beta$. The Gaussian fits that led to the detection are displayed for each single spectrum. Errorbars for the normalized flux values are given.

4.1.2. $H\alpha$ emission line search

High noise and changes in the wings could lead to missing flares in the core fitting search algorithm. Using the fact that stars that show big Balmer emission lines are magnetically active and therefore the probability of flares is much higher, a search for a high emission line in $H\alpha$ was started. Here, the Gaussian fitting algorithm (equation 4.1) is again used, but this time all stars are noted that show an emission line that is at least greater than 1.5 times the normalized continuum value. The resulting list of stars were then manually searched for changes from one time instant to another.

4.1.3. Usage of other fitting functions

As an alternative to the Gaussian function to fit the peaks, a so-called Moffat function was tested. It is used to accurately describe stellar point spread functions (PSFs) and has a core similar to a Gaussian while also accounting for broader wings. The implementation was done using the following equation for the intensity:

$$I = I_0 \left[1 + \left(\frac{(\lambda - \lambda_0)}{\sigma}\right)^2\right]^{-\beta} \tag{4.2}$$

Here, I_0 denotes the continuum flux, λ_0 the wavelength of the line core, σ a factor determining the width of the function and an exponent β. These 4 parameters were subsequently fitted by a fitting algorithm. Reasonable initial start values were chosen.

The Moffat fitting algorithm was ultimately unsuccessful and not further used in the flare search and analysis. Approximately 1 out of 5 spectra (from spectra with good SNR) were fitted incorrectly. Presumably this problem arose from high errors and noise (especially in the wings) leading to false fits. In this way, the Moffat fit proved to be unreliable compared to the Gaussian fit for this dataset.

4.1.4. Visual inspection of the flare candidate spectra

After obtaining lists of flaring candidates by the aforementioned algorithms, each star was checked manually to determine whether the flare is valid considering following aspects:

- Sorting out spectra with obvious data problems (e.g. one spectrum with completely different spectrum or severe cosmic ray hits)

- Is the peak change significantly above the surrounding noise in both $H\alpha$ and $H\beta$? Considering the relative flare peak height, every event was marked with an own categorization in either "no", "mini", "small", "middle" or "big" flare. Only the latter three categories were considered in the subsequent in-depth flare analysis. Error bars of the individual datapoints were considered.
- Is there visible activity in other Balmer Lines (especially $H\gamma$)? Results were noted, stars with no visible activity in other lines while having sufficiently good SNR were sorted out.
- Datapoint flags for each $H\alpha$, $H\beta$ and $H\gamma$ line were controlled. While flares are usually automatically flagged, there are several other aspects and problems resulting in flagged datapoints. Individual flags were controlled and spectra with plenty of flags were noted. Considering this information in combination with the aforementioned aspects, each spectrum was then categorized in three groups "Yes", "Probable" or "No" to indicate, whether the spectrum should be considered or discarded from the flare list. The stars in the category "Yes" are considered to show distinct flares. The spectra in the "Probable" category show clear activity in (at least) both $H\alpha$ and $H\beta$, but more caution in handling them is appropriate. They either show no visible activity in $H\gamma$ (due to high noise) or they have a several or all of the datapoints in one emission line flagged, indicating a problem with this part of the spectrum. In these cases, all Balmer lines on the blue spectrum as well as the Ca II H and K lines were checked. Only those events were kept in the list that clearly resembled usual flaring behaviour.
- Crosschecking with flares identified in Hilton et al. (2010) to check, whether a flare was mistakenly sorted out by one of the aforementioned aspects. These events were then reevaluated.

Based on this, a final list of flare contenders was created. This list built the basis for further in depth-analysis.

4.2. CME detection methods

4.2.1. Wing variability search

Enhanced datapoints in wings

To search for CMEs, the change of height of the datapoints in the far wings of $H\alpha$ and $H\beta$ were controlled from one time instant to another. A datapoint was noted, if the value difference was higher than the added errors of both datapoints. An error-scaling factor was introduced as an additional optional parameter, but it was usually set to unity. A possible CME-like feature detection was reported, when one or more datapoints on the same wing changed from one time instant to another in both $H\alpha$ and $H\beta$. Instant manual controlling by automatically plotting

the spectra and indicating all enhanced points was performed.

This algorithm on its own was deemed to be not suited to search for CMEs on its own, due to the high abundance of CRs and the noise in the dataset, resulting in more (and almost exclusively false) findings than one could possibly go through manually. It was mostly used on the flare-search results and also as a controlling program to go through spectra with possible CME-like features to test, whether particular enhancements are indeed significantly higher. It was successfully tested on an additional blue wing feature in the data from V 374 Peg presented in Vida, Kriskovics, et al. (2016).

"CME-train" search

To detect enhanced or reduced wings, two windows were defined covering the far red and blue wings of both $H\alpha$ and $H\beta$. An algorithm was programmed which determined whether several successive datapoints (a "train") changed significantly from one time instant to another. The code from the previous section was used and improved by testing for successive enhanced datapoints, reporting all "trains" that exceed a pre-defined length. Train-sizes of 5 Å and 3 Å were tested. The finding of one train in a spectrum triggered a detection, which was subsequently controlled manually.
The idea behind this method was to find wide additional emissions like the one found by Houdebine, Foing, and Rodono (1990). The algorithm was also successfully tested on an additional blue wing feature in the data from V374 Peg presented in Vida, Kriskovics, et al. (2016).
This algorithm holds two weaknesses: slow changes are not recognised, and one single datapoint in the whole enhanced train with larger error or with a slightly lower value may prevent a detection. The results mostly consisted of either huge cosmic ray hits or spectra showing completely different flux levels at one time instant due to faulty data reduction. Figure 4.2 shows a prime example of these false detections. While common CRs enhance two or three datapoints, these unusual high and wide CR enhancements may arise from saturation of a pixel, leading to an overflow of charges into the next pixel.
One exception in the findings (see section 5.2.4) could not be explained by faulty data.

4.2.2. Wing asymmetry search

To detect asymmetries, a window at the left and the right wing of the normalized $H\alpha$ line was defined and the mean value of the flux within this window was determined. These two levels were then compared, and significant differences were searched.

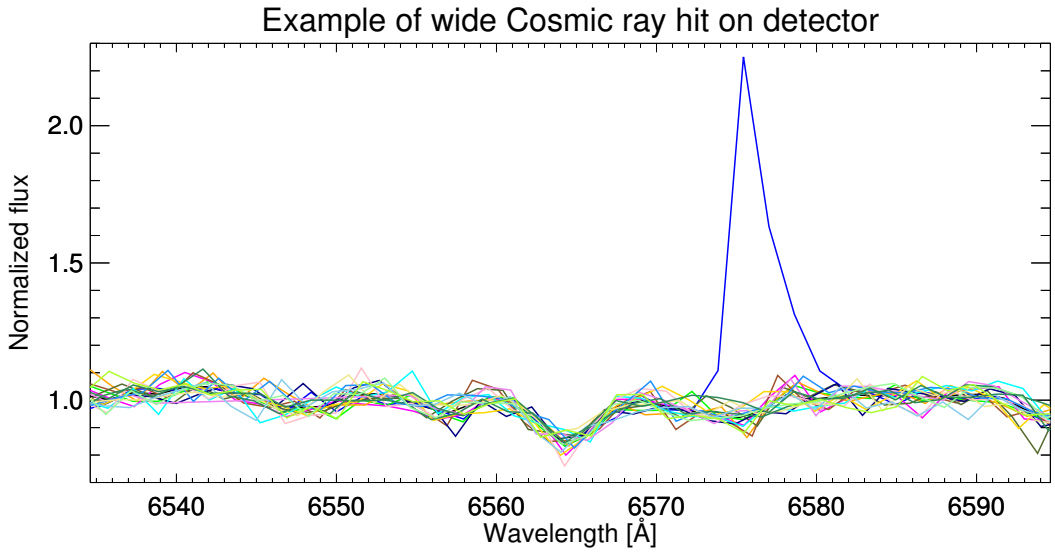

Figure 4.2.: Example of a CME false detection showing an extraordinary big cosmic ray hit on the detector.

This method to detect asymmetries was deemed unsuccessful due to high noise of the data, bad spectral resolution and contamination of other lines and molecular bands near the $H\alpha$ line. Visual inspection led to more findings of asymmetries in the spectra.

4.2.3. Manual search from flare events and high emission lines

Additional to the methods described in the previous chapters, a manual search for enhanced wings was performed accompanying the manual flare search described in section 4.1.4. This search was done for all spectra found by the the flaring and high emission line algorithms. Every spectrum showing an asymmetry in one of either $H\alpha$ or $H\beta$ was noted. Spectra with asymmetries in both lines were recognised as possible CME candidates and analysed in more detail. In these cases, the $H\gamma$ line and additional Balmer lines were included in the analysis, while all datapoint flags and errorbars were controlled. Figure 4.3 shows an example of such an asymmetry found during the flaring phase of a star.

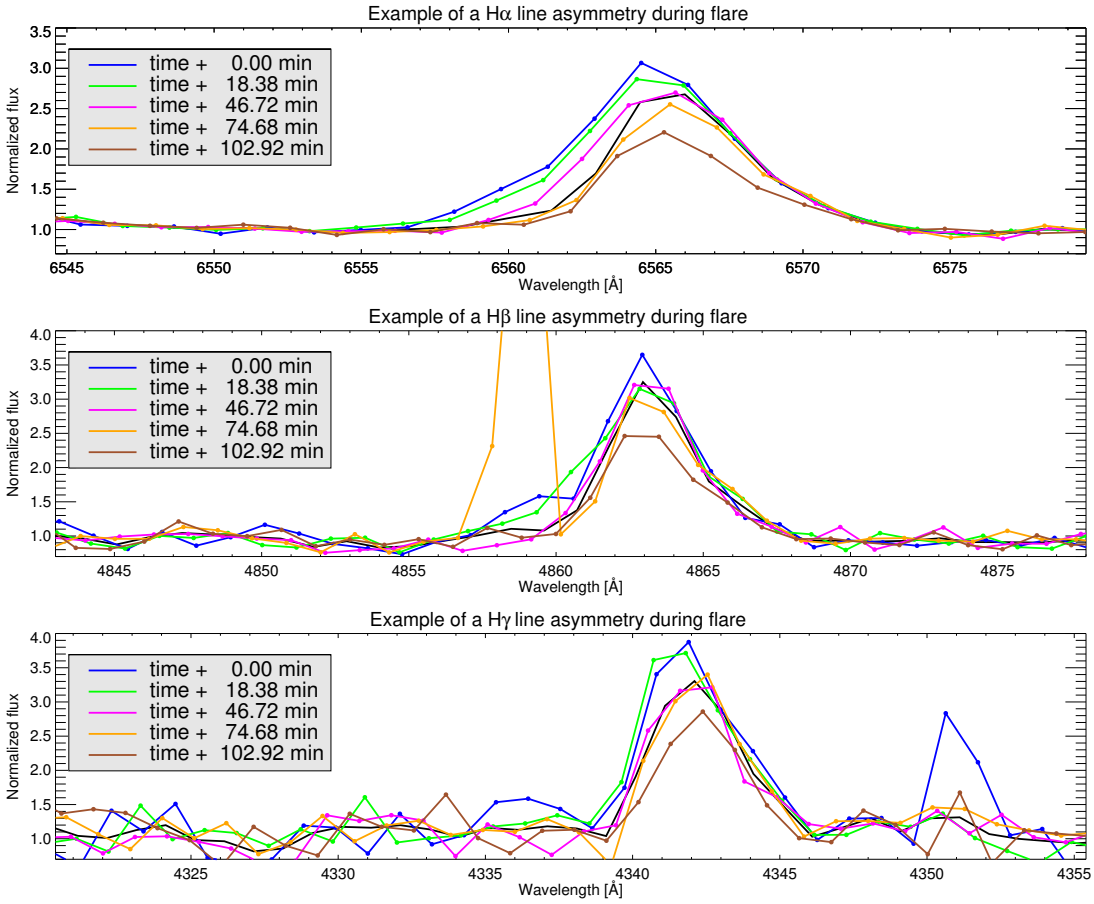

Figure 4.3.: Example of a found asymmetry during a flare on the star "Kiso A-0903 163", an emission line star of spectral type M4V.

5. Analysis and results

This section describes the results of the flare and CME search methods as well as the subsequent analysis of the findings.

5.1. Flare search results

Utilizing the methods mentioned in section 4 resulted in a list of flare candidates, sorted by each SNR bin.
The final list consists of 274 flare events on M dwarfs, 4 on K Stars and 3 on T Tauri stars. The search for flares using this method did not yield any results for dwarf stars of the types G or F, therefore, only K, M and T Tauri stars are covered by the analysis.
Table 5.1 shows all found flares per spectral subtype listed for each SNR bin. Two stars in the M0 categorization were originally denoted as K type in SDSS. This is discussed in section 5.1.6, as the classification bears some ambiguity. Three stars originally denoted as M type main-sequence stars were found to be T Tauri stars.

The raw algorithm searching for Gaussian peak differences (using higher threshold of 2 $\times$ peak error) found 538 flaring candidates on M stars (183, 90, 73 and 192 flares for high, middle, low and worst SNR, respectively). The same algorithm using lower threshold (1.5 $\times$ peak error) found 420 M star flare candidates (9, 10, 35 and 366 flares for high, middle, low and worst SNR, respectively) in addition to the flares found via higher threshold. For K type stars, the higher threshold method found 47 candidates (19, 17, 6, 5 flares for high, middle, low and worst SNR, respectively) while the lower threshold found additional 132 (18, 22, 15 and 77 flares for high, middle, low and worst SNR, respectively). All of the 54 detections on G stars and 169 detections on F stars were considered to be non flaring (or other type of star) after inspection.
Using high $H\alpha$ emission line search on M stars, the algorithm found 177 in the high SNR, 146 in the middle SNR, 203 in the low SNR and 5049 in the worst SNR bin. These numbers include several stars that were already detected via Gaussian peak difference. These detections were inspected manually to search for flares except for the detections in the worst SNR bin, which proved to be too large of a dataset with too many false emission line detections, which renders a manual search through the list neither efficient nor reasonable. Most of the found

SNR bin	K3	K7	M0	M1	M2	M3	M4	M5	M6	M7	M8	M9	TT	Total
high	1	3	3	0	4	6	35	29	19	5	0	0	2	107
middle	0	0	0	1	0	3	3	15	13	3	1	0	1	40
low	0	0	0	0	1	2	4	2	16	14	1	1	0	41
worst	0	0	0	0	0	2	1	5	30	29	9	17	0	93
Total	1	3	3	1	5	13	43	51	78	51	11	18	3	281

Table 5.1.: Spectral type of found flaring stars per SNR bin.

SNR bin	Gauss peak diff, high	Gauss peak diff, low	Emission line	Re-eval.	Other	Total
high	99	5	2	0	1	107
middle	38	1	0	1	0	40
low	32	4	3	2	0	41
worst	67	24	1	1	0	93
Total	236	34	6	4	1	281

Table 5.2.: Number of flaring stars found by each method per SNR bin. The one flare in the "Other" category was found by an older search on a K star based on $H\alpha$ activity only.

candidates in the other SNR bins appeared to be in fact active stars showing high emission lines. For K stars, this search yielded 167 candidates (147 from the worst SNR bin alone), but almost the entirety of these detections have their origins in false data values. For the same reason, going through findings for F and G stars was not reasonable (while real findings were highly active binary objects like cataclysmic variables).

The flare list in Table 5.1 is the result of a conservative approach during the manual inspection of the flare candidates, ruling out all flares that were considered to be too small. Several spectra were also sorted out during the subsequent in-depth analysis (see 5.1.1).
Table 5.2 lists the final number of flares that were found by each method, showing that the Gaussian peak difference with high threshold proved to be the most successful flare search method in this work.

5.1.1. In-depth analysis of flare result list

The in-depth analysis of each event covered the following methods and aspects:

Flare inspection and evolution estimation:
The $H\alpha$, $H\beta$ and $H\gamma$ Balmer lines were inspected and the evolution of the flare was estimated by grouping every event into the following categories: "Rise", "Decay", "Both", "Activity at different time" and "Other". If a spectrum showed unusual behaviour or if further information was necessary, the whole available

spectrum and especially the other Balmer lines were checked. Spectra with unexpected values were also crosschecked using the SIMBAD and VizieR catalogues. Thereby, 8 stars classified as M dwarfs by SDSS were identified as either cataclysmic variables (CV) or close/eclipsing white dwarf - M star binaries and were removed from the initial flare event list. CVs are identifiable by their emission lines shifting within a short period of time and the strength of the lines undergoing large (periodic) changes. The orbiting period can be estimated for CVs with sufficient consecutive spectra by looking at $H\alpha$.

Crosschecking every star using catalogues within VizieR:
The coordinates extracted from the header of each spectrum file were used to perform a VizieR crosscheck with both the Gaia DR2 (Gaia Collaboration et al., 2018) and the SDSS photometric catalogue release 12 (Alam et al., 2015). Each search was conducted within 5 arcseconds around the given coordinates. 272 stars in the M dwarf flare list were found in the Gaia DR2, 252 of which also include information on the star's parallax. For the flaring K stars, all 7 objects had associated Gaia parallaxes. Stars with missing parallaxes were checked for other sources within VizieR and, if possible, a value for the distance/parallax was added (these instances are marked separately). Another crosscheck was made using the catalogue of spectral classifications (Skiff, 2014), which serves as a compilation of known spectral classifications from literature. This catalogue was used to indicate whether the SDSS spectral classification is mostly valid and if otherwise to use the classification from literature that was especially dedicated to do spectral type classifications. 253 of the 281 flaring stars could be found within this catalogue. Missing stars were again checked for other sources.

Obtaining flaring time instances and their respective power values:
In a final manual inspection of the flaring events, every spectrum that was considered to be in flaring state as well as the reference spectrum was noted. Cosmic ray hits surrounding $H\alpha$ were also noted and whether they hit a flaring spectrum or the reference spectrum. Information on whether the flare is happening in consecutive time instances or at separated times is gathered. The reference spectrum was marked if it appears to be in a quiet state (which was also crosschecked with the events from Hilton et al., 2010). This information led to the overall number of flaring spectra and the overall flaring time as well as the automatic calculation of the $H\alpha$ power and the $H\alpha$ energy that was released during each flare.

5.1.2. Flare evolution results

The results of the flare evolution estimation is summarised in Table 5.3. These results were crosschecked with the overlapping flares form Hilton et al. (2010), giving the same results.

	Rise	Decay	Both	Activity at different time	Other	Total
Number	82	67	55	67	10	281

Table 5.3.: Flare evolution estimation of all 281 flares, including both M and K stars.

The overabundance of rising flares compared to decaying flares (which is contrary to the expected result) is most probably an effect of the data and the search method. The short rising period of the flare, which is expected to last less than 10 minutes, may be shorter than the exposure times (up to 25 minutes) of the single spectra. As a result, the first spectrum may show a lower integrated flux due to the integrated mix of quiet and rise phase, while the subsequent spectrum shows a higher flux due to the slowly diminishing higher flux level during the decay. This gives the impression of a peak happening later in the data. A second factor is that the searching method is most sensitive to high changes in consecutive spectra. Decaying spectra may show too little changes to get detected due to the slow evolution.
The introduction of the quiet flag was made in addition to the flare evolution. Spectra were considered to be quiet, when at least two of them at a different time series than the flaring spectra show no temporal changes. Spectra were considered to be probably quiet, when they appear before or after a consecutive flaring series without showing any temporal changes. Of the 281 events, 59 show quiet spectra and 64 show probable quiet spectra.

5.1.3. Flaring fraction per stellar subtype

To get an estimate on the flaring fraction, the flaring times of all events were summed for each stellar subtype and divided by the overall exposure times of said subtype. The flaring percentage of the later M type stars is highly dependent on whether a possible flare was detected despite the bad SNR. There are not enough flares found on earlier spectral types to make meaningful statistics like flaring fraction.
Figure 5.1 shows the results of each flaring fraction per subtype. These results were plotted for each SNR bin to get an overview on the influence of bad SNR. The "High" and "Middle" SNR bins are naturally more reliable than the other bins. No flare on a M8 or M9 star was detected in the high SNR stars, which is again a consequence of their low flux. Overall, the flaring fraction appears to rise for later type stars.
It is important to note that the overall exposure times per subtype was based on the original SDSS classification, while the flaring stars are classified using several sources as is described in section 5.1.1. The large flaring fraction reaches high values (up to 55 % for type M7) due to very little late type stars being in these SNR bins (only $\sim$ 10 stars of type M7 stars in "High"). Here, the mix of different

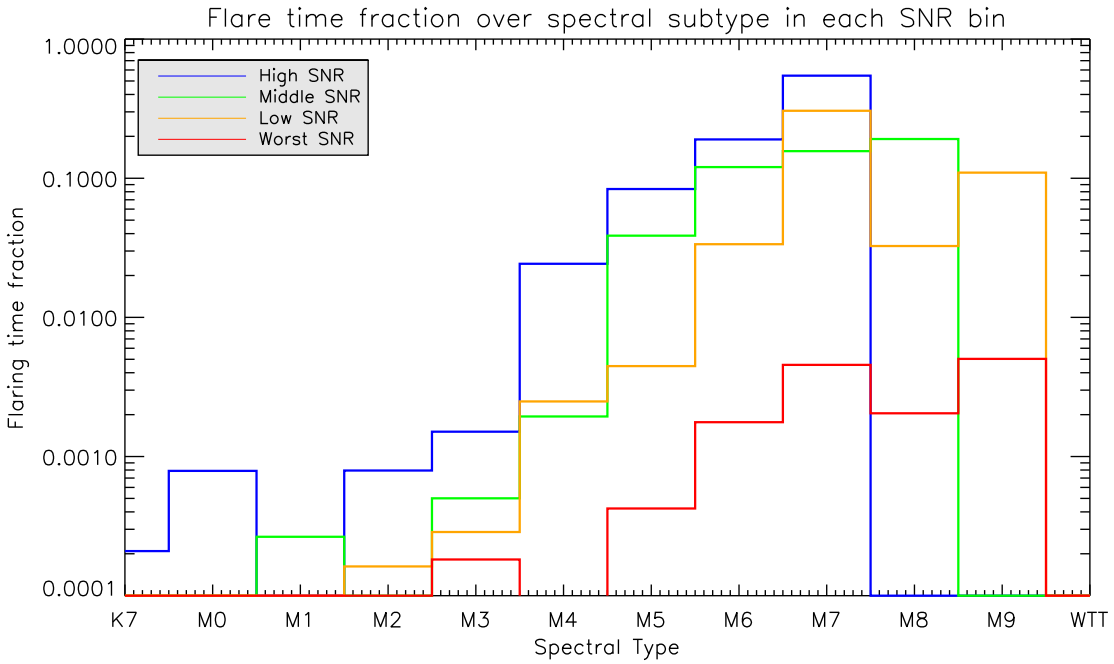

Figure 5.1.: Fraction of observed flaring time compared to overall exposure time in the dataset. Normalized to each spectral subtype.

spectral classifications may compromise the absolute values while the overall trend is valid.

5.1.4. Positions in HRD and sample purity

Using the data given by GAIA DR2, one can plot the position of the flaring stars in the HRD. The basic idea behind this is to test whether the stars in question are in fact late type dwarf stars, resulting in a high sample purity.
Figure 5.2 shows the flares in the HRD, using both their absolute G magnitude derived from GAIA DR2 and their GAIA B - R color. Missing and large error values for the color axis is the major constraint in this plot (see also Figure 5.5). Most of the displayed stars lie well within the main sequence. Some stars are above the M star main-sequence region. These indicate pre-main sequence stars (T Tauri stars), one of which was confirmed to be one. None of the present stars in this plot show signs of being an evolved star on the RGB.

Figure 5.3 shows all M stars in the dataset with their GAIA G magnitudes over their distances. All flaring stars are displayed as well, indicating that all flaring M stars are well within 1000 parsec. The G magnitude of a solar-like star was printed as a function of the distance to give a distinction line between stars with sub-solar luminosity (like M dwarfs) and stars with higher than solar luminosity (like red giants). The function of a well known M5.5 dwarf (Proxima Centauri)

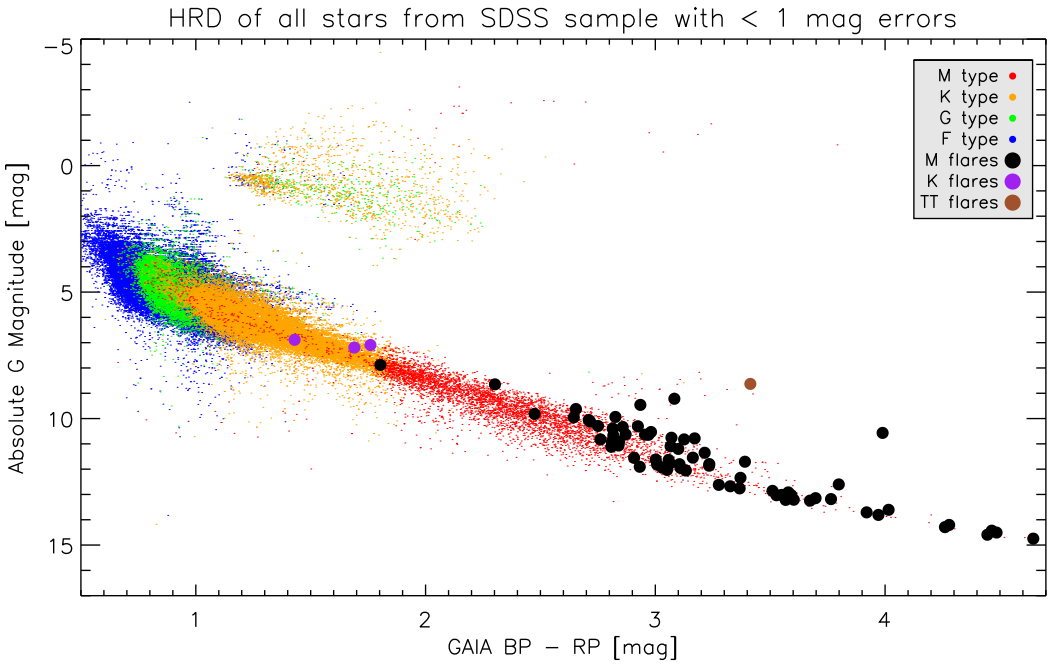

Figure 5.2.: HRD of the SDSS sample with errors < 1 mag in both axes for the original sample. The flaring subsample pose errors of < 2 mag in absolute magnitude and < 1 mag in the color axis. The mayor constraining factor is the availability of error values for the color.

is also displayed. The errors of the distance is color coded as described in the Figure caption. The diameter of the milky way is given as an upper limit for unrealistic distance values. Sorting effects due to getting information out of two datasets (SDSS and GAIA dr2) are prevalent. Most obvious is the lower threshold in magnitude, as GAIA dr2 restricts its measurements on stars brighter than 21 mag in G (Gaia Collaboration et al., 2018).
This plot further indicates that the present displayed sample of flaring M stars consists of M dwarfs only. Stars with missing distances or GAIA values were further evaluated in more detail.

5.1.5. Energy and power calculations

The energy and the power of the flares in $H\alpha$ was calculated. The other chromospheric lines were not considered due to their lower SNR with respect to $H\alpha$.
As the fluxes are given as spectral flux density in units of $10^{-17}\,\mathrm{erg\,s^{-1}cm^{-2}\AA^{-1}}$, one calculates the radiance ($\mathrm{erg\,s^{-1}cm^{-2}}$) by integrating the flux over a certain wavelength range, resulting in a measure for radiating power per area. To get the additional flaring energy, the area of the flaring line and a defined reference spectrum were calculated and subtracted. Prior to the integration, linear interpolation was used to reduce errors arising from offsets in the x axis between the spectra, which could otherwise result in one spectrum having more datapoints to

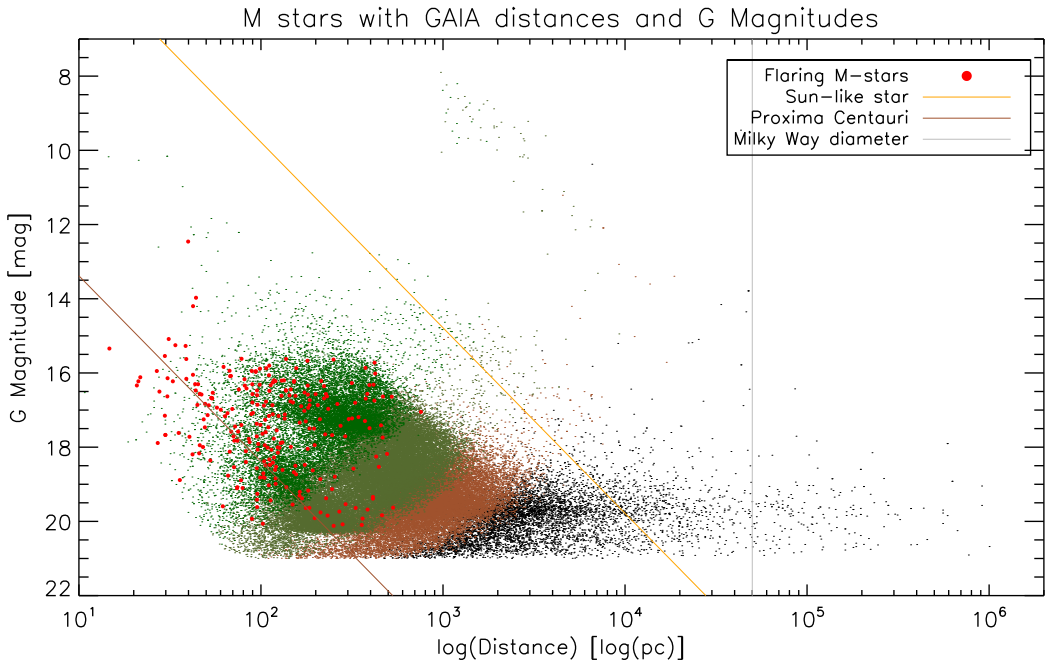

Figure 5.3.: M stars with their respective distances and G magnitudes from GAIA dr2. Flaring M stars are shown within the plot. Example for a dwarf star (Proxima Centauri) and a Sun-like star are given. The diameter of the milky way is given as an upper constraint on the distance. Errors in the distance are color coded. Green: error less than 5%. Olive: error between 5 and 20%. Brown: error between 20 and 50%. Black: error higher than 50%.

be integrated. The used reference spectrum was either decided to be a spectrum declared as a quiet spectrum, the co-added spectrum or the spectrum showing the least amount of activity. Spectra showing cosmic rays in the integration range were excluded.
The radiance of consecutive spectra were added up, while the radiance of the peaking flare alone was also evaluated. To get the radiant energy per area (erg cm^{-2}), the radiances were simply multiplied by the corresponding exposure times.
As these values give information on the radiation emitted by the star measured on earth, the overall flaring energy/power (in units of erg or erg s^{-1}) of the flare is calculated by multiplying the radiant energy per area/radiance with $4\pi d^2$, giving the area of a sphere with d being the distance to the star. This distances are adopted from GAIA DR2 or other sources if no GAIA data was available.
This calculation was done using a wide and a narrow window around $H\alpha$. The reason behind this is that both should yield the same result under optimal conditions, which is unrealistic for the given dataset and SNR. The difference between both values give an idea on the errors due to noisy spectra. Having similar results using both windows further indicate that the found line enhancement is not just an effect of noisy data. The used ranges are $6555 - 6575$ Å for the close range and $6530 - 6600$ Å for the wide range.
A more sophisticated way to determine errors was performed using the errorbars in the used ranges. They were determined as follows:

$$error_{int} = range * \sqrt{\sum_{i}^{N} (error_{(i)})^2} \tag{5.1}$$

Here, N denotes the number of all datapoints in the range (without interpolation) and $error_{(i)}$ the errorbar associated with datapoint i. Obviously, the resulting error becomes bigger with a larger range.
Using maximum error propagation, the end result of the power/energy error was determined by

$$\Delta energy = \left| error_{int\_energy}\, 4\pi d^2 \right| + \left| \Delta d \;\; energy_{per\_area}\, 8\pi d \right| \tag{5.2}$$

$$\Delta power = \left| error_{int\_power}\, 4\pi d^2 \right| + \left| \Delta d \;\; power_{per\_area}\, 8\pi d \right| \tag{5.3}$$

where d is the distance determined by the GAIA DR2 parallax and Δd the associated error determined by the GAIA DR2 parallax error. If no distance error value was available, the second term in equations 5.2 and 5.3 was neglected.

Figure 5.4 shows the result of the $H\alpha$ flaring energy (using the close range) over the distance. Stars that also had quiet reference spectra are marked in blue. The energy values of these flares are more reliable due to the reference being not part

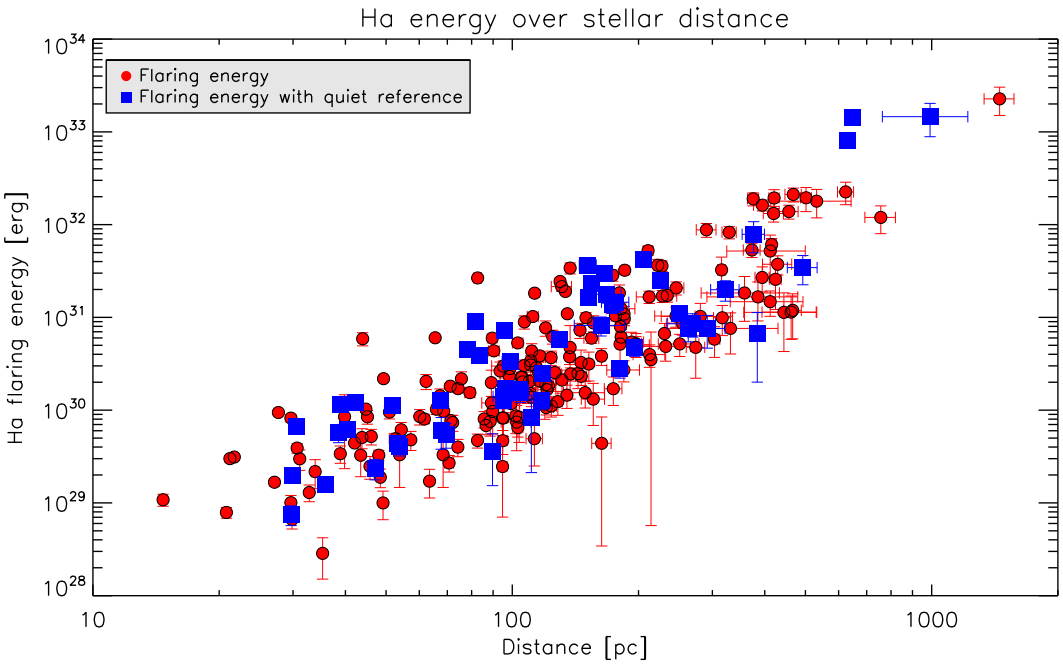

Figure 5.4.: Flare energy (close range) over stellar GAIA distance.

of the flare, which would compromise the calculation. It was not clear whether the reference spectrum was quiet or still in a flaring state for all flares marked in red. The two groups are in clear agreement, indicating that the obtained values marked in red are also fairly reliable.
The flaring energy arising from excess flux in $H\alpha$ ranges from $\sim 3 \times 10^{29}$ erg up to 2×10^{33} erg. The plot shows an expected result: the further away a star is, the more energetic the flare has to be to get detected through the presented methods. This is also another validation of the significance of the found flares.
One has to keep in mind that the distance itself is part of the calculation of the energy, therefore a higher calculated energy at a higher distance is a trivial result. This plot therefore mostly depends on the reliability of the GAIA parallax information. Calculated errorbars (using equation 5.2 for the energy and GAIA parallax errors for the distance) are displayed. The apparent upper limit of energetic flares of nearby stars may be a result of a selection effect and is discussed in chapter 6.

Figure 5.5 shows the result of the $H\alpha$ flaring energy (using the close range) over the GAIA B - R color(difference between optical B band and optical R band). Stars that also had quiet reference spectra are marked in blue.
Albeit having wide error bars in the color axis, the plot shows a clear trend in the flaring spectra, with redder stars seemingly showing less energetic flares than bluer ones. Color excess was not taken into account in this plot, which primarily affects stars with large distances.

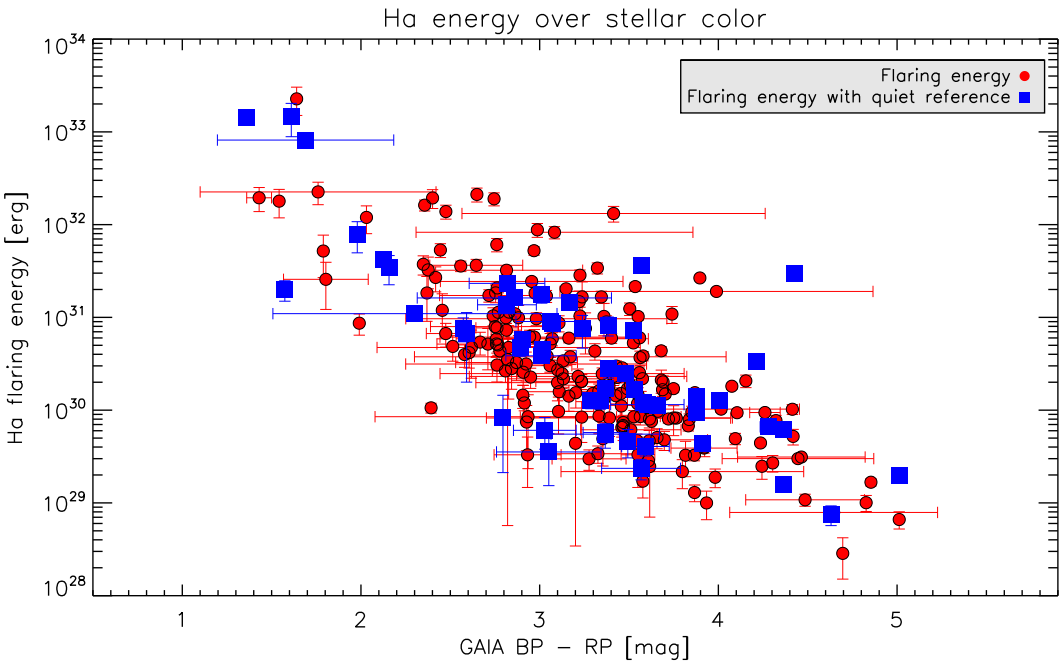

Figure 5.5.: Flare energy (close range) over stellar GAIA B-R color.

Figure 5.6 shows a similar result like the previous plot, giving the same conclusion. It shows the *Hα* flaring energy (using the close range) over the spectral subtype (using information from Skiff, 2014). Color excess effects are of no concern in contrast to the previous figure.
Seemingly, the highest calculated flare energies are observed on K stars and earlier M stars. This is probable due to the K stars showing higher flux, demanding high energy releases to get detected.
Another explanation for this trend is the simple correlation with distance: there are more late M stars in the solar neighbourhood, making their flares (even at small energies) easier to detect, while there are no late M dwarf stars in the dataset with large distances to the solar system. Their flux is not sufficiently large enough for spectroscopic observation in SDSS. K stars on the other hand show higher absolute magnitudes and are easier to observe at larger distances.

Figure 5.7 shows the statistical distribution of the flares per each SNR bin. There appears to be no clear correlation between energy and SNR. The highest outliers are part of the high SNR bin, while the worst SNR bin has the smallest interquantile range (showing the range of 25 and 75 % of the flares).

5.1.6. Special cases in the flaring results

M stars:
As was mentioned before, several stars were identified to be cataclysmic variables showing extreme shifts in the spectra and chromospheric line height variations.

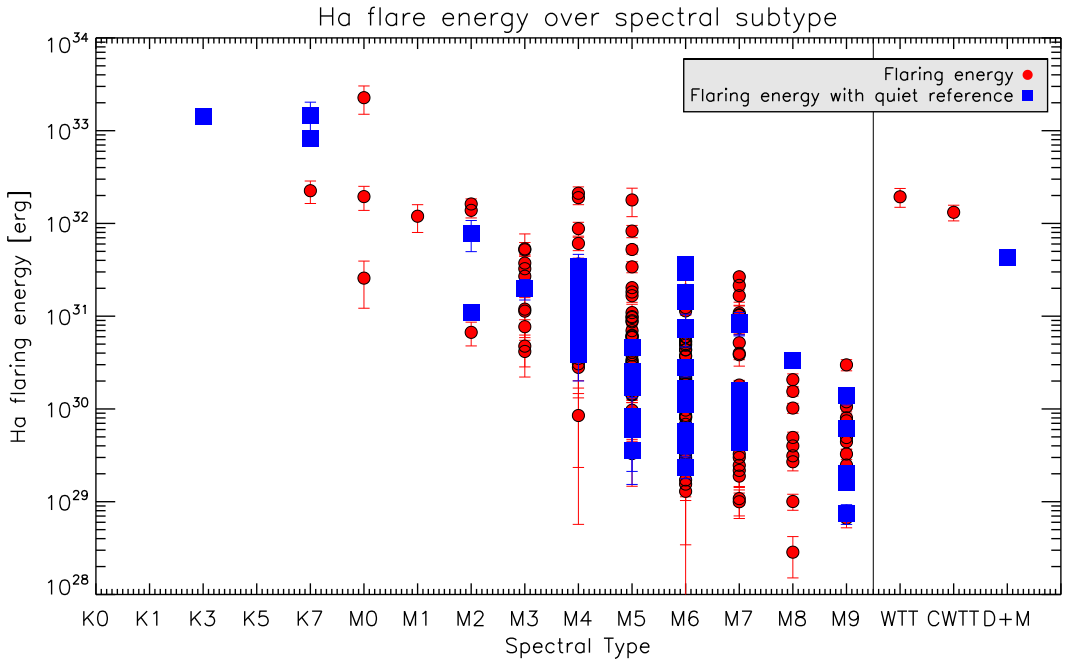

Figure 5.6.: Flare energy (close range) over stellar subtype. T Tauri stars and binaries are displayed separately.

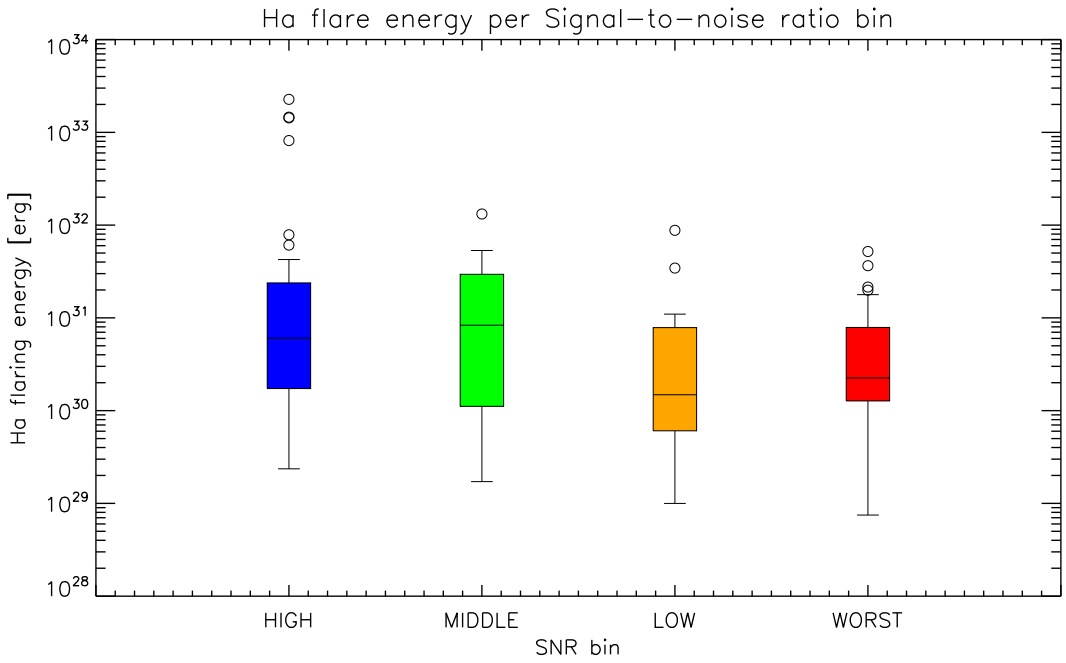

Figure 5.7.: Flare energy (close range) over SNR bin. Box plots are used showing the interquantile (IQR) range (25-75) and the mean value. Maximum whiskers of 1.5 IQR are given, higher energy values indicating outliers are displayed with a circle.

These as well as other, possible close (+eclipsing) White dwarf/late type binaries with extreme line shifts were excluded from the list.
After further inspection, several stars still present in the list are also possible WD+dM binaries. One object ("SDSS J045325.65-054459.2") was found to be most likely a late type M star in front of a more distant star of an earlier type. This gets clear by looking at the available GAIA distances, revealing two sources within two arcseconds. Rebassa-Mansergas et al. (2013) came to the same conclusion, stating the object as a main-sequence-main-sequence superposition.
Other stars given as possible binaries were still included, when there was no sign of significant shift or unusual behaviour of the lines, which would otherwise indicate close binaries. The object "SDSS J005506.77-005702.4" is given as either a detached or (with low confidence) semi-detached star by Becker et al. (2011). With only 3 consecutive spectra, the possible shift due to being a binary system in the data is too low to make concrete assumptions; the object is therefore kept in the list with the flaring attribute "probable".
Object "SDSS J141528.99+123127.4" was found to be in front of a galaxy. Manual inspection revealed that the GAIA DR2 parallax closest to the stellar coordinates obtained by crossmatching gave the value of the galaxy (parallax around 0 mas). The distance was replaced with the star's real distance value. The object "SDSS J161237.41+164556.0" also appears to be in front of another object resulting in two GAIA DR2 distances. Both distances are similar (225 vs 256 parsec, Bailer-Jones et al., 2018).
The spectrum of object "SDSS J162027.54+364002.8" consists of two stars (M4 and M3) too close together to be spectroscopically resolvable, due to the hole diameter in SDSS plates being larger than their angular distance. The distances given by GAIA DR2 are 300 and 350 parsecs, respectively.

K stars:
The star "SDSS J161924.09+061554.2", marked as subtype K3 in SDSS, had a flare that changed its Balmer absorption lines into emission lines. It was identified to be a RS-Canum-venaticorum star (Drake, Graham, et al., 2014).
The star "SDSS J011707.01+250359.8", marked as subtype K3 in SDSS, showing a new emission line in $H\alpha$ and $H\beta$ at one time instance, was identified to be a eclipsing binary of type W UMa (Drake, Graham, et al., 2014).
The star "SDSS J075835.12+482523.6" is marked as a K5 star in SDSS and shows high chromospheric emission lines with variation over time. The spectra show clear shifts in the data, which is an indication of a close binary object. This assumption is confirmed by Kleinman et al. (2013) declaring it a White dwarf/M0e binary, and by Watson, Henden, and Price (2006) that recognised the object as a cataclysmic variable.
The star "SDSS J215455.17+011414.5", marked as subtype K5 in SDSS, shows significantly higher emission lines in $H\alpha$, $H\beta$ and $H\gamma$ and especially high Ca H and K emission lines at two time instances. The spectrum as a whole is red shifted by ~ 2 Å in these instances. Even without the flare, the star showed these lines in

emission. Xue et al. (2014) determined the star to be a K giant star on the RGB, while Kowalski, Hawley, Hilton, et al. (2009) in their search for flaring M dwarfs used the spectral classification dM0. Using data from GAIA, the star appears to be on the upper part of the main sequence, while they also give information on the radius ($2.1972 R_\odot$) and luminosity ($2.153 L_\odot$) (GAIA DR2). This clearly suggests that the star is not a M dwarf star. It may be a K giant, nevertheless, we keep it in the final flaring list.
The star "SDSS J000500.22-043228.8" is marked as a K5 star in SDSS, while an unpublished work of Skiff et al. 2013 gave it the spectral type M0Ve. Heinze et al. (2018) declared the object as a distant binary. The SDSS spectra show a possible flare evolution on both $H\alpha$ and $H\gamma$. The whole spectrum gets shifted over time, which is an indicator for binaries. Flags in the red spectrum range and missing Balmer lines of a higher order resulted in the "Probable" flare categorization of the event.

5.2. CME search results

As was already discussed in section 4.2, the CME search is mostly based on in-depth analysis of the flare results and high emission line search. A list of possible candidates as well as all found asymmetries was created.

5.2.1. CME candidates

10 possible CME candidates were found, all on M stars, that show enhancements in Balmer line wings. One special case detected on a K0 star showing wing absorption in $H\alpha$ is discussed in section 5.2.4.
An overview of the possible candidates is given in Table 5.4, including general information on the objects. Table 5.5 shows calculated values based on the CME assumptions.

Nr. 1: Star SDSS J052700.12+010136.8 (Figure 5.9a):
The star with subtype M3.2 (SDSS classification M4) was found by the high emission line algorithm. Other sources report it as a WTTS (McGehee, 2006). The SDSS spectrum shows 5 consecutive spectra with exposure time of 15 minutes for spectrum 1 and 5 and 25 minutes for spectra 2,3 and 4. Spectrum number 4 shows a significant increase in flux on two successive datapoints on the right wing in $H\alpha$ and one datapoint on each $H\beta$ and $H\gamma$. One has to keep in mind that the wavelength axis is oversampled in respect to the spectral resolution, making single enhanced datapoints hard to interpret. Still, it is noted that these enhancements are significantly higher in all three lines and occur at a similar Doppler shifted velocity range. The star exhibits a high SNR compared to other SDSS spectra. It

Nr.	SDSS ID	RA	DEC	Type	Found by	SNR Bin
1	J052700.12+010136.8	81.75054	1.02691	M3.2[1]	Emission line	high
2	J085556.66+174942.0	133.98612	17.82835	M4e[2]	Gauss peak difference	high
3	J110743.30+075624.9	166.93047	7.94027	M4e[2]	Emission line	high
4	J042139.64+264913.8	65.41520	26.82050	M6[3]	Gauss peak difference	middle
5	J082857.42+470654.4	127.23924	47.11513	M5e[2]	Emission line	middle
6	J000206.48+011536.6	0.52572	1.26006	M9e[2]	Gauss peak difference	low
7	J144759.59-014914.6	221.99831	-1.82074	M7e[2]	Gauss peak difference	low
8	J052856.54-000032.4	82.23562	-0.00900	M4e[2]	Ha peak difference	high
9	J053709.91-011050.3	84.29134	-1.18067	WTT[4]	Gauss peak difference	high
10	J052839.66-000322.5	82.16528	-0.05627	M4e[2]	Gauss peak difference	high

Table 5.4.: List of the CME candidates including their SDSS ID, their right ascension and declination, their spectral subtype, the algorithm that found them and their SNR bin. Spectral type sources: [1] Suárez et al. (2017),[2]West, Morgan, et al. (2011),[3]Luhman et al. (2017),[4]Koenig et al. (2015)

Nr.	Enhanced Wing	Distance [pc]	Max. velocity [km/s]	Est.mass $H\alpha$ [g]	Error %	Est.mass $H\gamma$ [g]	Error %
1	red	379.3	594	3.9E+17	81	9.0E+17	42
2	red	234.2	708	8.4E+17	22	3.1E+17	71
3	red	70.5	667	7.9E+16	51	1.7E+17	24
4	red	166.3	703	1.1E+18	11	1.7E+17	50
5	red	89.3	352	8.5E+15	120	6.6E+16	43
6	blue	20.8	-434	1.6E+15	44	4.8E+15	37
7	blue	47.3 *	-343	2.9E+15	68	1.5E+16	42
8	blue	374.1	-343	4.9E+17	67	6.6E+17	53
9	red	-	708	-	-	-	-
10	blue	467.8	-365	7.9E+18	19	3.1E+18	38

Table 5.5.: CME candidates with associated values, indicating the direction of the Doppler shift, the distance in parsec based on Gaia DR2, their maximum velocity and the estimated mass (including rough error estimates in percent) using the flux power in $H\alpha$. *Distance adopted from West, Morgan, et al. (2011)

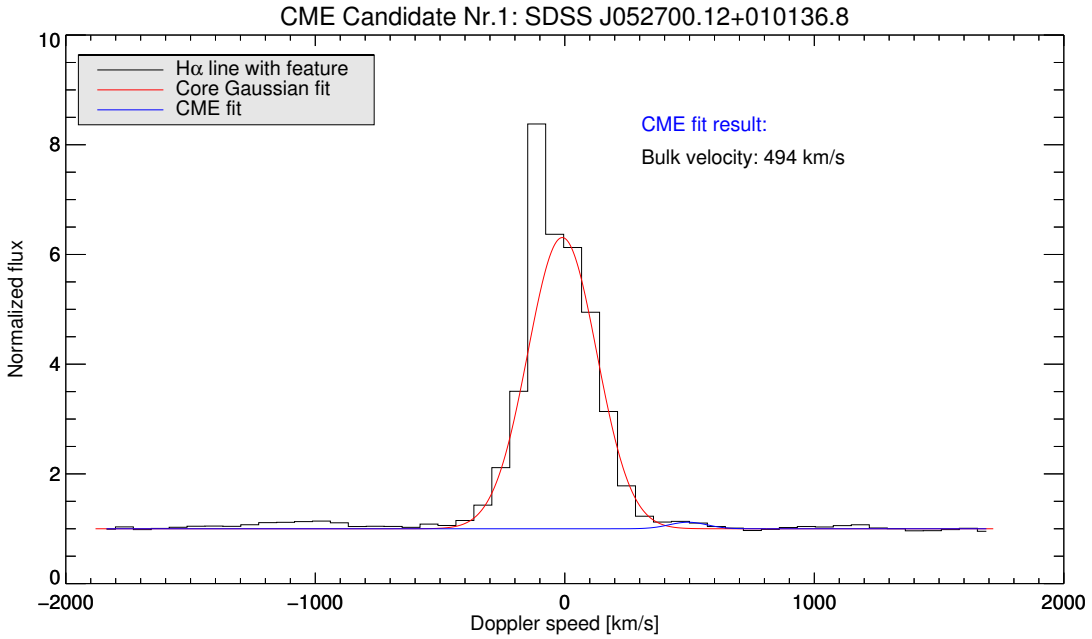

Figure 5.8.: *Hα* line of star number 1. Core as well as the possible CME feature is fitted, with the bulk velocity of the Gaussian CME fit stated.

shows strong chromospheric emission lines that peak at approximately 6 times the flux of the surrounding continuum. The maximum Doppler velocity (manually read out from the spectrum) amounts to approximately 600 km/s, 630 km/s and 640 km/s for $H\alpha$, $H\beta$ and $H\gamma$ respectively. A bulk velocity of $\sim$ 500 km/s was derived using a Gaussian fit in the CME signature in $H\alpha$ (see Figure 5.8).
The mass estimated from integrated flux measurements in both $H\alpha$ and $H\gamma$ using equation 5.4 amounts to approximately 4×10^{17} g and 9×10^{17} g, respectively. These values are just an order of magnitude estimation and should be treated carefully as the method using linear interpolation to make the integration over the enhanced ranges possible is not reliable.
While the quality of the plate is categorized as "bad" by SDSS, there are no datapoint flags in the wings of the emission lines to indicate problematic data (only the $H\alpha$ line core is flagged in several spectra).

Nr.2: Star SDSS J085556.66+174942.0 (Figure 5.9b):
The star with subtype M4e (SDSS classification M4) was found by the Gauss peak difference algorithm while searching for flares. The found flare is part of the M star flare in the high SNR bin. The spectrum consists of 2 x 2 consecutive spectra. The latter two spectra (which are observed 2 days after the first set) show higher Balmer emission lines interpreted as flaring activity. Spectrum number 3 shows a clearly enhanced wide red wing in $H\alpha$ over 7 successive datapoints, while two datapoints are enhanced in each $H\beta$ and $H\gamma$. Only the feature in $H\alpha$ is significantly enhanced considering all errorbars. The noise in other chromospheric lines is too high to detect wing enhancements, while the flare is still visible.
The maximum Doppler velocity (manually read out from the spectrum) amounts

to approximately 710 km/s, 300 km/s and 310 km/s for $H\alpha$, $H\beta$ and $H\gamma$ respectively. A bulk velocity of $\sim$ 300 km/s is estimated, while the Gaussian fit into the CME signature in $H\alpha$ (see 5.10) did not fit perfectly with the enhancement being wide and the normalized flux of the flaring spectrum leading to a diminished enhancement. The mass estimated from integrated flux measurement in both $H\alpha$ and $H\gamma$ using equation 5.4 amounts to approximately 8.4×10^{17} g and 3×10^{17} g, respectively. Linearly interpolating datapoints in the $H\alpha$ wing is more sensible with this object, while the integration over the interpolated $H\gamma$ enhancement based on two enhanced points is used with caution.
The plate quality is categorized as "good" by SDSS and 4 datapoint flags are present in the flaring line, which is not unusual for flaring activity.

Nr. 3: Star SDSS J110743.30+075624.9 (Figure 5.11a):
The star with subtype M4e (SDSS classification M4) was found by the high emission line algorithm. The spectrum consists of 2 x 2 consecutive spectra, with the latter two being observed 4 days after the first two. The exposure times amounted to 20 minutes for the first two and 12 and 10 minutes for the latter two. Spectrum number 4 shows both an enhanced wide red wing in $H\alpha$ (between 5 and 7 successive datapoints) and an enhanced blue wing (2 successive datapoints). The focus was laid on its red wing, as the red $H\beta$ wing shows two enhanced datapoints and the red $H\gamma$ wing shows 6. While not being significant considering the errorbars, this red wing enhancement can also be seen in $H\delta$, the overlapping $He/Ca\ II\ H$ line and the $H\zeta$ line (but not visible in CA II K). Flaring activity is not visible within this resolution.
The maximum Doppler velocity (manually read out from the spectrum) amounts to approximately 670 km/s, 300 km/s and 650 km/s for $H\alpha$, $H\beta$ and $H\gamma$ respectively. A bulk velocity of $\sim$ 300 km/s is estimated. Fitting a Gaussian fit into the CME signature in $H\alpha$ did not work on normalized flux of the spectrum with enhanced flux alone, as the emission still lies lower than the normalized value. The mass estimated from integrated flux measurement in both $H\alpha$ and $H\gamma$ using equation 5.4 amounts to approximately 8×10^{16} g and 1.7×10^{17} g, respectively. Integrating over datapoints is possible in this case due to several successive datapoints in both $H\alpha$ and $H\gamma$ (still, linear interpolation was used).
The plate quality is categorized as "marginal" by SDSS. There are no datapoint flags of importance for this analysis, indicating no problem with the data.

Nr. 4: Star SDSS J042139.64+264913.8 (Figure 5.11b):
The star with subtype M6 (SDSS classification M8) was found by the Gauss peak difference algorithm while searching for flares. The found flare is part of the M star flare in the middle SNR bin. The spectrum consists of 5 single spectra observed within 4 hours. While the first 3 spectra show quiet Balmer emission lines (down to $H\gamma$), the 4th spectrum showed flaring activity with an enhanced peak and a wide red wing which is visible in the Balmer lines down to $H\delta$. The 5th and last spectrum is observed one hour after the previous one, only showing an enhanced emission line core (which is higher in $H\alpha$, of similar height in $H\beta$

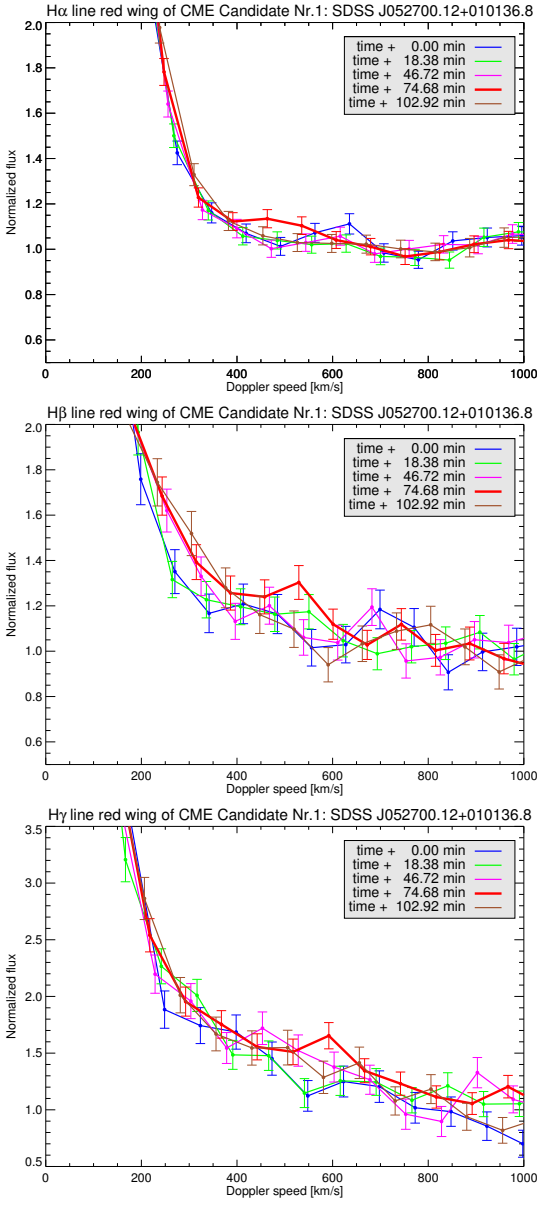

(a) *Hα* red wing of star number 1. The line showing the enhancement is marked in red.

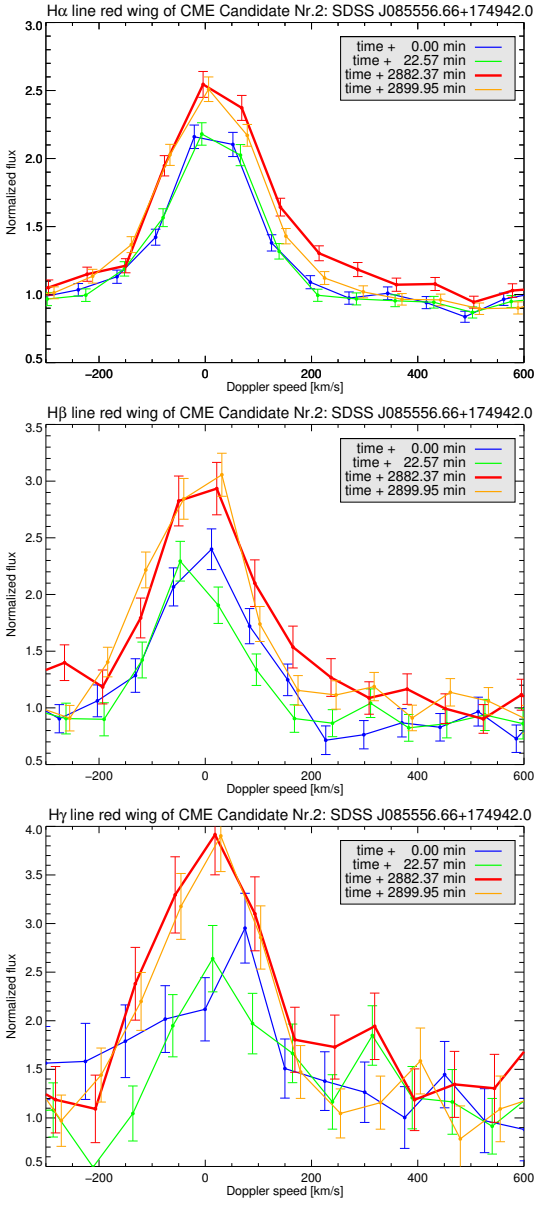

(b) *Hα* red wing of star number 2. The line showing the enhancement is marked in red.

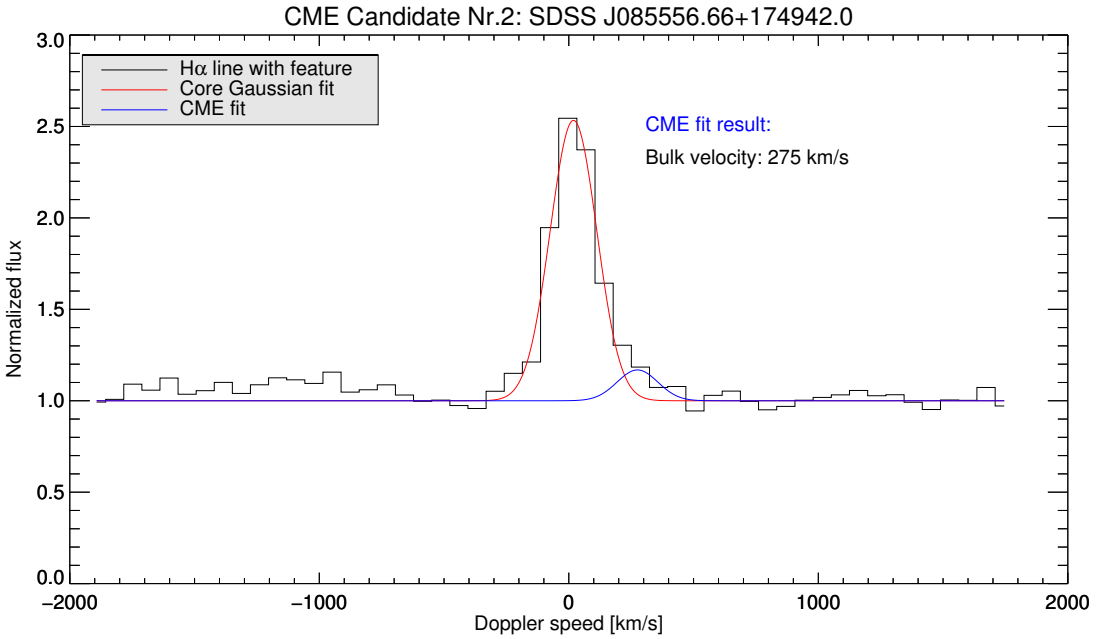

Figure 5.10.: *Hα* line of star number 2. Core as well as the possible CME feature is fitted, with the bulk velocity of the Gaussian CME fit stated.

and somewhat lower than the previous one in $H\gamma$, while not being visible in $H\delta$ at all). The red wing enhancement is showing 7 significantly successive higher datapoints in $H\alpha$, 8 higher datapoints in $H\beta$ (several of which are above the errorbars) and two higher points in $H\gamma$ (with too high errorbars).
The maximum Doppler velocity (manually read out from the spectrum) amounts to approximately 700 km/s, 700 km/s and 240 km/s for $H\alpha$, $H\beta$ and $H\gamma$ respectively. A bulk velocity of $\sim$ 360 km/s was derived using a Gaussian fit in the CME signature in $H\alpha$ (see 5.12).
The mass estimated from integrated flux measurements in both $H\alpha$ and $H\gamma$ using equation 5.4 amounts to approximately 1.1×10^{18} g and 1.7×10^{17} g, respectively. While the enhanced feature in $H\alpha$ is sufficiently broad to be safely integrated, the feature appears weak in $H\gamma$, making the mass assumptions unreliable.
The plate quality is categorized as "bad" by SDSS. The flaring lines are mostly flagged in both $H\alpha$ and $H\beta$ as well as the whole emission feature in the $H\alpha$ red wing. As these values depart heavily from the quiet spectra, the flagging of these values is not unexpected.

Nr. 5: Star SDSS J082857.42+470654.4 (Figure 5.13a):
The star with subtype M5e (SDSS classification M8) was found by the high emission line algorithm. The spectrum consists of 4 consecutive single spectra with an exposure time of 15 minutes each. The last spectrum shows one higher datapoint (but not above all errorbars) in the red wing of $H\alpha$, but shows both wings enhanced in $H\beta$ with 3 to 4 higher datapoints (one significantly higher) . The enhancement of the red wing is still visible in the $h\gamma$ line, albeit being not significantly above the errorbars. Although the emission line is barely visible

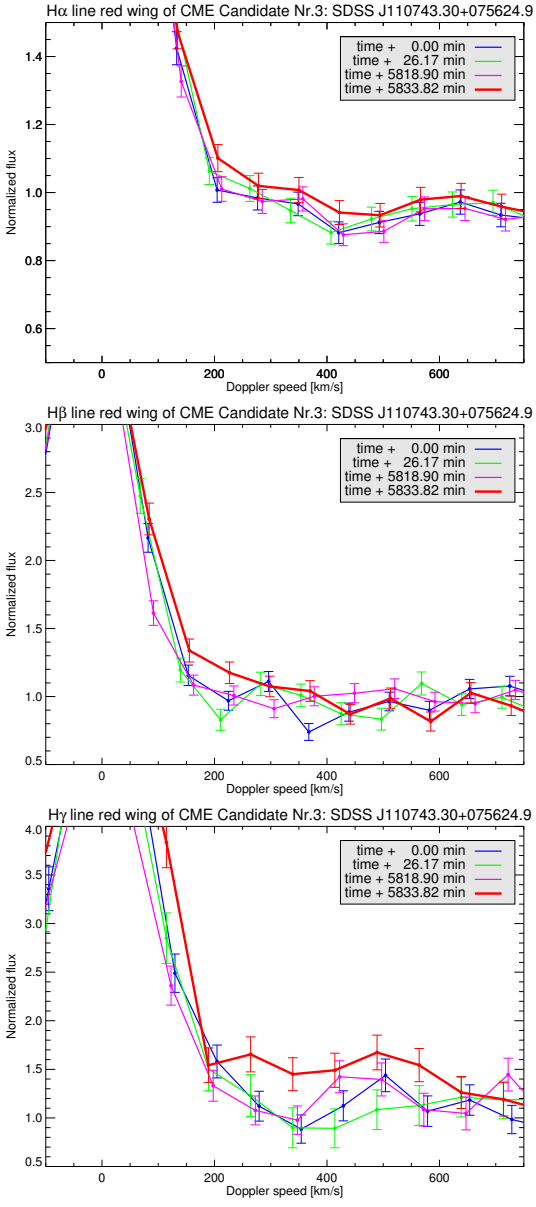

(a) *Hα* red wing of star number 3. The line showing the enhancement is marked in red.

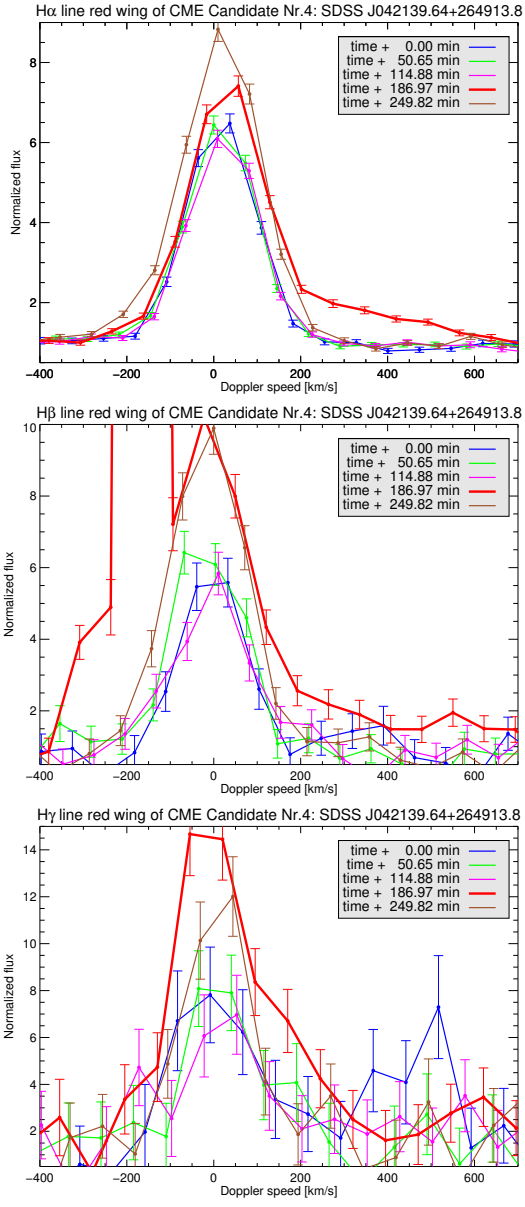

(b) *Hα* red wing of star number 4. The line showing the enhancement is marked in red.

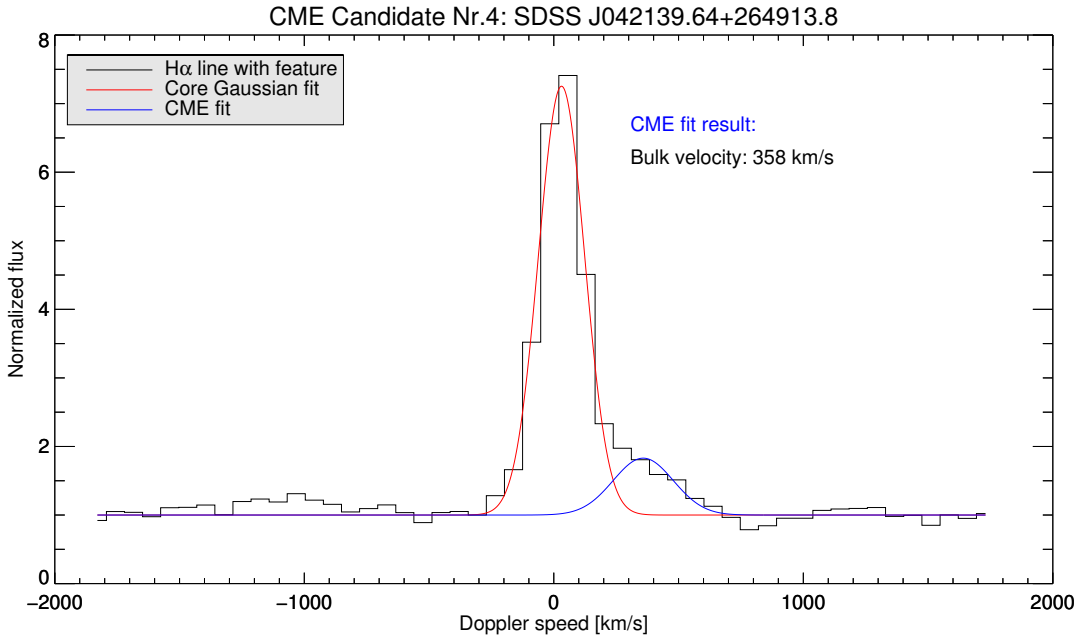

Figure 5.12.: $H\alpha$ line of star number 4. Core as well as the possible CME feature is fitted, with the bulk velocity of the Gaussian CME fit stated.

in $H\gamma$, one point in the red wing is enhanced even above the errorbars (which could be an anomaly as well). All that considered, it appears as if this spectrum shows activity in the red wing, while the emission line peak change is too small to report a flare. Assuming a CME feature, the maximum Doppler velocity (manually read out from the spectrum) amounts to approximately 350 km/s, 390 km/s and 300 km/s for $H\alpha$, $H\beta$ and $H\gamma$ respectively. A bulk velocity of $\sim$ 275 km/s was estimated. Fitting a Gaussian into the CME signature in $H\alpha$ with only one enhanced datapoint did not yield acceptable results.
For the sake of completeness, the mass estimated from integrated flux measurements was still conducted, although the amount of significantly enhanced datapoints is low in the lines of $H\alpha$ and $H\gamma$. The estimated masses using equation 5.4 led to values of 8.5×10^{15} g in $H\alpha$ and 6.6×10^{16} g in $H\gamma$.
The plate quality is categorized as "good" by SDSS. There are no datapoint flags of importance for the analysed spectral ranges.

Nr. 6: Star SDSS J000206.48+011536.6 (Figure 5.13b):
The star with subtype M9e (SDSS classification M8) was found by the Gauss peak difference algorithm while searching for flares. The found flare is part of the M star flare in the low SNR bin. The spectrum consists of 4 consecutive single spectra with exposure times between 10 and 15 minutes each. It shows a flare, peaking in the second spectrum. Afterwards, the emission lines drop in spectrum 3 and get significantly higher again in the last spectrum, although not as high as in the first spectrum. The first spectrum shows excess flux in the blue wing of $H\alpha$ and $H\beta$. The higher flux in the blue wing of $H\gamma$ lies well within the errorbars and therefore within the noise of the surrounding continuum. While

only one datapoint in $H\beta$ is significantly higher than the errorbars, the whole blue wing of $H\alpha$ is consistently higher than the other spectra within 4 successive datapoints. All that considered, it is the weakest of the present candidates where the assumption of a CME can be applied.
The maximum Doppler velocity (manually read out from the spectrum) amounts to approximately $-430\,\mathrm{km/s}$, $-440\,\mathrm{km/s}$ and $-280\,\mathrm{km/s}$ for $H\alpha$, $H\beta$ and $H\gamma$ respectively. The minus is indicating velocity towards the line-of-sight. A bulk velocity of $\sim 290\,\mathrm{km/s}$ was derived using a Gaussian fit for the CME signature in $H\alpha$ (see 5.14).
Similar to candidate number 5, the mass estimation was performed for the sake of completeness, with values from the $H\gamma$ line being noted as unreliable. The measurement in both $H\alpha$ and $H\gamma$ using equation 5.4 amounts to approximately $1.6 \times 10^{15}\,\mathrm{g}$ and $4.8 \times 10^{15}\,\mathrm{g}$, respectively.
The plate quality is categorized as "good" by SDSS. Some of the datapoints in the line core are flagged due to high difference arising from the flare.

Nr. 7: Star SDSS J144759.59-014914.6 (Figure 5.16a):
The star with subtype M7e (SDSS classification M6) was found by the Gauss peak difference algorithm while searching for flares. The found flare was excluded from the M star flare list due to datapoint flags in $H\alpha$, high noise even in $H\beta$ and $H\delta$ showing no change at all. This lead to the categorization of a "mini" flare, which are excluded in the final list.
The spectrum consists of 3 consecutive single spectra with exposure times being 15 minutes for spectrum 1 and 20 minutes for spectra 2 and 3. It shows a higher activity in $H\alpha$ in the last spectrum. The same spectrum shows excess flux in the blue wing of $H\alpha$ and a clear blue asymmetry of the $H\beta$ line. The blue wing $H\alpha$ enhancement consists of two datapoints, one being significantly above the errorbars, while the enhancement in $H\beta$ shows 4 higher datapoints with two being significantly higher.
The maximum Doppler velocity (manually read out from the spectrum) amounts to approximately $-340\,\mathrm{km/s}$, $-320\,\mathrm{km/s}$ and $-340\,\mathrm{km/s}$ for $H\alpha$, $H\beta$ and $H\gamma$ respectively. A bulk velocity of $\sim 290\,\mathrm{km/s}$ was derived using a Gaussian fit in the CME signature in $H\alpha$ (see 5.15).
Similar to the two aforementioned candidates, the mass estimation has to be used with caution, with values from the $H\gamma$ line being noted as unreliable. The measurement in both $H\alpha$ and $H\gamma$ using equation 5.4 amounts to approximately $2.9 \times 10^{15}\,\mathrm{g}$ and $1.5 \times 10^{16}\,\mathrm{g}$, respectively.
The plate quality is categorized as "good" by SDSS. The whole red spectrum is flagged in all spectra with the flag "MANYBADCOLUMNS", resulting in extra caution using this spectrum. No flags in the blue spectrum are of concern for this analysis.

Nr. 8: Star SDSS J052856.54-000032.4 (Figure 5.16b):
The star with subtype M4e (SDSS classification M4) was found by an older version of the Gauss peak difference algorithm, only looking at $H\alpha$ changes.

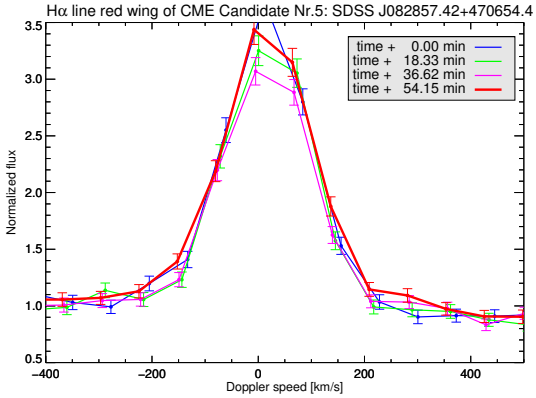

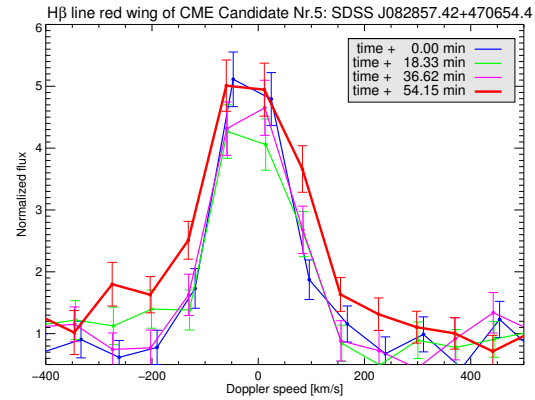

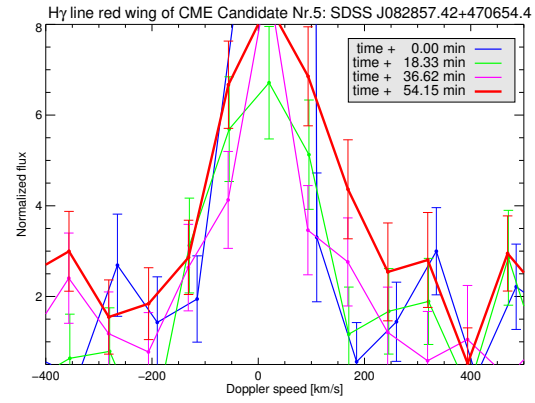

(a) *Hα* red wing of star number 5. The line showing the enhancement is marked in red.

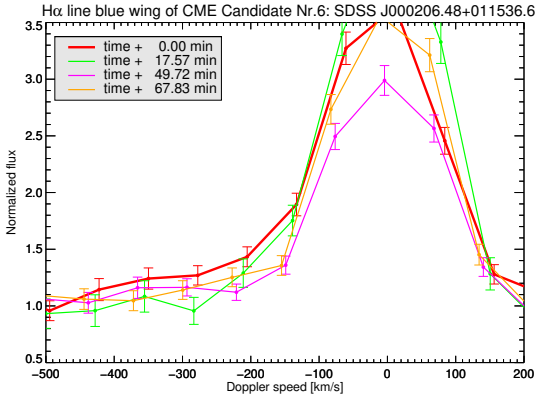

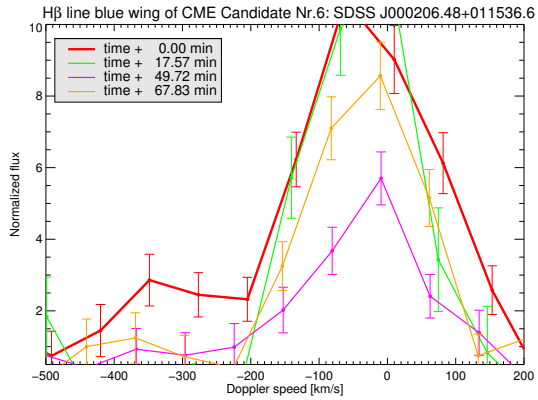

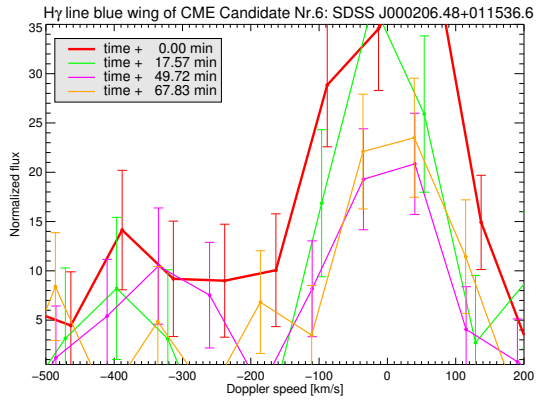

(b) *Hα* red wing of star number 6. The line showing the enhancement is marked in red.

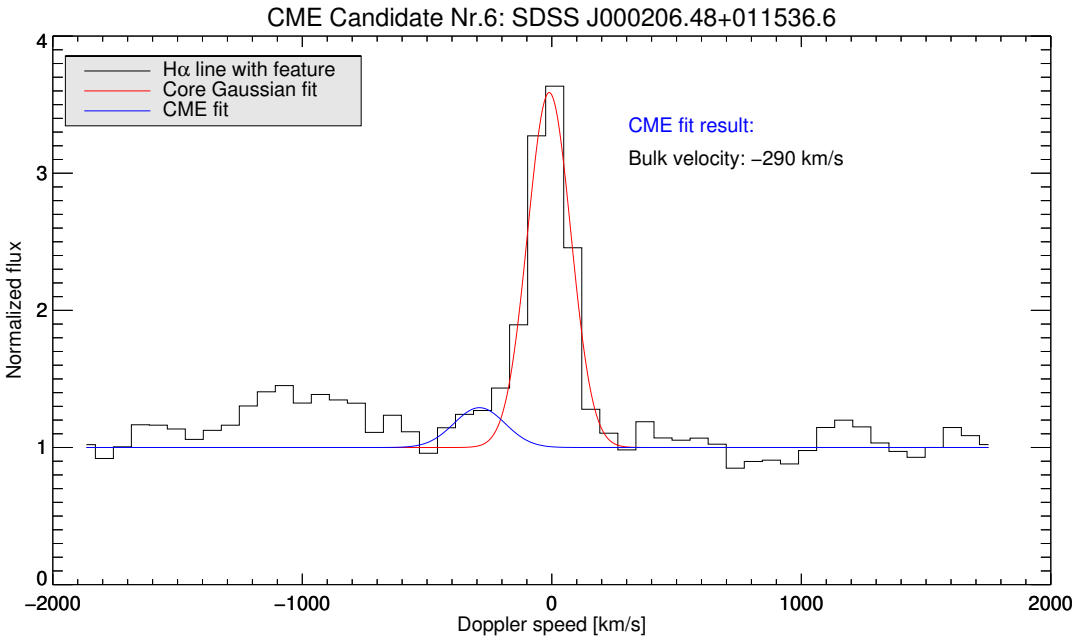

Figure 5.14.: *Hα* line of star number 6. Core as well as the possible CME feature is fitted, with the bulk velocity of the Gaussian CME fit stated.

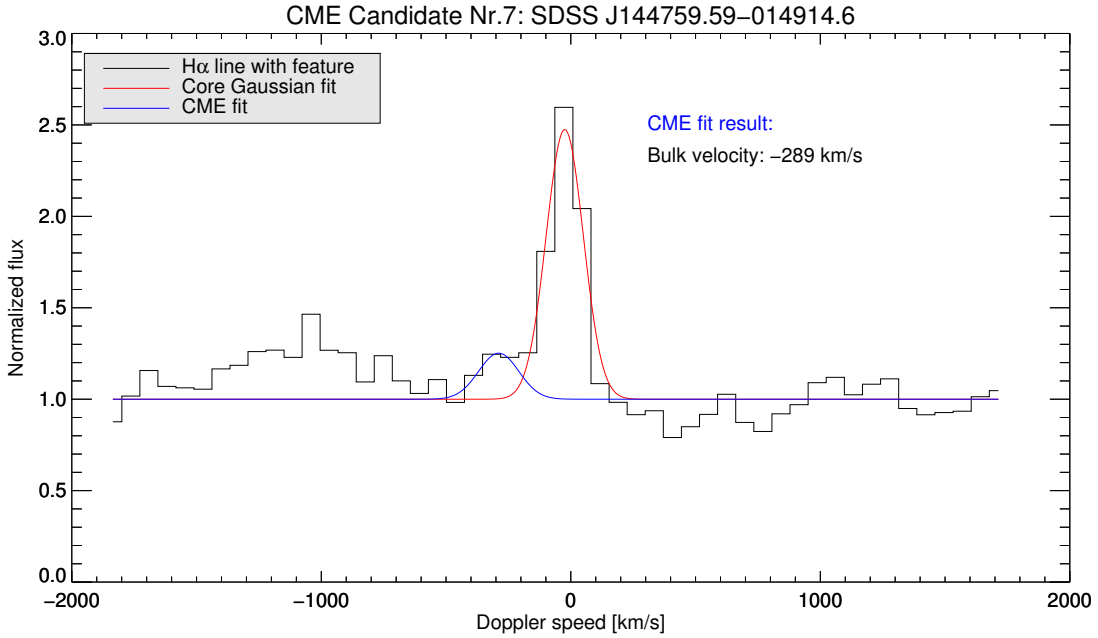

Figure 5.15.: *Hα* line of star number 7. Core as well as the possible CME feature is fitted, with the bulk velocity of the Gaussian CME fit stated.

Found variations in the height of the emission lines were deemed not high enough for a clear detection of a flare. The spectrum consists of 5 consecutive single spectra, with exposure times being 15 minutes for spectrum 1 and 5 and 25 minutes for spectra 2, 3 and 4. The last spectrum shows excess flux in the blue wing of $H\alpha$ (3 datapoints, not above errorbars) and a blue wing enhancement of the $H\beta$ line (3 datapoints, one above the errorbars). The blue wing of $H\gamma$ shows two higher datapoints (not above errorbars).
The maximum Doppler velocity (manually read out from the spectrum) amounts to approximately $-340\,\mathrm{km/s}$, $-380\,\mathrm{km/s}$ and $-290\,\mathrm{km/s}$ for $H\alpha$, $H\beta$ and $H\gamma$ respectively. A bulk velocity of $\sim 200\,\mathrm{km/s}$ is estimated.
Similar to the two aforementioned candidates, the mass estimation has to be used with caution. The measurement in both $H\alpha$ and $H\gamma$ using equation 5.4 amounts to approximately 5×10^{17} g and 6.6×10^{17} g, respectively.
The plate quality is categorized as "bad" by SDSS. The $H\alpha$ line is flagged in every spectrum with the flag "BADSKYCHI". The blue wing enhancements are not flagged in any of the Balmer lines.

Nr. 9: Star SDSS J053709.91-011050.3 (Figure 5.18a):
The star reported as weak line TTauri star (SDSS classification M5) was found by the Gauss peak difference algorithm while searching for flares. The found flare is part of the M star flare in the high SNR bin. The spectrum consists of 5 single spectra, the first exhibiting an exposure time of 15 minutes, while the other 4 spectra build a consecutive time series 1 day after the first spectrum, also with 15 minutes of exposure time each. The last spectrum shows a big flare in the chromospheric lines, which includes a wide flux enhancement in the red wing. The flare and flux excess is visible in all available Balmer lines down to $H\zeta$. The wing enhancement is significantly higher than the quiet spectrum in at least 6 successive datapoints in $H\alpha$, $H\beta$ and $H\gamma$.
The maximum Doppler velocity (manually read out from the spectrum) amounts to approximately $710\,\mathrm{km/s}$, $-760\,\mathrm{km/s}$ and $590\,\mathrm{km/s}$ for $H\alpha$, $H\beta$ and $H\gamma$ respectively. A bulk velocity of $\sim 340\,\mathrm{km/s}$ was derived using a Gaussian fit in the CME signature in $H\alpha$ (see 5.17).
There is no mass estimation because there was no available value for the distance of the star.
The plate quality is categorized as "bad" by SDSS. Most of the $H\alpha$ emission line is flagged in all spectra and the red wing excess is also flagged, which is expected due to the high difference of these values from the quiet spectrum.

Nr. 10: Star SDSS J052839.66-000322.5 (Figure 5.18b):
The star reported as a M4e type (SDSS classification M4) was found by the Gauss peak difference algorithm while searching for flares. The found flare is part of the M star flare in the high SNR bin. The spectrum consists of 5 consecutive single spectra, with exposure times being 15 minutes for spectrum 1 and 5 and 25 minutes for spectra 2, 3 and 4. The spectra show a decaying flare, having its maximum in the first spectrum. The first three spectra also show an enhanced blue

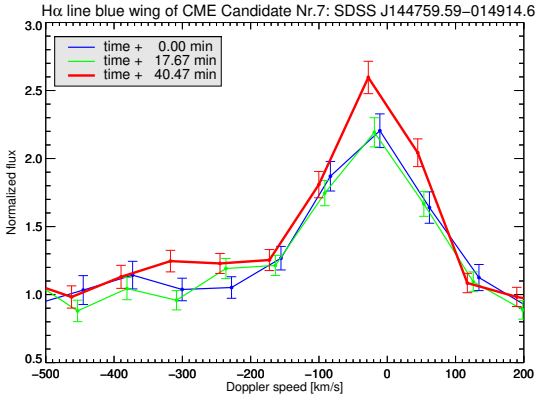

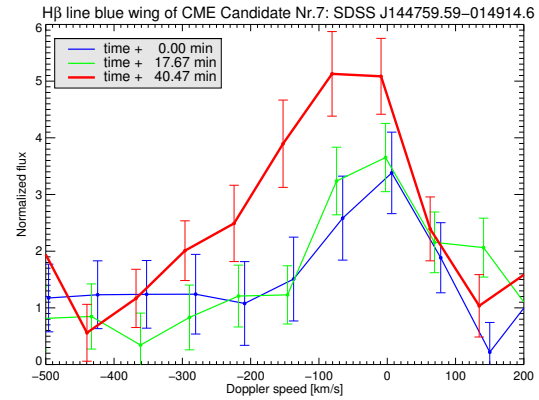

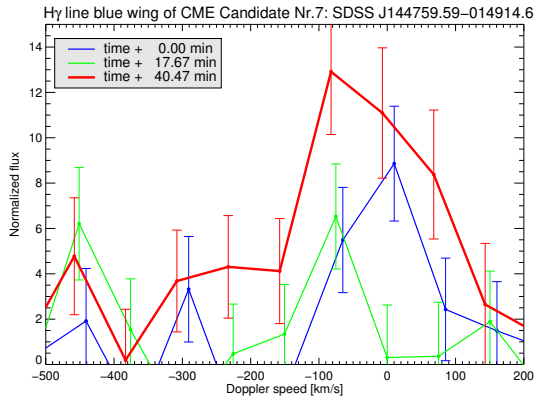

(a) *Hα* red wing of star number 7. The line showing the enhancement is marked in red.

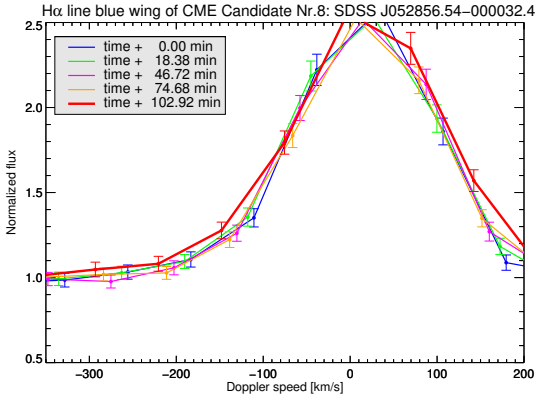

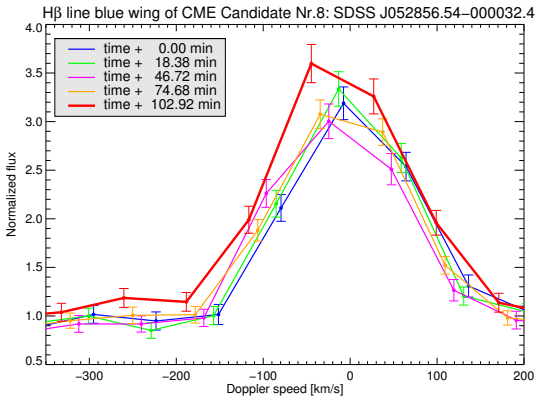

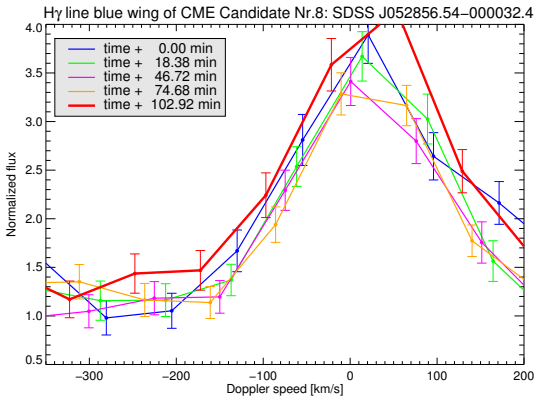

(b) *Hα* red wing of star number 8. The line showing the enhancement is marked in red.

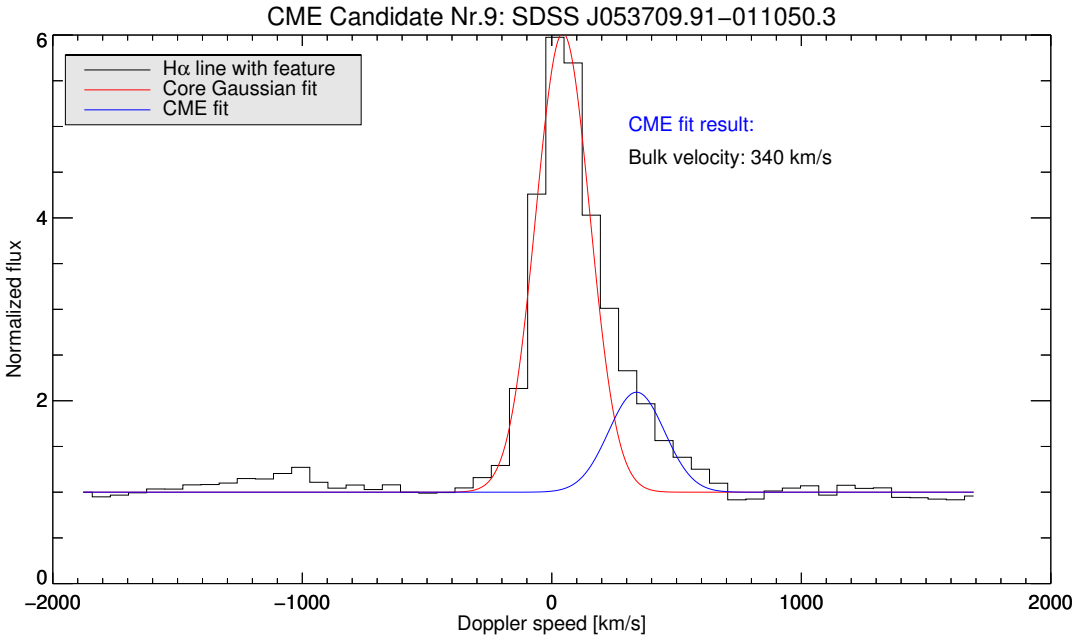

Figure 5.17.: *Hα* line of star number 9. Core as well as the possible CME feature is fitted, with the bulk velocity of the Gaussian CME fit stated.

wing in $H\alpha$, which also decays over time. The whole blue wing (4 datapoints) of the first two spectra in $H\alpha$ is significantly enhanced compared to the last spectrum that shows the least amount of activity. The blue wing is also enhanced in $H\beta$, but only two datapoints in the blue wing in spectrum one and two are significantly higher. While there is still an enhancement visible in $H\gamma$, no datapoint is significantly above the errorbars.
The maximum Doppler velocity (manually read out from the spectrum) amounts to approximately $-365\,\mathrm{km/s}$, $-320\,\mathrm{km/s}$ and $-450:\mathrm{km/s}$ for $H\alpha$, $H\beta$ and $H\gamma$ respectively. A bulk velocity of $\sim -240\,\mathrm{km/s}$ was derived using a Gaussian fit in the CME signature in $H\alpha$ (see 5.19).
The mass estimated from integrated flux measurements in both $H\alpha$ and $H\gamma$ using equation 5.4 amounts to approximately 7.9×10^{18} g and 3.1×10^{18} g, respectively. While the enhanced feature in $H\alpha$ is sufficiently broad to be safely integrated, the feature appears weak in $H\gamma$, making the mass assumptions unreliable.
The plate quality is categorized as "bad" by SDSS. The $H\alpha$ line is flagged in every spectrum with the flag "BADSKYCHI". The blue wing enhancements in the first three spectra are flagged with the flag "COMBINEREJ", which is a common flag for unusual enhancements. It states that these points are rejected for the coadded spectrum.

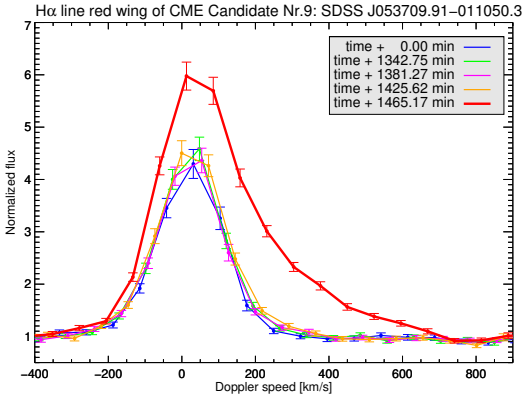

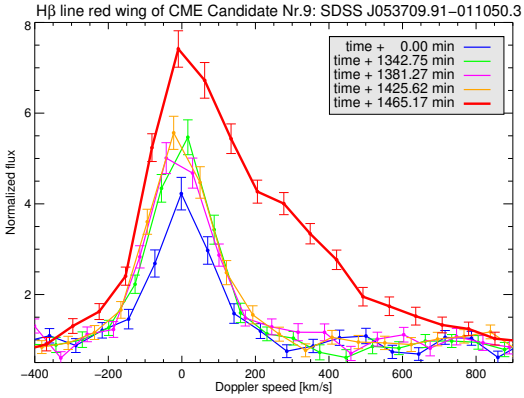

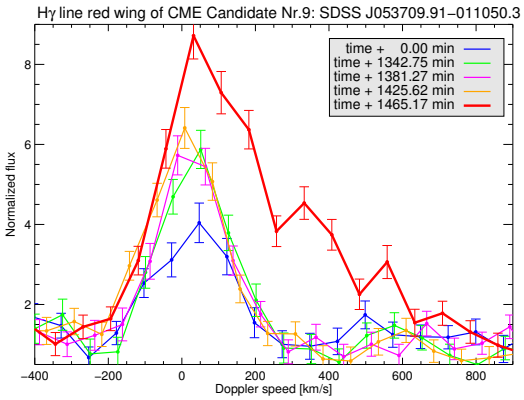

(a) *Hα* red wing of star number 9. The line showing the enhancement is marked in red.

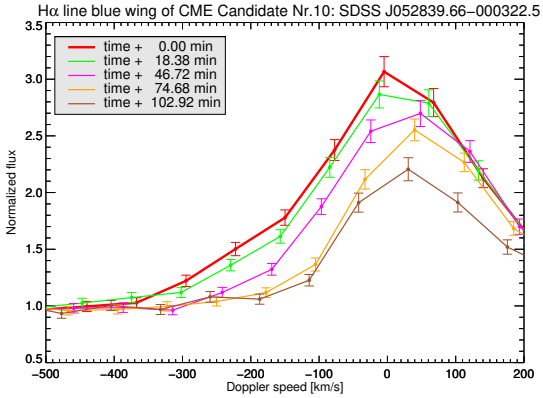

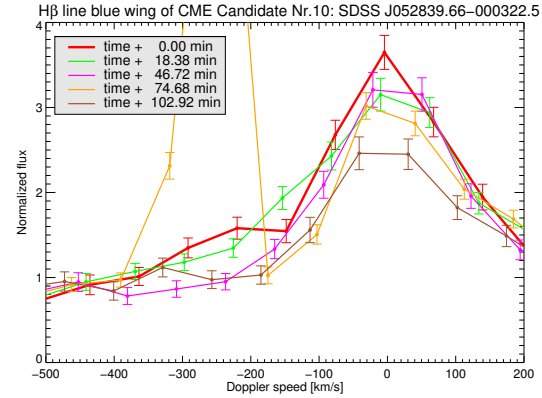

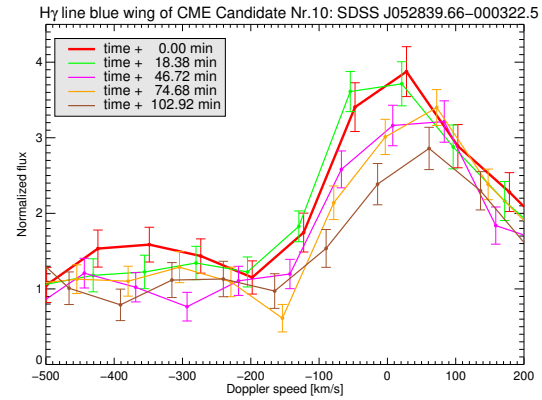

(b) *Hα* red wing of star number 10. The line showing the enhancement is marked in red.

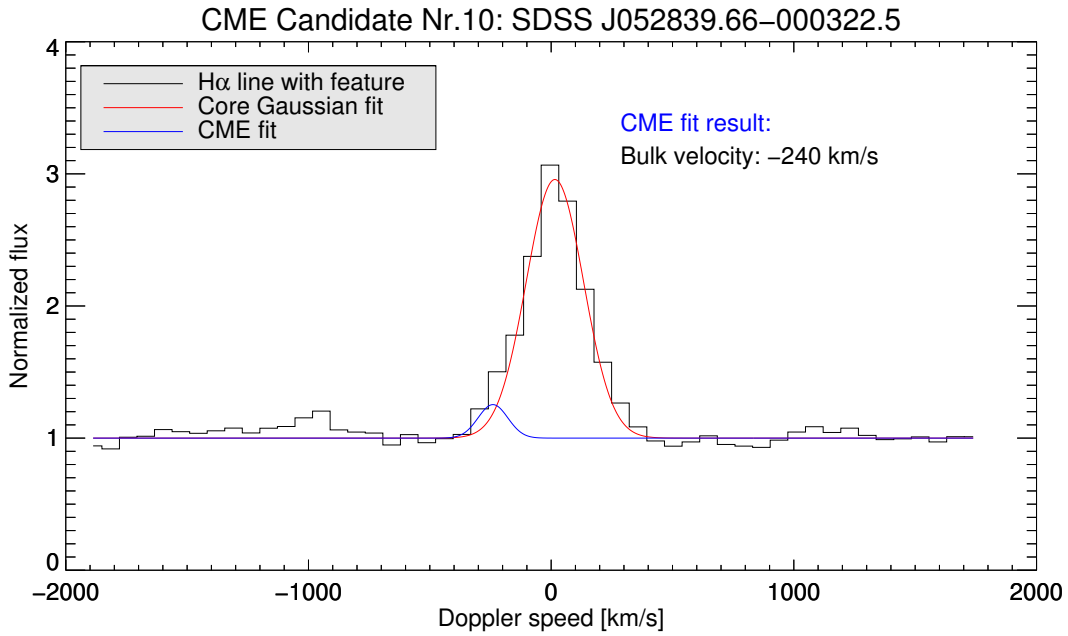

Figure 5.19.: *Hα* line of star number 10. Core as well as the possible CME feature is fitted, with the bulk velocity of the Gaussian CME fit stated.

5.2.2. Mass and velocity estimations

Under the assumption of the features showing a CME, one can estimate the velocity of the out-flowing material. The highest speed was estimated by looking at the farthest datapoint that is enhanced as part of the CME feature, while the bulk velocity was determined by fitting a Gaussian into the CME feature, determining the central wavelength. If the Gaussian fit into the CME did not work, the bulk velocity was estimated using a mean value.

To estimate the mass the following relation from Houdebine, Foing, and Rodono (1990) was used:

$$M_{CME} \geq \frac{4\pi d^2 F_{em} \left(N_{tot}/N_j\right) m_h \eta_{OD}}{h \nu_{j-i} A_{j-i}} \tag{5.4}$$

Here, d denotes the distance of the star, F_{em} the integrated excess flux from the emission feature, N_{tot}/N_j the ratio between the total number of hydrogen atoms to the hydrogen atoms being in excitation level j, m_H the mass of the Hydrogen atom, η_{OD} the opacity damping factor (giving a value to indicate how much flux escapes the plasma due to optical thickness), h the Planck's constant, ν_{j-i} the frequency difference between excitation level j and i, and A_{j-i} the Einstein coefficient for spontaneous decay from the excitation level i to j.
While the CME candidates are most prevalent in the *Hα* line (transition from j= 3 to i = 2) there is so far no value in the literature to estimate the ratio N_{tot}/N_3. However, the transition for $H\gamma$ (j = 5, i = 2) is estimated to be $N_{tot}/N_5 = 2 \times 10^9$

by Houdebine, Foing, and Rodono (1990) using NLTE modelling. η_{OD} was set to 2, indicating that 50 % of the radiation escapes the plasma (Leitzinger, Odert, Greimel, et al., 2014), while the Einstein coefficient amounts to $A_{5-2} = 2.53 \times 10^6$ (Wiese and Fuhr, 2009).
As the SDSS spectra are covering the whole visible spectrum, the $H\gamma$ line is usable but poses difficulties due to bad SNR, especially for weak late type stars. Therefore, one may approximate the real value of the CME flux in $H\gamma$ by scaling the flux from $H\alpha$ with the Balmer decrement BD ($F_{em,\gamma} = F_{em,\alpha}/BD$), with BD set to 3 (adopted from solar and stellar flares, Butler, Rodono, and Foing, 1988). This work makes use of both $H\alpha$ and $H\gamma$ measurements for CME mass estimations.
For rough error estimations, the same method performed in the flare energy error analysis was used (see Equation 5.1). For all CME excess flux measurements, the flux as well as the errors of the coadded spectrum was used as reference. It is noted that the coadded spectrum has smaller errorbars due to the higher SNR, as it is the result of all spectra added together. The errors were determined only using the spectra and the star's distance. There are no estimations on the uncertainties of the total to excited hydrogen ratio, therefore this error source was omitted.

5.2.3. Wing asymmetries and variations

During visual inspection (manually done for each spectrum), all stars were noted where a possible enhancement or variation of any wing in either $H\alpha$ or $H\beta$ was suspected. If both showed changes in their wings, more Balmer lines were examined. This built the basis for the CME candidate list.
Overall, 136 SDSS spectra were noted where variations in chromospheric lines is suspected. The list consists of M stars only due to the large amount of examined active M stars showing high emission lines. The list includes the aforementioned CME candidates. 65 of the suspected wing asymmetry findings are part of the final flaring list, while 51 were sorted out of the flaring list by declaring the Balmer line core changes too small / not significant enough. 20 were found during the high emission line look through on M stars.
The number of found wing asymmetries correlates with the SNR of each object. 86 were found in the high, 29 in the middle, 16 in the low and only 5 in the worst SNR bin. This result is trivial as only high signals above the noise enables meaningful statements about variation in the wings.
These changes are not always significant; the findings are a summary of possible candidates for CMEs. The findings were not inspected as thoroughly as the final flare and CME candidate lists. Thus, the possibility of some findings only being wrong datapoints can not be ruled out. Most of the enhancements are expected to be enhanced wings from flaring activity in the stellar atmosphere. 50 objects show changes in both wings, most of these objects are included in the flaring list as expected. There is a slight over-representation of red wing changes (105) over

blue wing changes (81).

5.2.4. Special cases

Using the "CME-train" algorithm yielded in several finding (375 detections), one of which showed a possible CME-like feature that could not be explained by faulty data or CRs.
The star "SDSS J021450.83+060859.2" (found on plate 7256, MJD 56658, number 148) is marked as a K0V star in this spectrum, while it also appears in a second spectrum marked as a F9 subtype. The former spectrum is considered to be the primary spectrum of this star in SDSS. The spectra are displayed in Figure 5.20. The same spectra is displayed in Figure 5.21 including all errorbars. The combined spectrum is made up of 7 individual spectra, taken at two different days: 4 consecutive spectra spanning 66 minutes, and 3 consecutive spectra one day later, spanning 49 minutes. The first 4 spectra show an absorption feature on the blue wing of the $H\alpha$ absorption line, which is not changing its shape within these 66 minutes. The later 3 lines show no such feature and are consistent with the values from the other SDSS spectrum of the same star. The feature does not appear in any other Balmer line.
To rule out problems arising from the observation, other spectra from the same plate and same time were checked. These other objects did not show any form of similar feature. There are no dataflags in this spectrum to indicate problems, and no other unusual feature was found in the whole available spectrum.
We make the hypothesis that this absorption is caused by an expanding CME directly towards the line-of-sight. While 66 minutes is a long time, it is not implausible when looking at CMEs from the sun. No feature in $H\beta$ would mean, that the material is optically thick in $H\alpha$ only, which is a theory not considered in the search for other CMEs within this thesis.

If the CME hypothesis is used, the estimated velocity of the absorption would yield maximum values of $\sim 900\,\mathrm{km\,s^{-1}}$ and minimum values of $\sim 200\,\mathrm{km\,s^{-1}}$. The bulk velocity was determined by fitting a Gaussian onto the absorption (see Figure 5.22), yielding the value of $\sim 570\,\mathrm{km\,s^{-1}}$.

To further test the CME hypothesis, a mass estimation was performed using a relation from Odert, Leitzinger, Guenther, et al. (2019):

$$M = m_H N_H \frac{2F_{abs}}{\omega f_{cont}} \pi R_*^2 \tag{5.5}$$

here, m_H denotes the mass of the hydrogen atom, N_H is an estimation of the hydrogen column density of the prominence, F_{abs} is the integrated flux of the absorption feature, ω the FWHM of the feature, f_{cont} the mean value of the quiet

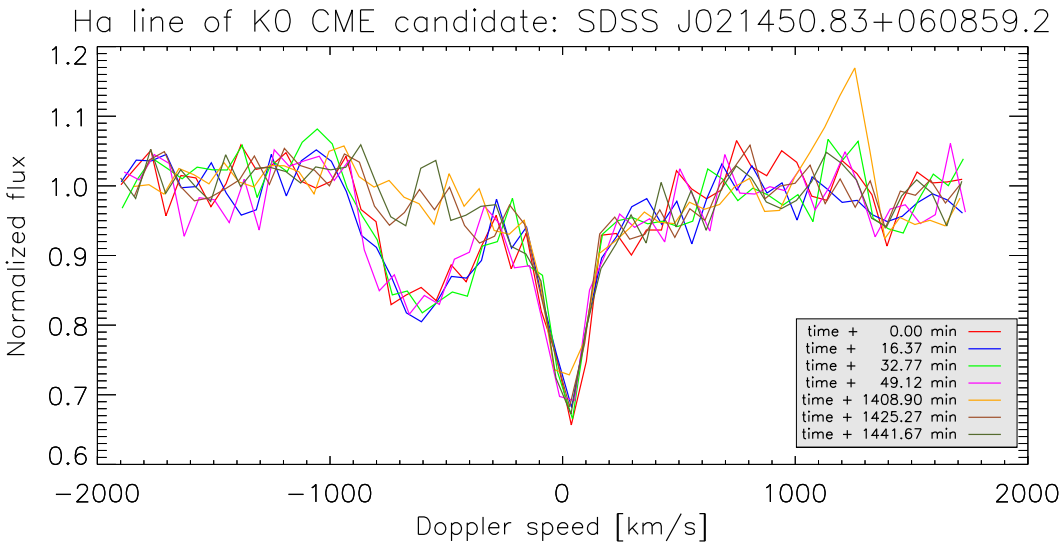

Figure 5.20.: *Hα* line of CME candidate with absorption feature. The starting times of all exposures are stated.

spectrum in the area of the feature and R_* the radius of the star.
For the column density, the value of $10^{20}\,\mathrm{cm}^{-2}$ was adopted (Odert, Leitzinger, Guenther, et al., 2019). The radius of the star was adopted from the GAIA dr2, which gives a value of $0.68\,\mathrm{R}_\odot$ (Gaia Collaboration et al., 2018). The other values were calculated using the spectrum: $F_{abs} = 2.06 \times 10^{-14}\,\mathrm{erg/s/cm^2}$, $\omega = 8.5\,\text{Å}$, $f_{cont} = 9.05 \times 10^{-16}\,\mathrm{erg/s/Å/cm^2}$.
The estimation of the mass resulted in a value of $8.2 \times 10^{18}\,\mathrm{g}$.

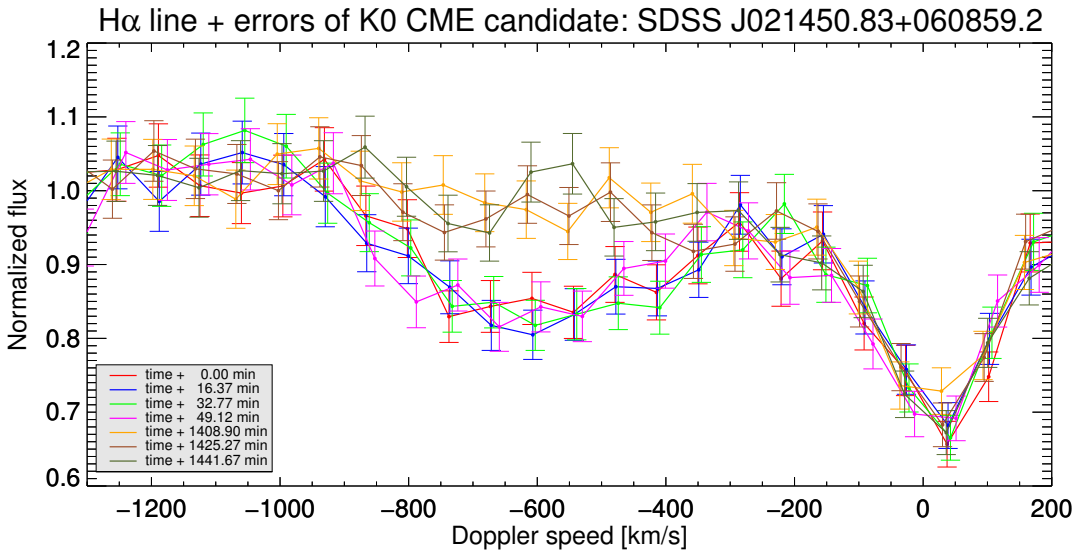

Figure 5.21.: *Hα* line of CME candidate with absorption feature. The starting times of all exposures are stated. This plot includes errorbars to display the significant change of the blue wing.

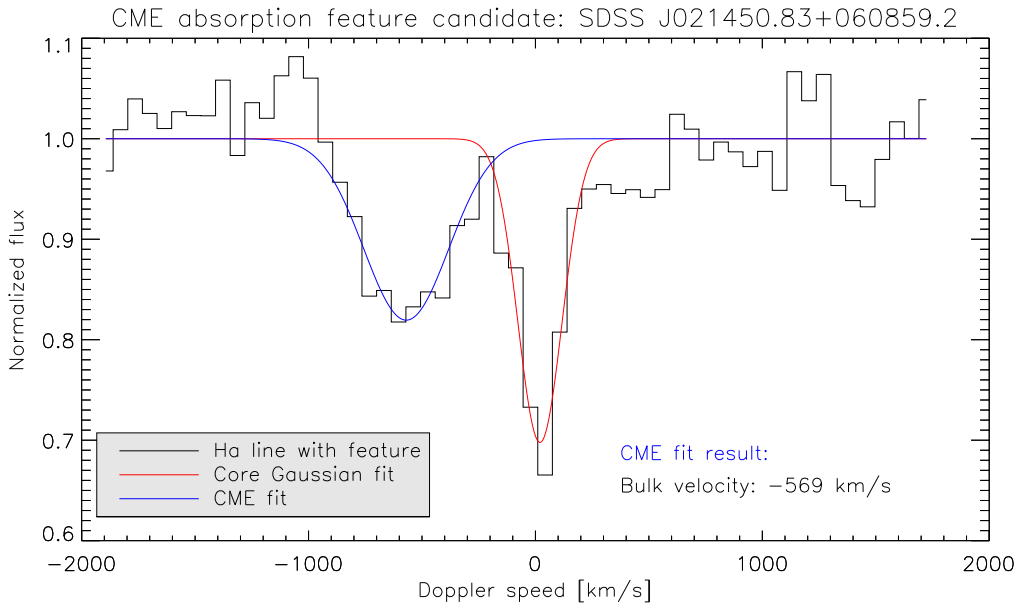

Figure 5.22.: *Hα* line of CME candidate with absorption feature. Core as well as the possible CME feature is fitted, with the bulk velocity of the Gaussian CME fit stated.

6. Discussion

Difference to Hilton et al. (2010)

Hilton et al. (2010) performed a search for flares on M-stars within an older data release of the spectroscopic SDSS data, finding 63 flaring events. While there is an obvious overlap with the presented work, there are substantial differences in both methodology and findings:

- The data release of the presented work is newer (DR 14 compared to DR 6), meaning that their objects are found within the given dataset.
- Hilton et al. (2010) pre-selected their sample using photometric SDSS flags and color selection to get M star spectral types. In this work, the original SDSS spectral classification was used and no selection criteria is used other than the restriction to F, G, K and M dwarf or subgiant stars. Photometric processing was not considered.
- Hilton et al. (2010) made high and middle SNR samples and did not consider low SNR objects. Their quality cuts were based on the continuum level compared to the standard deviations.
- The measurement of emission line strength in Hilton et al. (2010) was performed by defining a "flare line index" (FLI), where the mean value within the line region minus the continuum flux is divided by the continuum standard deviation. It measures the strength of the line and the significance compared to the surrounding noise. Their used flare criteria was either based on difference in FLI values between maximum and minimum exposures in $H\alpha$ and $H\beta$ or on threshold FLI values in strong emission lines. The latter method used a null distribution of non active stars to determine the quiescence emission line value and declared a flare threshold for each subtype each $H\alpha$ and $H\beta$ line and each SNR sample based on false discovery rate analysis.
  This method is quite distinct from the methods presented in this work, were Gaussian fits were used to tackle the low SNR problem in the data. Also, this work did not use flaring classification based on strong emission lines alone; temporal changes in the emission was mandatory to declare a flaring state.

Of the found 63 flares from Hilton et al. (2010), 41 (65 %) are part of the found flares in this work. Of the missing 22 flares, 8 were found by their strong emission line criteria only, which explains their non-detection. Of the remaining 14 flares,

one was found and declared as too small for flaring condition, two were found to have high emission lines but were declared by eye as non flaring and one was found by the high emission line search in the worst SNR bin, which was not controlled due to too many false detections. 10 remaining flares were not detected by any algorithm. These 10 objects are discussed in detail (see Appendix). The non-detections are caused by either too weak changes in one Balmer line, missing datapoints or cosmic ray hits in the spectrum that is used for the direct comparison.

Significance of findings and data quality

The bad data quality leads to a question whether found flares (and found CME candidates even more so) are significant at all or merely an artifact in the data. The highest possible SNR for single spectra in the dataset lies between 30 and 35, with most of the active K and M dwarfs having much lower SNR values. The spectral resolution is approximately two times oversampled, giving single enhanced datapoints (especially in the CME analysis) a lot of ambiguity. For flares, these problems were tackled by demanding that at least the $H\alpha$ and $H\beta$ Balmer lines are significantly enhanced while other Balmer lines were checked in addition. Significantly enhanced always denotes the value being higher than the combined error arising from the given errorbars. The errorbars of the original dataset are estimates of the 1σ error per pixel (Stoughton et al., 2002), assuming normal distribution for each pixel.
Similar to flares, CME candidates were only considered when the same wing shows any kind of enhancement in both $H\alpha$ and $H\beta$ and, if possible, in $H\gamma$. Long and successive enhancements above all other spectra were still considered, even with the single datapoints all lying within the errorbars.

Regarding the denotion of "Probable" flaring in the consideration categorization, a conservative approach was used. The categorization arose from a combination of flaring strength, noise in the data, visibility in other chromospheric lines and datapoint flags. The events are definitely in favor of showing flares. 4 flares with this flag are in fact also found in Hilton et al. (2010). The flag indicates that more care in using the values of these flares is necessary.

Notes on flare evolution estimation

The flare evolution estimation bears some ambiguity due to the long exposure times, as was already discussed. The assumptions are rough and the possibility of an intrinsic favoring of rise phases against decay phases is given.

Several M stars show highly active Balmer lines with significant changes, sometimes leading to observations of different phases (for example both a rise and a high activity at a different time). The more prominent and easier to categorize phase was chosen to represent the evolution of each set of spectra. For example, if rise and high activity at different time is visible, it was declared as rising due to the fact that activity at different time cannot be used to estimate consecutive evolution. The possibility of several flares in one set of spectra is thus not considered in the statistics.

Notes on flare energy results and flaring percentage

The lower threshold of flaring energy compared to the distance (see Figure 5.4) was expected (only large flares on distant stars are observable). On the other hand, the visible upper threshold showing no high energy flares within the surroundings of the solar system was not expected to this extend. The most probable explanation is a bias in the data arising from a selection effect. Checking the distances per subtype revealed that only few earlier flaring subtypes (K stars and M0 or M1 stars) in the given dataset are in the surroundings of the sun (within 200 pc). This leads to missing high energy flares on nearby stars due to energetic events being mostly visible on earlier types.
The fact that earlier types show higher maximum flare energies (see figures 5.6 and 5.5) is found in literature as well (e.g. Davenport (2016), Figure 5 or Balona (2015), Figure 10).

The result visible in Figure 5.1 is compatible with the result in Kowalski, Hawley, Hilton, et al. (2009), showing a rising flaring percentage until the type M6. Other than the presented result that uses spectroscopic analysis of Balmer lines, Kowalski, Hawley, Hilton, et al. (2009) used photometric lightcurves, giving the fraction of flaring epochs. West, Morgan, et al. (2011) determined the magnetic activity fraction for SDSS M dwarfs, conforming the found relation.

Notes on flare energy calculations

The high noise of the spectra renders the calculation of energy from excess $H\alpha$ emission difficult. A noisy reference spectrum could lead to a set of random enhancements in the wings being greater than the significant enhancement in the line core. These flares as well the ones having cosmic ray hits near the line were not further considered in the flare energy calculation.
With the low amount of datapoints to be integrated and SDSS providing different wavelength spacings for each single spectrum, the values were linearly interpolated to get useful results. Otherwise, the random shifts of the wavelength axis between the spectra could yield a different amount of datapoints per spectrum being within the chosen integration range, having valuable impact on the value

of the integrated area.
The final result in power and energy values is highly dependent on the distance, which was adopted from GAIA DR2 for each available star. Other sources were used if GAIA did not give a parallax for the object.
The calculated energies cover a large but expected range. With a dataset this big, some findings of extraordinary strong flares (beyond 10^{32} erg) are expected.
There appears to be no clear correlation between the power/energy of the flares and the SNR of the objects, which is a somewhat unexpected result. One may expect that only the strongest flares will get detected in the worst SNR data bin. The flaring strength mostly correlates with the distance, and it appears that the distances of the stars in the SNR bins are randomly distributed.

Improvements

With large datasets like this, the question always stands whether there is much more within the data that was not found due to inadequate methods.
Possible further approaches using either a Lorentzian or a Voigt profile may have lead to other, additional flares (while the Gaussian fit holds as a solid approximation, especially at this resolution).
Minor tweaks in the present methods may yield additional results, for example by changing the flaring criteria to Balmer line min/max change of all spectra, not just by comparing each line with the previous one. The problem of false fits for stars with no clear Balmer lines either in emission or absorption (for example active K stars) could also be tackled, as this made comparisons between consecutive lines impossible. The method used by Hilton et al. (2010) may be of use in this case; on the other hand, this work aimed to build methods from scratch instead of adopting them from literature.
Calculating equivalent widths and comparing these is another possible solution, especially valid for earlier types that show Balmer lines in absorption.
There is also the possibility of going for other lines than the Balmer lines, but lines like $H\alpha$ or $H\beta$ usually show a higher SNR and are obvious flaring indicators. Analyzing the calcium II triplet (CaT) of already found flares did not seem to be of additional use regarding stellar activity at this resolution, as the temporal changes seemed to be much lower and less significant compared to changes in $H\alpha$.

CME candidate findings

Of the 10 CME candidates showing Balmer line wing excesses presented in Section 5.2, 6 show a red and 4 a blue wing enhancement. CME candidate Nr. 2 (Figure 5.9b), Nr. 4 (Figure 5.11b) and Nr. 9 (Figure 5.18a) show an enhanced red wing during a flare. Assuming this is a CME feature, counter-intuitive to what is expected from the standard model of a CME onset, because the red-shifted

prominence material has to move away from the observer while the flare is directed towards the observer. There are two possible explanations for this feature: a) the huge flare causes a chain reaction in the magnetic field of the whole star, causing CMEs on the back side of the star to erupt, or b) the visible feature is cool plasma material falling back onto the surface of the star, albeit with unexpected high velocities (see below for further discussion on CME candidate velocity). For CME candidate Nr. 2 (Figure 5.9b) in particular, we stress that the last spectrum does not show the red wing enhancement anymore, while the line core is still distinctly enhanced compared to the "quiet" spectra. A possible explanation in this case (other than downfalling material) is the CME material getting ionized on its way, making it invisible in Balmer lines in the last spectrum.
CME candidate Nr. 10 (Figure 5.18b) shows a strong and wide wing enhancement during the flare similar to the candidates Nr. 2, 4 and 9, but here the excess flux is blue shifted, which is in agreement with the theory. CME candidate Nr. 6 (Figure 5.13b) has a similar characteristic (flare and wide blue wing enhanced), but the excess flux is much weaker and therefore the event is less reliable as a CME candidate.
CME candidate Nr. 1 (Figure 5.9a) has significant red wing enhancements in $H\alpha$, $H\beta$ and $H\gamma$, but only with either one or two enhanced datapoints each, making the detection more doubtful. CME candidate Nr. 3 (Figure 5.11a) on the other hand shows several enhanced datapoints in the red wing of each Balmer line, rendering it a great example of a possible CME in this dataset. Due to weak signals in the line enhancements, candidates Nr. 5 (Figure 5.13a), Nr. 7 (Figure 5.16a) and Nr. 8 (Figure 5.16b) are more doubtful CME candidates.

CME search, CME rates and non-detections

As was mentioned before, the found CME candidates pose a lot of ambiguity. While the derived masses are in agreement with expected results, it has to be noted, that deriving masses in these spectra even from small datapoint artifacts alone could yield similar results. Odert, Leitzinger, Guenther, et al. (2019) estimated minimum SNR ratios necessary to detect a certain amount of CME masses per stellar subtype. Their estimation for emission features (see Figure 1 in Odert, Leitzinger, Guenther, et al., 2019) shows, that for stars of type M 5.5 a minimum SNR of ~ 20 is at least necessary to detect CME masses above 2×10^{14} g in $H\alpha$. For stars of type M2, the detectable CME masses with a SNR of ~ 20 rises to $\sim 10^{16}$ g in $H\alpha$. The SNR near $H\alpha$ of the presented list of candidates ranges between 13 and 28; their derived masses lie well above the estimated minimum detectable value estimated by Odert, Leitzinger, Guenther, et al. (2019). The values are summarised in Table 6.1 (mass estimations arising from measurements in the $h\gamma$ wings are omitted in this table due to their ambiguity arising from bad SNR). One has to take the limited spectral resolution into account, which brings up

Nr.	Enhanced Wing	Type	Mean SNR in $H\alpha$	Est.mass $H\alpha$ [g]	Est.mass error [%]
1	red	M3.2	28	3.9 E+17	81
2	red	M4e	22	8.4 E+17	22
3	red	M4e	28	7.9 E+16	51
4	red	M6	17	1.1 E+18	11
5	red	M5e	17	8.5 E+15	120
6	blue	M9e	13	1.6 E+15	44
7	blue	M7e	13	2.9 E+15	68
8	blue	M4e	25	4.9 E+17	67
9	red	WTT	21	-	-
10	blue	M4e	24	7.9 E+18	19

Table 6.1.: CME candidates with associated types, mean SNR near $H\alpha$ and estimated CME masses with errors (based on $H\alpha$ wing excess flux).

the question whether a single enhanced datapoint can be used to deduct meaningful physical properties. One faulty enhanced point (below spectral resolution limit) in this dataset might yield a CME mass estimation which would be in agreement with the given minimum SNR estimation. The error calculation can be compromised too, as the errorbar of one single faulty datapoint does often not corresponds to the real error. The errorbars are mere estimations automatically generated by the SDSS pipeline.

Considering the minimum SNR - CME mass detection estimation by Odert, Leitzinger, Guenther, et al. (2019), for the large number of late type M stars with their expected high activity phenomena in the given dataset and the assumed high association rate between high energy flares and CMEs (based on solar values), the amount of found candidates for CME-like features is surprisingly low. Explanations for the sparse findings based on the dataset quality may be (as was mentioned before) a) bad spectral resolution or b) flares giving wing enhancements that may over-shine an otherwise possible CME like feature. The long exposure times are another explanation for non-detection, as these integration times (up to 25 minutes) may diminish a short time flux enhancement.
A physical explanations for sparse CME findings may lie in CMEs getting suppressed by strong overlying magnetic field of the star, as was suggested by Alvarado-Gómez et al. (2018). This would result in a significant weakening of radial velocity, suppressing weaker CMEs while only huge ejections could break free (Vida, Leitzinger, et al., 2019). Nonetheless, there is only one detection of a clear and detached (absorption) feature indicating a possible CME in this dataset, while no clear and detached emission features were found.
Another explanations lies in expanding, density decreasing and (adiabatic) cooling of fast CMEs, making it undetectable in the Balmer line (Leitzinger, Odert, Greimel, et al., 2014; Odert, Leitzinger, Hanslmeier, et al., 2017; Vida, Leitzinger, et al., 2019). The other way is also possible, with the prominence material getting ionized too early in the hot coronae of M stars, which would suggest, that their coronae are different than the solar corona (Leitzinger, Odert, Greimel, et al., 2014;

Odert, Leitzinger, Hanslmeier, et al., 2017; Vida, Leitzinger, et al., 2019). More information on the temperatures of different stellar atmospheres is necessary to make conclusions based on this theory.

Alternative explanations for found CME candidates and asymmetries arise by using the connection to flares. Balmer line asymmetries are generally associated with chromospheric material moving either downwards or upwards. Blue-shifted $H\alpha$ emission could arise from chromospheric evaporation, where material rises up into the flaring loop. The associated velocities to this mechanism on the sun is usually in the range of tens of kms^{-1}, way below the estimated velocities for the blue-shifted CME candidates. Gunn et al. (1994) reported a blue wing emission feature similar to the presented CME candidates as a high velocity evaporation (max $600\,\mathrm{kms}^{-1}$) during a flare, while the possibility of an associated CME was not discussed.
Red-shifted $H\alpha$ emission may arise from downward moving material (chromospheric condensation) or cooling flows along flare loops (Vida, Leitzinger, et al., 2019). Solar red wing asymmetry reported by Asai et al. (2012) is in range of $50\,\mathrm{km}^{-1}$, which is also way below our found values up to a maximum of 700 kms^{-1}. One also has to keep in mind that all CME velocity estimations work with projected velocities only, diminishing the true value by an unknown amount.

This work did not employ an upper occurrence rate estimation on stellar CMEs due to the large number of spectra that are probably too low in SNR to get used to perform a reasonable CME search. The overall observation time that is usable for CME analysis thus gets greatly diminished. The same problem holds for flares, but these are much easier to detect and thus are less dependent on the SNR. The upper limit on CME occurrence rate would need an in depth calculation considering all SNR rates around each $H\alpha$ line of each M star.

New questions arise with the finding of the K0V star that shows an absorption in the blue wing of $H\alpha$, as the absorption is visible in this range only. The first assumption that this might be an artifact representing wrong datavalues is not supported by any additional facts other than the feature itself. The Doppler-shifted velocity is perfectly in range of what would be expected of a CME, and the feature is clearly detached from the line core. The estimated mass of the feature, albeit being really high compared to solar values ($\sim 8 \times 10^{18}\,\mathrm{g}$, is not unrealistically beyond usual values. The feature is visible for at least 66 minutes, which is a fairly long time, especially considering that this kind of absorption associated with an CME was never reported before. The question whether a feature is visible in $H\alpha$ only, meaning that it is only optically thick in $H\alpha$ and optically thin in other Balmer / chromospheric lines, needs to be further investigated. This might be done using NLTE modelling of stellar atmospheres. The possibility of CME material being optically thick in one Balmer line only would change the whole approach to search for CMEs in optical spectra.

Outlook

While this work focused on main-sequence stars, one may shift the focus to include more pre-main-sequence stars in order to search for CMEs, as these objects are known for their frequent activity.
Better instrumentation is needed to increase the possibility and significance of CME detections. Long observing times are necessary, which poses the problem that it would block the used telescope for other scientific cases. Therefore, the establishment of a flare alert system like the one presented by Hanslmeier et al. (2017) might be a promising concept. Using continuous photometric observations with small telescopes, a detected flare can be reported in real time to larger observatories to conduct spectroscopic observations.

Appendix

Appendix A.

Missing flares of Hilton et al. (2010)

Using notation from Hilton et al. (2010), Table 3, the stars are identified by their right ascension and declination coordinates.

Star R.A. 355.347630 and Decl. -0.646637 : This M1 star in the high SNR bin probably showed too little variation in $H\alpha$ line height for detection. It was probably not found by the high emission line algorithm due to the high continuum flux compared to the $H\alpha$ line height.

Star R.A. 128.514690 and Decl. 23.718951 : This M3 star in the high SNR bin shows flaring activity in later Balmer lines, but not in $H\alpha$.

Star R.A. 134.892240 and Decl. 28.224011 : This M3 star in the high SNR bin shows small variation (decay) in one spectrum. It was probably not detected due to too small temporal changes in $H\beta$.

Star R.A. 154.133280 and Decl. 36.066472 : This M3 star in the high SNR bin shows slowly decaying emission lines. The changes in $H\alpha$ are most likely too small for detection.

Star R.A. 179.329230 and Decl. 36.899333 : This M3 star in the high SNR bin shows too little changes in $H\alpha$. One smaller line in $H\alpha$ does not appear smaller in $H\beta$.

Star R.A. 8.116274 and Decl. -0.669970 : This M4 star in the high SNR bin shows a significantly high rising flare. There was probably no detection due to a cosmic ray hit near the peaking spectrum in $H\beta$, messing up the Gaussian fit.

Star R.A. 123.544780 and Decl. 7.833261 : This M4 star in the middle SNR bin shows variation of the lines, but too little to get detected with the present algorithms. The temporal change between flaring spectra in $H\beta$ appears to be too small.

Star R.A. 237.126050 and Decl. 51.509009 : This M4 star in the high SNR bin shows a huge flare visible in all chromospheric lines. The flare was not detected due to missing datapoints in the wing of the $H\alpha$ line.

Star R.A. 329.517010 and Decl. -8.355448 : This M6 star in the low SNR bin shows its last spectrum with flaring emission lines. It was probably not detected due to the previous spectrum in $H\beta$ showing only a cosmic ray hit, giving rise to a faulty temporal comparison between quiet and flaring spectra.

Star R.A. 182.070410 and Decl. 8.757879 : This M9 star in the worst SNR bin shows a clear flare in the Balmer lines in its last spectrum. Like the previous star, it may be not detected due to a cosmic ray hit near the Balmer line in the previous spectrum in $H\alpha$.

Appendix B.

Complete list of found flaring late-type stars

The complete list of flares found by this work is given by the tables B.1, B.2, B.3, B.4 and B.5.
The included columns in the tables are:

- RA and DEC: Right Ascension and declination of the object in degrees.
- Search Method: what method yielded the detection of this object. Following abbreviations are used:
  A1 ... Gauss peak difference (high threshold)
  A2 ... Gauss peak difference (low threshold)
  E ... Emission line look through
  R ... Re-evaluated flares also found by Hilton et al. (2010) that were originally sorted out after visual inspection
- SNR Bin: Categorization of object into specific SNR bin (see Section 3.3)
- Spec. Type (Literature): Spectral type of object based on literature search
- Spec. Type (Source): Source of the spectral type in the previous column. Following abbreviations are used:
  S1 ... West, Morgan, et al. (2011); S2 ... West, Hawley, Bochanski, et al. (2008); S3 ... Kleinman et al. (2013); S4 ... Cook et al. (2016); S5 ... McGehee (2006); S6 ... Guieu et al. (2006); S7 ... Newton et al. (2014); S8 ... Briceño et al. (2019); S9 ... Kraus and Hillenbrand (2009); S10 ... Luhman et al. (2017); S11 ... Zhang et al. (2010); S12 ... Morgan et al. (2012); S13 ... Kowalski, Hawley, Hilton, et al. (2009); S14 Zhong et al. (2015); S15 ... Skiff (2014); SDSS ... Spectral type from SDSS file if no literature was available
- Spec. type (SDSS): Original spectral type designation from .fits file header provided by SDSS.
- Distance (pc): Reported distance of star in parsec.
- Distance (Source): Source of the distance used in the previous column. If no specific source is given, Gaia Collaboration et al. (2018) was used (see Section 3.5). Following abbreviations are used:
  D1 ... Jones and West (2016); D2 ... West, Morgan, et al. (2011); D3 ... Stassun et al. (2018); D4 ... Theissen et al. (2017)

- Quiet flag: Indication, whether reference spectrum for calculating flaring energy was quiet.
  1 ... Quiet reference
  2 ... Reference spectrum probably quiet
  0 ... Reference spectrum has problems (e.g. cosmic ray hit), energy calculation not reliable
- Flares evol. estimation: Estimation of the evolution visible in the spectra (see Section 5.1.1 and the discussion in Chapter 6). Following abbreviations are used:
  "rise" / "p. rise" ... flaring rise / probably rise
  "decay" / "p. decay" ... flaring decay / probably decay
  "unclear" ... activity visible, but not possible to declare evolution
  "diff. activity" ... the flare is happening at a different time, no evolution visible
  "evolution" ... both rise and decay as well as a peak is visible
- Consideration flag: indication of how reliable the flare is using either "Yes" or "Probable" (see Section 4.1.4 and the discussion in Chapter 6).
- In Hilton et al. 2010: Indicating whether the flare was also found by Hilton et al. (2010).
- Platequality: Read out from the SDSS .fits file header. Plate quality can either be "good", "marginal" or "bad".
- Ha energy (erg): Calculated $H\alpha$ flare energy (see Section 5.1.5).
- Error (erg): Calculated $H\alpha$ flare energy error (see Section 5.1.5).
- Comments: Subjective comments added during the look-through of the flares. Often used abbreviations and notes:
  (Subjective) significance and size of the flare using the designations "big", "middle", "small" and "mini" (see Section 4.1.4).
  cons. .... indicates whether the flare is in a consecutive series of spectra.
  Notes on wing variability: e.g. "ha hb hg hd both wings" means enhanced wings in $H\alpha$, $H\beta$, $H\gamma$, and $H\delta$. The mentioning of a Balmer line wing means that there is the possibility of an enhancement. Possible absorptions are mentioned separately. "CME?" indicates, that this event was analysed in depth to conclude, whether a CME did happen.
  "New emission line" or "new em. line" ... indicates, whether the flare produced a Balmer emission line where previously no emission line was visible (good indicator for flaring activity).
  Other notes include: visible shifts in the data, high noise values, "cont. em?" as the possibility of enhanced continuum emission due to the flare and many available spectra (as "many datapoints").

Note: This is a mere summary of important values; there was considerably more information gathered on each object (e.g. all spectra crosschecked from SDSS photometric catalogues in VizieR, all values from GAIA DR2, in-depth notes on flags and problems of each flare, notes on which spectra are in flaring state, cosmic ray hits near $H\alpha$ as well as all calculated flaring powers, energies and errors). The

Tables including all gathered values as well as the tables with information on the CME objects and the full wing asymmetry list is available at the IGAM servers. Please contact the author to gain access to this data.

RA deg	DEC deg	Search Method	SNR BIN	Spec. Type Literature	Spec. Type Source	Spec.Type SDSS	Distance pc	Distance Source	Quiet flag	Flare evol. estimation	Consideration Flag	In Hilton et al. 2010	Platequality	Ha energy erg	error erg	Comments
146.83368	-0.33597	A1	high	M7e	S1	M6	26.7832			p. decay	Yes		good	3.7E+28	1.3E+28	small, big in hb, cons.
225.10974	-0.657786	A1	high	M7e	S1	M6	33.8737			evolution	Probable		good	2.0E+29	4.5E+28	small, cons.
51.664902	-6.299639	A1	high	M6e	S1	M6	47.3	D1		decay	Yes		good	6.4E+29	7.7E+28	small, cons., ha hb hg hd both wings
116.7287	36.041374	A1	high	M6e	S1	M5	38.9066		1	unclear	Yes	Yes	marginal	1.2E+30	6.5E+28	small, many datapoints, wing variations
131.82185	3.014382	A1	high	M4e	S1	M4	81.5189		1	decay	Yes	Yes	marginal	7.1E+30	3.1E+29	middle, ha red wing, hb blue wing
328.15564	-7.89591	A1	high	M4e	S1	M4	116.205			p. decay	Probable		marginal	1.2E+30	4.8E+29	middle, hb red wing
21.297153	-0.448107	A1	high	M4e	S1	M4	129.638		1	diff. activity	Yes		marginal	4.5E+30	4.8E+29	middle, ha wing enhanced + absorption
27.197636	0.241484	A1	high	M6e	S2	M6	30.6872			p. decay	Yes		good	3.5E+29	3.1E+28	small, cons.
34.359509	-0.554997	A1	high	M2e + Da	S3	M2	376.209		1	diff. activity	Yes		marginal	1.4E+32	7.1E+30	big, red wing shift
146.86066	54.302231	A1	high	M5e	S1	M4	124.831		2	diff. activity	Yes		marginal	6.7E+30	5.5E+29	small, ha blue wing, hb other blue wing
214.41065	59.650318	A1	high	M6e	S1	M5	43.8059			evolution	Probable		good	5.2E+29	6.9E+28	middle, cons., ha red wing
135.96791	47.018555	A1	high	M3.5	S4	M4	120.084			p. decay	Probable		marginal	6.6E+30	8.5E+29	small, cons., ha blue wing
140.53719	40.925426	A1	high	M6e	S1	M6	32.7969			evolution	Yes		marginal	1.2E+29	1.9E+28	small, cons., ha blue wing
127.17438	13.295162	A1	high	M4	SDSS	M4	173.001		1	decay	Yes		good	1.5E+31	1.2E+30	middle, ha wings, hb red wing
75.90654	-2.99434	A1	high	M2	SDSS	M2	456.496			diff. activity	Yes		good	1.5E+32	5.8E+30	one big line
76.616013	-3.340849	A1	high	M4.5	S4	M5	173.551			diff. activity	Yes		good	2.9E+31	2.0E+30	middle, many datapoints
20.530289	0.543299	A1	high	M4e	S1	M4	151.923		1	diff. activity	Yes		good	1.6E+31	1.2E+30	one spec without flare
313.00403	-0.371448	A1	high	M5e	S1	M5	89.798			slow rise	Yes		good	1.4E+30	2.2E+29	middle, cons., ha red wing
8.968297	-0.388641	A1	high	M5e	S1	M4	115.591		2	diff. activity	Yes		marginal	2.5E+30	3.8E+29	middle
8.593903	0.291741	A1	high	M4e	S1	M4	383.921		1	diff. activity	Yes		good	8.5E+30	2.4E+30	middle
13.778212	-0.950669	A1	high	M4e	S1	M4	180.034			unclear	Probable		good	1.5E+31	2.2E+30	middle, cons., shift
83.181114	-0.812375	A1	high	M5	SDSS	M5				rise	Probable		bad	0.0E+00	0.0E+00	small, cons.
82.941521	-0.843048	A1	high	M4e	S1	M4	375.305			decay	Probable		bad	1.7E+32	1.6E+31	small, cons., line shift
82.165283	-0.056267	A1	high	M4e	S1	M4	467.771			decay	Probable		bad	2.5E+32	9.8E+30	middle, cons., ha shift, hb blue wing
84.291336	-1.18067	A1	high	WTT	S5	M5				sudden rise	Probable		bad	0.0E+00	0.0E+00	one big line, big red asymmetry
83.802437	-0.702625	A1	high	M3	SDSS	M3	394.337			p. decay	Probable		bad	1.5E+31	4.8E+30	small
83.556282	-1.122456	A1	high	WTT	S5	M3	420.964		0	p. decay	Probable		bad	1.9E+32	3.2E+31	small or mini, wing enhanced in ha hb
85.555069	0.264564	A1	high	M4	SDSS	M4	415.403		2	diff. activity	Probable		bad	5.6E+31	4.8E+30	middle, wings enhanced
86.20948	1.0793	A1	high	M5e	S1	M4	93.5261			evolution	Probable		bad	1.4E+30	4.3E+29	small
245.11481	36.667454	A1	high	M4e	S1	M4	303.49		2	diff. activity	Yes		good	4.4E+30	1.1E+30	middle, shift, ha wings
230.8392	34.886509	A1	high	M4e	S1	M4	110.657			rise	Yes		marginal	3.9E+30	5.6E+29	small, cons.
151.16177	39.817059	A1	high	M5e	S1	M5	78.2191		1	p. decay	Yes	Yes	good	5.3E+30	2.9E+29	middle, wings enhanced
335.0863	0.411424	A1	high	M6e	S1	M5	47.1311		1	diff. activity	Yes		good	1.4E+29	3.3E+28	small, ha wings
10.962794	0.012733	A1	high	M3e	S1	M3	523.122		0	diff. activity	Yes		good	-1.4E+30	6.2E+30	small or cosmic
28.154886	0.943767	A1	high	M4e	S1	M4	227.505			rise	Probable	Yes	good	3.9E+31	2.0E+30	middle, cons., hb red wing CME?
44.965473	0.771972	A1	high	M5e	S1	M6	106.86		2	evolution	Probable		marginal	9.0E+30	9.4E+29	small, cons., ha wings
46.008732	0.764225	A1	high	M6e	S1	M6	29.6545			evolution	Probable		marginal	8.0E+29	5.5E+28	small, cons., hb wings
47.477882	0.460924	A1	high	M5e	S1	M5	93.6295			evolution	Probable		good	5.8E+29	2.9E+29	small, cons.
57.750114	-0.879412	A1	high	M7e	S1	M7	14.6989			p. decay	Probable		good	9.8E+28	1.1E+28	small, cons.,ha hb wings
248.08604	23.949038	A1	high	M5e	S1	M5	67.2273			rise	Yes	Yes	good	1.7E+30	1.5E+29	small, cons.
239.47389	29.815516	A1	high	M5e	S1	M5	143.476			p. decay	Yes		good	1.3E+30	4.7E+29	small, cons.
132.64668	29.973049	A1	high	M5e	S1	M4	152.253			p. decay	Yes		marginal	2.9E+30	6.3E+29	small, cons.
163.76196	11.930522	A1	high	M5e	S1	M4	95.0932			rise	Yes		marginal	4.5E+30	4.3E+29	middle, cons., ha blue wing
67.517387	16.068888	A1	high	M6	SDSS	M6	361.324			rise	Yes		bad	6.5E+31	8.1E+30	small, cons., ha possible red wing
66.776787	16.430063	A1	high	M6	SDSS	M6	46.0887			rise	Yes		bad	2.1E+29	6.8E+28	small, cons., hb wings
65.397827	16.894363	A1	high	M5	SDSS	M5	43.9771			evolution	Probable		bad	5.7E+30	5.9E+29	small, cons. , possible blue wing enhanced
66.4459	17.544653	A1	high	M5e	S1	M5	38	D2	2	evolution	Probable		bad	1.5E+30	2.7E+29	small, cons., wings enhanced
66.517982	17.12072	A1	high	M5e	S1	M5	30.9	D2		decay	Probable		bad	1.9E+31	9.6E+29	small, cons., red wings
64.456398	28.2255	A1	high	M5.5IVe	S6	M6	137.37			rise	Probable		bad	3.3E+31	3.2E+30	small, cons., hb wings
70.209999	24.603399	A1	high	M4	SDSS	M4	137.344		2	evolution	Probable		good	1.0E+31	2.0E+30	small, cons., many datapoints
49.862267	40.066494	A1	high	M4	S1	M4			1	diff. activity	Probable		good	0.0E+00	0.0E+00	middle, many datapoints
227.86179	44.155331	A1	high	M5e	S1	M4	68.3896			evolution	Yes		good	2.0E+29	1.1E+29	small, cons.
247.80444	31.749735	A1	high	M4e	S1	M4	214.174			rise	Yes		good	5.7E+30	1.8E+30	small
256.99539	22.788597	A1	high	M5e	S1	M4	111.026		1	diff. activity	Yes		good	1.2E+30	3.9E+29	small, hb wings
244.10886	7.428527	A1	high	M5e	S1	M5	89.1313			p. decay	Probable		good	3.0E+30	4.3E+29	small
203.68723	14.907484	A1	high	M6e	S1	M5	95.2526			rise	Yes		good	6.7E+29	1.6E+29	middle
218.62013	32.732052	A1	high	M5e	S1	M4	145.845		2	diff. activity	Yes		good	3.8E+30	6.6E+29	small, asymmetric blue line
131.44402	27.391935	A1	high	M6e	S1	M5	117.868		2	diff. activity	Yes		good	4.9E+30	5.8E+29	middle or small
131.81371	27.05574	A1	high	M5e	S1	M4	67.7053		1	diff. activity	Yes		good	4.8E+29	1.3E+29	middle
133.10251	25.683031	A1	high	M7e	S1	M6	43.497			unclear	Yes		good	3.1E+29	7.7E+28	small, cons.

Table B.1.: Detected flaring spectra. A detailed description of the content is given at the begin of this chapter.

RA deg	DEC deg	Search Method	SNR BIN	Spec. Type Literature	Spec. Type Source	Spec.Type SDSS	Distance pc	Distance Source	Quiet flag	Flare evol. estimation	Consideration Flag	In Hilton et al. 2010	Platequality	Ha energy erg	error erg	Comments
174.94681	39.499439	A1	high	M5e	S1	M5	62.2975		2	evolution	Yes		marginal	1.8E+30	1.8E+29	middle, possible hb red wing
137.21883	25.206903	A1	high	M4e	S1	M4	149.869			p. decay	Yes	Yes	marginal	1.1E+31	5.7E+29	big, cons., wings enhanced
163.1069	37.365356	A1	high	M6e	S1	M5	38.889			rise	Yes	Yes	good	3.4E+29	4.2E+28	middle, cons., possible blue wing ha hb
181.06226	32.772865	A1	high	M6e	S1	M6	42.3105		1	rise	Yes	Yes	good	1.1E+30	4.8E+28	big, cons., wings enhanced
244.0479	14.758066	A1	high	M5e	S1	M4	113.058		2	rise	Probable		good	1.8E+31	8.8E+29	big flare in ha, possible wrong data
245.87633	14.528161	A1	high	M5e	S1	M4	184.942			diff. activity	Yes		good	6.3E+30	7.3E+29	small or middle
251.36629	13.649387	A1	high	M2e	S1	M2	230.532			diff. activity	Yes		good	7.7E+30	1.0E+30	small
133.98612	17.828348	A1	high	M4e	S1	M4	234.165		2	diff. activity	Yes		good	1.6E+31	1.2E+30	small, red wing, CME contender
135.50452	20.896919	A1	high	M4e	S1	M4	181.169			diff. activity	Yes		marginal	9.0E+30	9.3E+29	small
137.87724	22.802999	A1	high	M7e	S1	M6	21.9	D2	1	p. decay	Probable		good	9.1E+29	3.0E+28	middle, hb blue wing
142.82671	26.237862	A1	high	M4e	S1	M3	262.771		1	diff. activity	Probable		marginal	6.9E+30	1.1E+30	small
153.57832	26.29591	A1	high	M5e	S1	M5	89.5825			diff. activity	Probable		marginal	5.1E+30	3.7E+29	middle
164.2802	26.23797	A1	high	M2e	S1	M2	394.804			rise	Probable		good	1.7E+32	4.4E+30	big, cons., one wrong spectrum
154.30232	22.335365	A1	high	M5e	S1	M4	81.211		2	diff. activity	Yes		marginal	4.0E+30	3.6E+29	small, ha wings enhanced
154.50961	22.508436	A1	high	M4e	S1	M4	129.993		2	diff. activity	Yes		marginal	2.4E+31	9.2E+29	small
156.66344	22.958412	A1	high	M4e	S1	M4	145.035			rise	Probable		good	6.1E+30	7.1E+29	middle, cons.
155.85814	19.937998	A1	high	M6e	S1	M5	136.998		2	rise	Yes		good	3.8E+30	3.7E+29	small
152.11742	26.625694	A1	high	M0e	S1	M0	424.286		2	diff. activity	Yes		good	3.0E+31	6.6E+30	small, cosmic ray
163.01347	0.544043	A1	high	M4V	S7	M4	39.8138		2	diff. activity	Probable		good	1.7E+30	3.7E+29	middle, ha red and blue wing
120.49913	10.519128	A1	high	M4e	S1	M4	222.168		2	unclear	Yes		marginal	3.4E+31	2.7E+30	small, hb hg wing enhanced
132.04105	13.035116	A1	high	M6e	S1	M5	98.4204			diff. activity	Yes		marginal	2.0E+30	2.5E+29	middle
173.56552	20.781763	A1	high	M6e	S1	M5	31.1269			rise	Yes		good	3.6E+29	4.3E+28	small, cons.
157.55618	15.183814	A1	high	M4e	S1	M4	105.3	D2	2	p. rise	Yes		good	3.3E+30	5.4E+29	small, hb wing enhanced
181.05025	20.036539	A1	high	M4e	S1	M4	343.395		2	unclear	Probable		good	2.6E+30	5.4E+30	middle, high noise
206.32639	23.659437	A1	high	M3e	S1	M2	315.597		2	diff. activity	Yes		good	4.4E+31	6.1E+30	small
212.5434	18.769993	A1	high	M6e	S1	M5	38.5465		1	rise	Yes		marginal	6.8E+29	8.1E+28	middle
206.88586	22.11492	A1	high	M6e	S1	M5	53.9721		1	diff. activity	Yes		good	5.0E+29	4.7E+28	small
209.10953	23.09729	A1	high	M4e	S1	M4	98.6767			evolution	Yes		good	2.7E+30	6.4E+29	small,hb red wing enhanced,blue wing abs.
122.64737	-6.069219	A1	high	M4e	S1	M4	185.388			diff. activity	Probable		good	2.1E+31	1.7E+30	small flare
221.51769	63.950817	A1	high	M5e	S1	M4	199.681		0	diff. activity	Yes		good	-4.1E+30	1.2E+30	one small wide line
245.64414	19.383097	A1	high	M4e	S1	M4	154.689		1	decay	Yes		good	1.3E+31	1.4E+30	big flare, wings enhanced
73.356911	-5.749764	A1	high	M4	SDSS	M4	205.385		1	decay	Yes		good	4.4E+31	1.7E+30	big, many datapoints,wings enhanced
152.47575	20.348604	A1	high	M4	SDSS	M4	83.2979		1	diff. activity	Probable		good	4.1E+30	2.5E+29	middle
352.711212	-0.684079	A2	high	M3e	S1	M3	159.5	D2	2	diff. activity	Yes		good	4.3E+30	7.4E+29	middle
84.178802	-1.026140	A2	high	M3.5	S4	M4	220.8906	D3	2	diff. activity	Probable		bad	3.3E+31	3.4E+30	small
48.102718	-0.802344	A2	high	M4e	S1	M4	180.695			p. rise	Yes		good	6.2E+30	1.2E+30	small, cons., high noise
186.034561	36.741596	A2	high	M5	S1	M4	89.707		1	decay	Yes		good	3.6E+29	1.1E+29	small, cons., high noise, new hb emission line
233.658813	30.819677	E	high	M5e	S1	M5	156.24			rise	Probable		marginal	6.5E+30	1.0E+30	small, cons., ha hb red wing asymmetry
135.152817	20.994905	E	high	M6e	S1	M6	40.3	D2		unclear	Yes		marginal	3.3E+29	4.2E+28	small
238.975327	0.807979	A1	middle	M5e	S1	M5	75.6304			unclear	Yes		good	1.6E+30	2.2E+29	small, cons., many datapoints
116.053619	41.686867	A1	middle	M6e	S1	M6	51.6799		1	p. decay	Yes	Yes	good	9.5E+29	5.7E+28	middle
49.663315	-7.054426	A1	middle	M5e	S1	M5	66.3	D2		rise	Yes		good	6.9E+29	1.5E+29	small, cons.
135.528793	0.555384	A1	middle	M8e	S1	M7	21.7328			evolution	Yes	Yes	good	3.1E+29	1.2E+28	middle, cons.
225.053314	60.903133	A1	middle	M6e	S1	M5	49.3143			rise	Yes	Yes	good	2.1E+30	6.7E+28	big, cons., enhanced wings
136.041824	42.068287	A1	middle	M5e	S1	M5	45.1465			unclear	Probable	Yes	marginal	8.4E+29	8.0E+28	middle, cons.
37.750614	24.505690	A1	middle	M4	SDSS	M4	176.211			unclear	Yes		good	8.3E+30	1.1E+30	middle, many datapoints, wings enhanced
16.513277	1.163345	A1	middle	M1	SDSS	M1	756.315			evolution	Yes		good	7.3E+31	1.5E+31	small, high noise
155.637817	46.632072	A1	middle	M5e	S1	M5	163.188			evolution	Yes		marginal	2.7E+30	4.3E+29	small, cons., blue wing absorption in ha hb
162.490067	5.932383	A1	middle	M5e	S1	M5	105.516			rise	Yes		marginal	1.6E+30	2.9E+29	small, cons., hb blue wing
246.657104	34.375595	A1	middle	M3e	S1	M3	466.2		2	rise	Yes	Yes	good	2.0E+31	2.4E+30	big, cons., high noise, new emission line
53.652840	0.496465	A1	middle	M5e	S1	M5	210.744		2	diff. activity	Probable		bad	4.4E+31	2.3E+30	small, hb wings enhanced
9.787901	1.142402	A1	middle	M5e	S1	M5	110.618		2	diff. activity	Yes		good	2.7E+30	2.2E+29	small, ha wings enhanced
84.926285	-0.659990	A1	middle	M5	SDSS	M5	329.131			p. rise	Yes		bad	6.8E+31	5.8E+30	middle, ha hb both wings
83.795654	-1.237497	A1	middle	CWTT	S8	M6	419.903		2	p. decay	Yes		bad	1.2E+32	9.9E+30	small
65.775291	28.022131	A1	middle	M6.25	S9	M7	133.881		2	p. rise	Probable		good	2.0E+31	5.4E+29	small
123.690750	5.846943	A1	middle	M6e	S1	M5	122.035			decay	Yes		good	2.2E+30	2.3E+29	small, cons.
213.019836	54.689850	A1	middle	M6e	S1	M5	106.176		2	diff. activity	Yes	Yes	good	1.9E+30	1.4E+29	small
231.358093	35.709362	A1	middle	M3e	S1	M3	273.8		2	rise	Yes	Yes	marginal	7.3E+30	1.1E+30	small, cons.
161.540237	42.759010	A1	middle	M3e	S1	M2	372.662		2	p. decay	Yes	Yes	good	3.1E+31	3.5E+30	middle, hb red wing absoprtion
194.240585	42.849792	A1	middle	M5e	S1	M4	135.27			decay	Probable		marginal	2.0E+30	2.8E+29	small, cons., possible red wing

Table B.2.: (Continuation) Detected flaring spectra. A detailed description of the content is given at the begin of this chapter.

RA deg	DEC deg	Search Method	SNR BIN	Spec. Type Literature	Spec. Type Source	Spec.Type SDSS	Distance pc	Distance Source	Quiet flag	Flare evol. estimation	Consideration Flag	In Hilton et al. 2010	Platequality	Ha energy erg	error erg	Comments
358.334747	0.270599	A1	middle	M4e	S1	M4	245.948			decay	Yes	Yes	good	2.0E+31	1.1E+30	small, cons.
18.762882	-1.079139	A1	middle	M6e	S1	M5	53.875			decay	Yes		good	3.1E+29	1.0E+29	small, cons.
169.278885	10.973529	A1	middle	M5	SDSS	M5	103.851		2	p. rise	Yes		good	9.0E+29	2.2E+29	small
65.415199	26.820499	A1	middle	M6	S10	M8	166.309		1	rise	Yes		bad	2.9E+31	1.1E+30	small, cons., red wings enhanced, CME?
176.086655	39.111515	A1	middle	M6e	S1	M5	111.271			p. rise	Yes		marginal	3.7E+30	4.3E+29	small, red wing absorption
180.389786	40.779339	A1	middle	M7e	S1	M7	27.6849			rise	Yes	Yes	marginal	8.4E+29	2.9E+28	middle, cons., hb wings enhanced
193.302048	40.566845	A1	middle	M7e	S1	M7	21.2155			decay	Yes	Yes	good	1.6E+29	1.5E+28	small, cons., ha red wing enhancements
171.081482	39.804825	A1	middle	M6e	S1	M5	63.486		2	rise	Yes		good	1.6E+29	3.2E+28	middle, cons.
183.986725	32.217255	A1	middle	M5e	S1	M4	316.716			diff. activity	Yes		good	8.9E+30	1.7E+30	small, line asymmetries
178.316254	35.110172	A1	middle	M5e	S1	M4	106.598			rise	Probable	Yes	good	2.1E+30	2.4E+29	small, cons., red wing+far blue wing, CME?
243.155914	16.765554	A1	middle	M4e	SDSS	M4	225.332		1	p. rise	Yes		good	1.3E+31	1.2E+30	middle, ha blue wing, red wing absorptions
129.050232	18.735506	A1	middle	M5e	S1	M4	181.808			rise	Yes		good	6.0E+30	5.8E+29	big, cons., wings enhanced
136.895126	20.606697	A1	middle	M5e	S1	M4	134.969			rise	Yes		good	1.1E+30	2.1E+29	small, cons.
152.648697	21.931276	A1	middle	M6e	S1	M6	90.3514			decay	Yes		good	2.9E+30	2.0E+29	middle, cons., ha blue wing enhancements
156.367157	22.506145	A1	middle	M7e	S1	M6	53.2677		1	diff. activity	Yes		good	4.2E+29	3.3E+28	middle
221.463104	20.943859	A1	middle	M6e	S1	M6	57.2856			evolution	Yes		good	5.9E+29	6.7E+28	small, cons., hb wings
246.471909	17.956699	A1	middle	M5e	S1	M5	95.6636			evolution	Yes		good	2.1E+30	3.1E+29	small
138.812164	32.875816	A2	middle	M6e	S1	M6	60.1667			evolution	Yes		good	6.8E+29	8.7E+28	small
217.630417	57.172825	R	middle	M6e	S1	M6	54.3475			diff. activity	Yes	Yes	good	6.4E+29	7.6E+28	mini or nothing
255.809235	59.179905	A1	low	M7e	S1	M7	30.5983		1	rise	Yes		marginal	5.8E+29	1.9E+28	big
119.294991	42.948811	A1	low	M8e	S1	M7	116.163			rise	Yes	Yes	good	2.0E+30	1.7E+29	small, cons., red wings all balmer lines, CME?
147.111221	58.435368	A1	low	M6e	S1	M5	69.5217		1	diff. activity	Yes		marginal	5.3E+29	8.9E+28	small
213.870972	65.654877	A1	low	M7e	S1	M6	64.5	D2		evolution	Yes		good	1.5E+30	7.5E+28	middle, cons.
209.801086	1.975816	A1	low	M6e	S1	M5	66.1	D2		evolution	Yes		good	3.9E+29	8.6E+28	small, cons., high noise
144.389587	55.568310	A1	low	M6e	S1	M6	128.422			diff. activity	Probable		good	1.4E+30	1.8E+29	small, high noise
163.593353	5.628249	A1	low	M6e	S1	M6	86.5981			evolution	Yes		marginal	8.2E+29	6.9E+28	small, cons.
211.050232	4.048353	A1	low	M7e	S1	M6	72.1116			evolution	Yes	Yes	good	8.6E+29	6.9E+28	middle, cons., hb blue wing, ha wings
231.068893	60.044956	A1	low	M6e	S1	M6	117.661		1	diff. activity	Yes		good	1.4E+30	1.3E+29	middle
240.345276	51.896629	A1	low	M7e	S1	M6	85.7104			evolution	Yes	Yes	good	1.1E+30	8.4E+28	small, cons.
348.747528	-0.843476	A1	low	M6e	S1	M6	68.637			p. rise	Yes		good	7.0E+29	6.2E+28	middle, high noise
0.525718	1.260061	A1	low	M9e	S1	M8	20.81			unclear	Yes		good	3.6E+28	6.1E+27	small, cons., blue wing in ha hb hg, CME?
38.229469	0.562897	A1	low	M6e	S1	M6	126.355			evolution	Yes		marginal	1.9E+30	1.8E+29	small, high noise
114.812012	31.094975	A1	low	M6e	S1	M6	146.013			p. rise	Yes	Yes	good	2.5E+30	2.0E+29	middle, cons., new emission line
152.127136	59.292072	A1	low	M7e	S1	M7	44.7616			rise	Yes		bad	4.4E+29	4.4E+28	small, cons.
337.894928	0.454967	A1	low	M5e	S1	M5	96.6025		1	rise	Yes		good	1.5E+30	1.9E+29	small, many datapoints
12.247124	-0.526463	A1	low	M4e	S1	M4	195.764		1	diff. activity	Yes		marginal	3.7E+30	4.1E+29	middle, high noise
85.252243	0.791076	A1	low	M7e	S1	M6	184.713			decay	Probable		bad	1.4E+31	1.1E+30	middle
127.088547	27.709970	A1	low	M7e	S1	M6	45.2	D2		unclear	Yes		good	6.2E+29	5.1E+28	small, cons., wings in hb, poss. blue wing ha
138.911804	9.041699	A1	low	M4e	S1	M5	290.326		2	diff. activity	Probable	Yes	marginal	8.9E+31	3.3E+30	middle, line shift, possible enhanced
144.289124	10.437662	A1	low	M7e	S1	M6			1	diff. activity	Yes		good	0.0E+00	0.0E+00	middle, ha wings enhanced
52.993279	1.073068	A1	low	M4e	S1	M4	197.266			p. decay	Yes		good	6.9E+30	7.0E+29	middle, ha poss. red and blue wing cme like
234.079758	33.087532	A1	low	M7e	S1	M7	49.1807		2	decay	Probable	Yes	good	1.5E+29	2.2E+28	small, cons.
142.195221	34.326958	A1	low	M6e	S1	M6	74	D2	1	rise	Yes		marginal	4.4E+29	8.7E+28	small, cons.
180.587311	7.721731	A1	low	M6e	S1	M6	99.3009			decay	Yes		good	8.2E+29	1.8E+29	small, cons.
134.643127	25.270395	A1	low	M6e	S1	M6	78.0439		2	p. decay	Yes		good	4.6E+29	9.6E+28	small
29.342381	-0.432820	A1	low	M3e	S1	M2	444.306			p. rise	Yes		marginal	8.2E+30	2.1E+30	small, cons., new em. line, high noise, binary?
116.117882	19.265205	A1	low	M3e	S1	M2	429.387			unclear	M?		good	3.6E+31	1.9E+30	big, line shifts, maybe data problem, wings?
151.702667	26.765388	A1	low	M2e	S1	M1	250.288		1	p. rise	Yes		marginal	8.2E+30	5.4E+29	big, new emission line, high noise
123.095490	7.953677	A1	low	M6e	S1	M5	65.4759			evolution	Yes		good	4.3E+30	1.7E+29	middle, cons., shows evolution, wings enh.
230.153885	15.970867	A1	low	M7e	S1	M6	94.758			evolution	Yes		good	7.3E+29	1.6E+29	small, cons.
216.633057	9.272541	A1	low	M4e + DA	S3	M4	492.878		1	rise	Yes		good	3.9E+31	3.4E+30	middle, cons., high noise
33.471043	-0.005992	A2	low	M5	S1	M5	101.94			p. decay	Yes		good	1.1E+30	1.5E+29	small, new hb emission line
13.718028	0.528993	A2	low	M6e	S1	M5	109.851		2	rise	Yes	Yes	good	2.1E+30	1.8E+29	middle, cons.
156.391510	43.081554	A2	low	M6e	S1	M5	123.897		2	diff. activity	Yes		good	6.5E+29	1.3E+29	small
214.020264	32.288380	A2	low	M6e	S1	M5	74.8744		2	rise	Yes		good	2.2E+29	3.9E+28	small
6.851390	15.088673	E	low	M6e	S1	M6	108.789			rise	Yes		good	1.4E+30	1.3E+29	flaring
212.913757	60.413143	E	low	M7e	S1	M6	50.9391			evolution	Yes		good	5.3E+29	8.1E+28	slow
181.391479	3.970664	E	low	M7e	S1	M6	88.5779			decay	Yes		good	1.1E+30	1.2E+29	small
130.798233	35.319798	R	low	M7e	S1	M6	48.4489			decay	Yes	Yes	good	6.5E+28	2.5E+28	mini, cons., wings enhanced
148.586777	34.446220	R	low	M7e	S1	M6	94.8011			rise	Yes	Yes	good	5.8E+29	9.8E+28	mini, cons.

Table B.3.: (Continuation) Detected flaring spectra. A detailed description of the content is given at the begin of this chapter.

RA deg	DEC deg	Search Method	SNR BIN	Spec. Type Literature	Spec. Type Source	Spec.Type SDSS	Distance pc	Distance Source	Quiet flag	Flare evol. estimation	Consideration Flag	In Hilton et al. 2010	Platequality	Ha energy erg	error erg	Comments
247.065613	0.800828	A1	worst	M7e	S1	M7	71.1339			evolution	Yes		good	7.6E+29	5.9E+28	middle, cons., new hb emission line
48.996452	0.467583	A1	worst	M7e	S1	M6	331.29			p. decay	Probable		good	3.9E+30	8.9E+29	middle, cons., new hb emission line
35.959919	-9.251684	A1	worst	M9e	S1	M7	95.1683		1	diff. activity	Probable		good	1.4E+30	8.4E+28	middle, new emission line
53.721382	-7.317794	A1	worst	M6e	S1	M6	181.703			p. rise	Yes	Yes	good	9.8E+30	2.5E+29	big,cons.,new hb em.line,all red wings,cont. em?
138.121643	2.133469	A1	worst	M9	S11	M9			1	rise	Yes		good	0.0E+00	0.0E+00	big, cons., new emission lines
142.582779	-0.010675	A1	worst	M6e	S1	M6	357.82			p. decay	Probable		good	1.7E+31	1.2E+30	small, cons., normalization problem
136.702347	57.413158	A1	worst	M7e	S1	M6	94.8902			decay	Yes		good	4.5E+29	6.6E+28	middle, cons.
153.451675	2.272996	A1	worst	M7e	S1	M6	245.652		2	evolution	Yes		good	7.0E+30	5.6E+29	middle, cons., high noise
115.680260	35.390343	A1	worst	M6e	S1	M6	95.8699		1	diff. activity	Yes	Yes	marginal	5.4E+30	1.7E+29	middle, cons., many datapoints
118.834488	36.845558	A1	worst	M8e	S1	M8	77.6741			evolution	Probable		good	2.1E+29	5.5E+28	small, cons., high noise
132.202164	2.632245	A1	worst	M6	S1	M6	176.386		1	diff. activity	Probable		marginal	1.2E+31	4.4E+29	middle, cons., high noise, new emission line
197.737473	64.996262	A1	worst	M6e	S1	M6	462.235			unclear	Probable		good	7.3E+30	2.0E+30	small, cons., high noise
3.028603	-10.459081	A1	worst	M5e	S1	M5	104.991		2	p. decay	Probable		good	1.3E+30	1.3E+29	middle, high noise
353.034760	-0.951729	A1	worst	M7e	S1	M7	95.4563		1	diff. activity	Yes		good	1.4E+30	7.4E+28	big in ha
145.080627	54.030544	A1	worst	M6	S1	M5	227.962			rise	Yes		marginal	9.1E+30	5.6E+29	small, cons., high noise, new emission line
202.928467	62.168243	A1	worst	M6e	S1	M5	174.146			decay	Yes		good	1.3E+30	2.6E+29	small, cons., high noise
243.836594	43.501934	A1	worst	M8e	S1	M8	74.1757			p. rise	Probable		good	3.5E+29	4.5E+28	small, cons., high noise
132.950806	41.579262	A1	worst	M7e	S1	M7	46.1031			evolution	Probable		marginal	6.5E+29	4.8E+28	middle, cons., high noise
142.687454	46.293781	A1	worst	M6e	S1	M6	154.505			decay	Yes		marginal	3.2E+30	2.8E+29	small, cons., high noise
195.650879	6.030006	A1	worst	M7	S1	M7	82.6808			decay	Yes	Yes	marginal	2.5E+31	3.5E+29	big, cons., decay, huge emission line variation
157.092865	6.980092	A1	worst	M6e	S1	M5	111.085			decay	Yes		marginal	1.6E+30	1.4E+29	small, cons., high noise
247.801147	32.453171	A1	worst	M8e	S1	M8	29.653			decay	Yes		marginal	1.1E+29	1.1E+28	small, cons., high noise
24.024479	-1.129921	A1	worst	M6	S1	M6	151.499		1	diff. activity	Yes	Yes	marginal	3.8E+31	5.4E+29	big
353.101593	-0.840395	A1	worst	M9e	S1	M7	40.4722		1	p. decay	Yes		marginal	4.1E+29	1.9E+28	middle, new hb emission line
13.541390	-0.154456	A1	worst	M6e	S1	M6	123.716			rise	Yes		good	3.1E+30	2.8E+29	small, cons., high noise
129.566055	4.444690	A1	worst	M6e	S1	M6	184.505			evolution	Probable		good	1.5E+30	2.4E+29	small, cons., high noise
135.834137	36.697166	A1	worst	M7e	S1	M7	71.3781			decay	Yes		good	5.8E+29	5.4E+28	small, cons., high noise
152.750870	42.750820	A1	worst	M8e	S1	M8	35.3003			rise	Probable		marginal	2.0E+28	7.4E+27	small, cons., high noise
91.013451	-0.054071	A1	worst	M5	SDSS	M5	531.745			evolution	Yes		bad	1.2E+32	5.8E+30	middle, new emission line, high noise
141.033203	36.027294	A1	worst	M9	S1	M8	95.2553			evolution	Yes		good	2.2E+30	8.7E+28	middle, cons., new emission line, high noise
129.774246	6.915517	A1	worst	M5e	S1	M5	114.185		2	evolution	Yes	Yes	good	2.0E+30	1.3E+29	one middle, cons., high noise
188.085327	57.651936	A1	worst	M6e	S1	M6	197.258			rise	Probable		marginal	3.1E+30	3.8E+29	middle, cons., high noise
212.351959	43.966244	A1	worst	M7e	S1	M6	82.6207			p. decay	Probable		good	2.6E+29	4.4E+28	small
321.284088	0.086523	A1	worst	M8e	S1	M7	98.9335		1	p. rise	Yes		marginal	3.1E+30	1.7E+29	middle
135.662445	30.311211	A1	worst	M9	S1	M8	83.12369	D4		decay	Probable		good	9.2E+29	7.2E+28	small, cons., new emission line
203.732788	51.467476	A1	worst	M6e	S1	M5	163.343			p. rise	Probable		good	8.4E+29	1.7E+29	small
233.714584	41.826950	A1	worst	M7	S1	M6	250.777			evolution	Probable		good	3.0E+30	4.3E+29	one small, possible ha red wings
247.007782	31.288391	A1	worst	M8e	S1	M7	65.9417			rise	Probable		good	1.1E+30	6.0E+28	middle
125.496231	7.266244	A1	worst	M7e	S1	M7	119.53			evolution	Yes		good	1.2E+30	1.5E+29	small
196.079315	15.214287	A1	worst	M5e	S2	M5	212.026			decay	Yes	Yes	good	1.2E+31	5.7E+29	middle
193.602524	36.952114	A1	worst	M7e	S1	M7	67.351		1	diff. activity	Yes		good	9.2E+29	5.1E+28	small
235.920334	18.459101	A1	worst	M9	S1	M9	61.7185		2	p. rise	Probable		good	5.7E+29	3.0E+28	middle, weird hb
245.843933	14.709205	A1	worst	M8e	S1	M7	79.2305			decay	Probable		good	1.4E+30	6.1E+28	middle
242.102951	19.963179	A1	worst	M9e	S1	M9	27.097			rise	Probable		good	1.9E+29	8.9E+27	middle
170.398376	28.616863	A1	worst	M6e	S1	M5	412.082		2	evolution	Yes		good	6.8E+30	1.0E+30	small
173.717422	26.991867	A1	worst	M7e	S1	M6	162.8		1	evolution	Probable		good	5.2E+30	2.7E+29	middle
175.482635	30.132616	A1	worst	M7e	S1	M7	120.437			p. decay	Probable		good	4.4E+29	8.7E+28	small
120.245193	13.169741	A1	worst	M7	S1	M6	280.82			decay	Yes		good	7.8E+30	5.7E+29	small
129.006653	19.958700	A1	worst	M6e	S1	M5	192.585			decay	Yes		good	4.3E+30	5.4E+29	small
129.979538	20.938843	A1	worst	M9e	S1	M8	48.0432			evolution	Yes		good	3.4E+29	1.9E+28	middle
32.357277	6.703871	A1	worst	M3.5 + DA	S12	M4	412.082		2	evolution	Yes		good	4.9E+31	2.5E+30	middle
15.797990	-0.738078	A1	worst	M9e	S1	M9	35.8409		1	evolution	Yes		good	2.0E+29	1.1E+28	small, many datapoints
162.955521	26.190184	A1	worst	M4e	S1	M4	254.57			rise	Probable		good	5.6E+30	7.6E+29	small
164.008224	28.585464	A1	worst	M7e	S1	M5	111.908		2	rise	Yes		good	9.0E+30	2.3E+29	big
164.008224	28.585464	A1	worst	M7e	S1	M6	111.908			decay	Yes		good	3.1E+29	6.8E+28	small, same star as before
155.143417	22.113638	A1	worst	M7e	S1	M6	116.267		2	decay	Yes		marginal	3.2E+30	1.9E+29	middle
144.121552	16.522655	A1	worst	M6e	S1	M6	120.301			decay	Yes		good	1.3E+30	1.2E+29	small
151.333435	15.661367	A1	worst	M8	S1	M9	52.6854		2	diff. activity	Yes		good	5.3E+29	2.2E+28	middle
185.422562	21.683882	A1	worst	M9	S1	M8	102.421			evolution	Probable		good	1.1E+30	1.1E+29	small
191.523544	24.107292	A1	worst	M7e	S1	M6	68	D2	2	diff. activity	Yes		good	1.0E+30	7.3E+28	middle

Table B.4.: (Continuation) Detected flaring spectra. A detailed description of the content is given at the begin of this chapter.

RA deg	DEC deg	Search Method	SNR BIN	Spec. Type Literature	Spec. Type Source	Spec.Type SDSS	Distance pc	Distance Source	Quiet flag	Flare evol. estimation	Consideration Flag	In Hilton et al. 2010	Platequality	Ha energy erg	error erg	Comments
205.795212	24.993681	A1	worst	M6e	S1	M6	74.2528			diff. activity	Yes		good	1.6E+30	7.7E+28	middle or small
234.784363	18.069933	A1	worst	M9	S1	M9	89.2092			rise	Yes		good	1.2E+30	5.9E+28	middle
25.432005	-9.636590	A1	worst	M3.5 + DB	S12	M3	322.227		1	diff. activity	Yes		good	1.5E+31	1.5E+30	small, many datapoints
23.421482	-10.140172	A1	worst	M6e	S1	M7	155.989		2	decay	Probable		good	1.7E+30	2.3E+29	small, many datapoints
21.136980	-10.328443	A1	worst	M5e	S1	M5	117.936		1	p. rise	Yes		good	1.5E+30	1.2E+29	small, many datapoints
248.948273	27.373207	A1	worst	M9e	S1	M8	42.0713		2	rise	Yes		good	3.8E+29	1.9E+28	big
243.172134	17.507805	A1	worst	M8e	S1	M7	70.6739		2	rise	Yes		good	3.6E+29	2.5E+28	big
194.476898	3.550146	A2	worst	M6e	S1	M6	103.04		2	rise	Yes	Yes	good	4.1E+30	1.2E+29	big, wings, continuum emission
197.650009	2.003429	A2	worst	M7	S1	M7	73.9169		2	diff. activity	Probable		marginal	6.8E+29	#WERT!	
120.126373	39.861370	A2	worst	M7e	S1	M6	103.103			p. decay	Probable		good	3.4E+29	6.9E+28	
149.166458	5.049810	A2	worst	M6e	S1	M6	185.5	D2	2	rise	Yes		good	1.5E+30	1.7E+29	new emission line cons.
225.564941	54.986523	A2	worst	M6e	S1	M5	291.622		1	diff. activity	Yes		good	1.0E+31	5.3E+29	new emission line
118.056030	27.778877	A2	worst	M7e	S1	M6	104.63		1	rise	Yes	Yes	good	2.0E+30	1.4E+29	new emission line
123.969879	32.284924	A2	worst	M6e	S1	M6	137.811		2	rise	Yes	Yes	good	2.0E+30	1.1E+29	big
140.376541	48.078518	A2	worst	M6	S1	M5	131.392		2	decay	Yes		marginal	1.9E+30	2.6E+29	
230.633408	-1.351518	A2	worst	M7e	S1	M6	385.267			diff. activity	Probable		good	1.1E+31	1.0E+30	middle
156.272491	57.844460	A2	worst	M6e	S1	M6	104.133		1	rise	Yes	Yes	marginal	1.6E+30	1.2E+29	middle
136.280792	41.828140	A2	worst	M7	S1	M6	269.447		1	evolution	Probable		good	4.9E+30	5.7E+29	middle
144.749054	44.611221	A2	worst	M6	S1	M6	232.159		2	rise	Probable		good	3.4E+30	2.8E+29	middle
215.586517	53.885887	A2	worst	M6e	S1	M6	105.877		2	diff. activity	Yes		good	1.6E+30	1.5E+29	middle
224.673447	35.650471	A2	worst	M9	S1	M8	112.905		2	p. decay	Probable		good	3.7E+29	1.1E+29	small
243.384506	29.696947	A2	worst	M6e	S1	M6	110.386		2	decay	Yes		marginal	1.0E+30	1.0E+29	middle
180.333466	15.000701	A2	worst	M7e	S1	M6	120.995		2	rise	Yes		good	7.2E+29	1.0E+29	small
141.807541	30.691338	A2	worst	M7e	S1	M7	149.245			rise	Probable		good	1.0E+30	1.5E+29	small
196.457352	37.702522	A2	worst	M7e	S1	M6	212.553			evolution	Probable		marginal	2.4E+30	3.8E+29	middle, evolution
244.661240	15.636463	A2	worst	M6e	S1	M5	180.58		1	diff. activity	Probable		good	1.9E+30	2.8E+29	
120.508202	12.395294	A2	worst	M9e	S1	M8	45.7796			evolution	Probable		good	1.8E+29	3.7E+28	small, evolution
135.182648	20.928860	A2	worst	M6	S1	M6	167.926		1	diff. activity	Yes		marginal	1.9E+31	3.3E+29	big
248.558273	11.930343	A2	worst	M7e	S1	M7	65.99327	D4		evolution	Probable		good	5.9E+29	4.5E+28	small or middle
216.631851	15.950253	A2	worst	M9	S1	M9	29.8443			evolution	Probable		good	5.1E+28	7.2E+27	ha red wing
216.631851	15.950253	A2	worst	M9	S1	M9	29.8443		1	rise	Yes		good	1.7E+29	8.3E+27	
219.604477	39.638771	R	worst	M7e	S1	M5	131.125		2	rise	Yes	Yes	marginal	1.3E+31	5.5E+29	middle, cons.
184.37228	0.592402	R	worst	M9e	S1	M8	29.6888		1	decay	Probable	Yes	good	7.5E+28	9.7E+27	
328.729919	1.237362	A1	high	M0e	S13	K5	1452.43		2	diff. activity	Probable		good	2.3E+33	3.6E+32	small, shift
10.402094	0.187976	A1	high	K7	SDSS	K7	623.752			rise	Yes		good	2.3E+32	4.4E+31	small
343.805786	0.974758	A1	high	K3	SDSS	K3	647.333		1	evolution	Yes		good	1.4E+33	1.5E+32	middle, line shift
126.178383	38.568233	A1	high	dKs7.0	S14	K7	629.525		1	evolution	Yes		good	8.2E+32	4.5E+31	big, evolution
1.250924	-4.541332	A2	high	M0Ve	S15	K5	501.681			evolution	Probable		good	1.9E+32	4.2E+31	line shift
143.34863	28.740053	A2	high	dKp7.0	S14	K7	991.277		1	evolution	Yes		good	1.5E+33	1.8E+32	new emission lines

Table B.5.: (Continuation) Detected flaring spectra. A detailed description of the content is given at the begin of this chapter.

Bibliography

Abolfathi, Bela et al. (2018). "The Fourteenth Data Release of the Sloan Digital Sky Survey: First Spectroscopic Data from the Extended Baryon Oscillation Spectroscopic Survey and from the Second Phase of the Apache Point Observatory Galactic Evolution Experiment." In: *ApJS* 235.2, 42, p. 42. DOI: 10.3847/1538-4365/aa9e8a. arXiv: 1707.09322 [astro-ph.GA] (cit. on p. 25).

Ahn, Christopher P. et al. (2012). "The Ninth Data Release of the Sloan Digital Sky Survey: First Spectroscopic Data from the SDSS-III Baryon Oscillation Spectroscopic Survey." In: *APJS* 203.2, 21, p. 21. DOI: 10.1088/0067-0049/203/2/21. arXiv: 1207.7137 [astro-ph.IM] (cit. on p. 25).

Alam, Shadab et al. (2015). "The Eleventh and Twelfth Data Releases of the Sloan Digital Sky Survey: Final Data from SDSS-III." In: *ApJS* 219.1, 12, p. 12. DOI: 10.1088/0067-0049/219/1/12. arXiv: 1501.00963 [astro-ph.IM] (cit. on p. 43).

Alvarado-Gómez, Julián D. et al. (2018). "Suppression of Coronal Mass Ejections in Active Stars by an Overlying Large-scale Magnetic Field: A Numerical Study." In: *APJ* 862.2, 93, p. 93. DOI: 10.3847/1538-4357/aacb7f. arXiv: 1806.02828 [astro-ph.SR] (cit. on p. 78).

Antia, H. M., A. Bhatnagar, and P. Ulmschneider (2003). *Lectures on Solar Physics*. Vol. 619 (cit. on p. 13).

Asai, Ayumi et al. (2012). "A Study on Red Asymmetry of Hα Flare Ribbons Using a Narrowband Filtergram in the 2001 April 10 Solar Flare." In: *PASJ* 64, 20, p. 20. DOI: 10.1093/pasj/64.1.20. arXiv: 1112.5912 [astro-ph.SR] (cit. on p. 79).

Aschwanden, Markus J. (2019). *New Millennium Solar Physics*. Vol. 458. DOI: 10.1007/978-3-030-13956-8 (cit. on pp. 13, 16).

Bailer-Jones, C. A. L. et al. (2018). "Estimating Distance from Parallaxes. IV. Distances to 1.33 Billion Stars in Gaia Data Release 2." In: *AJ* 156.2, 58, p. 58. DOI: 10.3847/1538-3881/aacb21. arXiv: 1804.10121 [astro-ph.SR] (cit. on pp. 30, 52).

Balona, L. A. (2015). "Flare stars across the H-R diagram." In: *MNRAS* 447.3, pp. 2714–2725. DOI: 10.1093/mnras/stu2651 (cit. on pp. 22, 75).

Barnes, J. R. et al. (2005). "The dependence of differential rotation on temperature and rotation." In: *MNRAS* 357.1, pp. L1–L5. DOI: 10.1111/j.1745-3933.2005.08587.x. arXiv: astro-ph/0410575 [astro-ph] (cit. on p. 20).

Becker, A. C. et al. (2011). "Periodic Variability of Low-mass Stars in Sloan Digital Sky Survey Stripe 82." In: *APJ* 731.1, 17, p. 17. DOI: 10.1088/0004-637X/731/1/17. arXiv: 1102.1387 [astro-ph.SR] (cit. on p. 52).

Bell, Keaton J. et al. (2012). "Hα Emission Variability in Active M Dwarfs." In: *PASP* 124.911, p. 14. DOI: 10.1086/664024. arXiv: 1112.1411 [astro-ph.SR] (cit. on p. 3).

Berdyugina, Svetlana V. (2005). "Starspots: A Key to the Stellar Dynamo." In: *Living Reviews in Solar Physics* 2.1, p. 8. ISSN: 1614-4961. DOI: 10.12942/lrsp-2005-8. URL: https://doi.org/10.12942/lrsp-2005-8 (cit. on p. 19).

Bonanno, A., H. Schlattl, and L. Paternò (2002). "The age of the Sun and the relativistic corrections in the EOS." In: *AAP* 390, pp. 1115–1118. DOI: 10.1051/0004-6361:20020749. arXiv: astro-ph/0204331 [astro-ph] (cit. on p. 5).

Briceño, César et al. (2019). "The CIDA Variability Survey of Orion OB1. II. Demographics of the Young, Low-mass Stellar Populations." In: *AJ* 157.2, 85, p. 85. DOI: 10.3847/1538-3881/aaf79b (cit. on p. 84).

Butler, C. J., M. Rodono, and B. H. Foing (1988). "A correlation between Balmer and soft X-ray emission from stellar andsolar flares." In: *AAP* 206, pp. L1–L4 (cit. on p. 69).

Cook, N. J. et al. (2016). "A method for selecting M dwarfs with an increased likelihood of unresolved ultracool companionship." In: *MNRAS* 457.2, pp. 2192–2208. DOI: 10.1093/mnras/stw061. arXiv: 1601.03402 [astro-ph.SR] (cit. on p. 84).

Davenport, James R. A. (2016). "The Kepler Catalog of Stellar Flares." In: *APJ* 829.1, 23, p. 23. DOI: 10.3847/0004-637X/829/1/23. arXiv: 1607.03494 [astro-ph.SR] (cit. on pp. 22, 75).

de Boer, Klaas and Wilhelm Seggewiss (2008). *Stars and Stellar Evolution* (cit. on p. 19).

Debes, John H. (2006). "Measuring M Dwarf Winds with DAZ White Dwarfs." In: *APJ* 652.1, pp. 636–642. DOI: 10.1086/508132. arXiv: astro-ph/0608030 [astro-ph] (cit. on p. 21).

Den, O. E. and G. I. Kornienko (1993). "Mass ejection during the flare of 12 March 1989 based on Hα filtergrams and spectrograms." In: *Astronomy Reports* 37.1, pp. 76–82 (cit. on p. 3).

Ding, M. D. et al. (2003). "Hα and Hard X-Ray Observations of a Two-Ribbon Flare Associated with a Filament Eruption." In: *APJ* 598.1, pp. 683–688. DOI: 10.1086/378877. arXiv: astro-ph/0308085 [astro-ph] (cit. on p. 3).

Dissauer, K. et al. (2018). "On the Detection of Coronal Dimmings and the Extraction of Their Characteristic Properties." In: *APJ* 855.2, 137, p. 137. DOI: 10.3847/1538-4357/aaadb5. arXiv: 1802.03185 [astro-ph.SR] (cit. on pp. 15, 24).

Drake, A. J., M. J. Graham, et al. (2014). "The Catalina Surveys Periodic Variable Star Catalog." In: *APJS* 213.1, 9, p. 9. DOI: 10.1088/0067-0049/213/1/9. arXiv: 1405.4290 [astro-ph.SR] (cit. on p. 52).

Drake, Jeremy J., Ofer Cohen, et al. (2013). "Implications of Mass and Energy Loss due to Coronal Mass Ejections on Magnetically Active Stars." In: *APJ* 764.2, 170, p. 170. DOI: 10.1088/0004-637X/764/2/170. arXiv: 1302.1136 [astro-ph.SR] (cit. on p. 2).

Favata, F. and J. H. M. M. Schmitt (1999). "Spectroscopic analysis of a super-hot giant flare observed on Algol by BeppoSAX on 30 August 1997." In: *AAP* 350, pp. 900–916. arXiv: astro-ph/9909041 [astro-ph] (cit. on p. 2).

Fichtinger, Bibiana et al. (2017). "Radio emission and mass loss rate limits of four young solar-type stars." In: *AAP* 599, A127, A127. DOI: 10.1051/0004-6361/201629886. arXiv: 1702.08393 [astro-ph.SR] (cit. on p. 21).

Fletcher, L. et al. (2011). "An Observational Overview of Solar Flares." In: *SSR* 159.1-4, pp. 19–106. DOI: 10.1007/s11214-010-9701-8. arXiv: 1109.5932 [astro-ph.SR] (cit. on p. 13).

Foukal, Peter V. (2004). *Solar Astrophysics, 2nd, Revised Edition* (cit. on pp. 13, 16).

Fuhrmeister, B. and J. H. M. M. Schmitt (2004). "Detection and high-resolution spectroscopy of a huge flare on the old M 9 dwarf DENIS 104814.7-395606.1." In: *AAP* 420, pp. 1079–1085. DOI: 10.1051/0004-6361:20035644. arXiv: astro-ph/0403617 [astro-ph] (cit. on p. 2).

Gaia Collaboration et al. (2018). "Gaia Data Release 2 - Summary of the contents and survey properties." In: *A&A* 616, A1. DOI: 10.1051/0004-6361/201833051. URL: https://doi.org/10.1051/0004-6361/201833051 (cit. on pp. 3, 30, 43, 46, 71, 84).

Gopalswamy, N. et al. (2010). "A Catalog of Halo Coronal Mass Ejections from SOHO." In: *Sun and Geosphere* 5.1, pp. 7–16 (cit. on p. 14).

Graffagnino, V. G., D. Wonnacott, and S. Schaeidt (1995). "HR 5110 superflare: an interbinary flare identified?" In: *MNRAS* 275.1, pp. 129–142. DOI: 10.1093/mnras/275.1.129 (cit. on p. 22).

Güdel, Manuel (2002). "Stellar Radio Astronomy: Probing Stellar Atmospheres from Protostars to Giants." In: *ARAA* 40, pp. 217–261. DOI: 10.1146/annurev.astro.40.060401.093806. arXiv: astro-ph/0206436 [astro-ph] (cit. on p. 22).

Güdel, Manuel (2004). "X-ray astronomy of stellar coronae." In: *AAPR* 12.2-3, pp. 71–237. DOI: 10.1007/s00159-004-0023-2. arXiv: astro-ph/0406661 [astro-ph] (cit. on p. 22).

Guenther, E. W. and J. P. Emerson (1997). "Spectrophotometry of flares and short time scale variations in weak line, and classical T Tauri stars in Chamaeleon." In: *AAP* 321, pp. 803–810 (cit. on p. 2).

Guieu, S. et al. (2006). "Seventeen new very low-mass members in Taurus. The brown dwarf deficit revisited." In: *AAP* 446.2, pp. 485–500. DOI: 10.1051/0004-6361:20053493. arXiv: astro-ph/0509317 [astro-ph] (cit. on p. 84).

Gunn, A. G. et al. (1994). "High-velocity evaporation during a flare on AT Microscopii." In: *AAP* 285, pp. 489–496 (cit. on pp. 2, 79).

Günther, Maximilian N. et al. (2019). "Stellar Flares from the First Tess Data Release: Exploring a New Sample of M-dwarfs." In: *arXiv e-prints*, arXiv:1901.00443, arXiv:1901.00443. arXiv: 1901.00443 [astro-ph.EP] (cit. on p. 22).

Habets, G. M. H. J. and J. R. W. Heintze (1981). "Empirical bolometric corrections for the main-sequence." In: *AAPS* 46, pp. 193–237 (cit. on p. 17).

Haisch, B. M., J. L. Linsky, et al. (1983). "Coordinated Einstein and IUE observations of a disparitions brusques type flare event and quiescent emission from Proxima Centauri." In: *APJ* 267, pp. 280–290. DOI: 10.1086/160866 (cit. on p. 2).

Haisch, Bernhard, Keith T. Strong, and Marcello Rodono (1991). "Flares on the Sun and other stars." In: *ARAA* 29, pp. 275–324. DOI: 10.1146/annurev.aa.29.090191.001423 (cit. on pp. 21, 22).

Hanslmeier, A. et al. (2017). "Extreme Space Weather in Extra-Solar Systems - a Flare Alert Program." In: *Central European Astrophysical Bulletin* 41, pp. 67–78 (cit. on p. 80).

Heinze, A. N. et al. (2018). "A First Catalog of Variable Stars Measured by the Asteroid Terrestrial-impact Last Alert System (ATLAS)." In: *AJ* 156.5, 241, p. 241. DOI: 10.3847/1538-3881/aae47f. arXiv: 1804.02132 [astro-ph.SR] (cit. on p. 53).

Hilton, Eric J. et al. (2010). "M Dwarf Flares from Time-resolved Sloan Digital Sky Survey Spectra." In: *AJ* 140.5, pp. 1402–1413. DOI: 10.1088/0004-6256/140/5/1402. arXiv: 1009.1158 [astro-ph.SR] (cit. on pp. 3, 28, 30, 31, 37, 43, 73, 74, 76, 82–85).

Houdebine, E. R., B. H. Foing, and M. Rodono (1990). "Dynamics of flares on late-type dMe stars. I. Flare mass ejections and stellar evolution." In: *AAP* 238, p. 249 (cit. on pp. 2, 38, 68, 69).

Johnstone, C. P. et al. (2015). "Stellar winds on the main-sequence. I. Wind model." In: *AAP* 577, A27, A27. DOI: 10.1051/0004-6361/201425300. arXiv: 1503.06669 [astro-ph.SR] (cit. on p. 21).

Jones, David O. and Andrew A. West (2016). "A Catalog of GALEX Ultraviolet Emission from Spectroscopically Confirmed M Dwarfs." In: *APJ* 817.1, 1, p. 1. DOI: 10.3847/0004-637X/817/1/1. arXiv: 1509.03645 [astro-ph.SR] (cit. on p. 84).

Khodachenko, Maxim L. et al. (2007). "Coronal Mass Ejection (CME) Activity of Low Mass M Stars as An Important Factor for The Habitability of Terrestrial Exoplanets. I. CME Impact on Expected Magnetospheres of Earth-Like Exoplanets in Close-In Habitable Zones." In: *Astrobiology* 7.1, pp. 167–184. DOI: 10.1089/ast.2006.0127 (cit. on p. 1).

Kleinman, S. J. et al. (2013). "SDSS DR7 White Dwarf Catalog." In: *APJS* 204.1, 5, p. 5. DOI: 10.1088/0067-0049/204/1/5. arXiv: 1212.1222 [astro-ph.SR] (cit. on pp. 52, 84).

Kliem, B. and T. Török (2006). "Torus Instability." In: *PRL* 96.25, 255002, p. 255002. DOI: 10.1103/PhysRevLett.96.255002. arXiv: physics/0605217 [physics.plasm-ph] (cit. on p. 15).

Koenig, Xavier et al. (2015). "Spectroscopic Assessment of WISE-based Young Stellar Object Selection Near λ and σ Orionis." In: *AJ* 150.4, 100, p. 100. DOI: 10.1088/0004-6256/150/4/100. arXiv: 1506.05141 [astro-ph.GA] (cit. on p. 54).

Kowalski, Adam F., Suzanne L. Hawley, Eric J. Hilton, et al. (2009). "M Dwarfs in Sloan Digital Sky Survey Stripe 82: Photometric Light Curves and Flare Rate Analysis." In: *AJ* 138.2, pp. 633–648. DOI: 10.1088/0004-6256/138/2/633. arXiv: 0906.2030 [astro-ph.SR] (cit. on pp. 53, 75, 84).

Kowalski, Adam F., Suzanne L. Hawley, John P. Wisniewski, et al. (2013). "Time-resolved Properties and Global Trends in dMe Flares from Simultaneous Photometry and Spectra." In: *APJS* 207.1, 15, p. 15. DOI: 10.1088/0067-0049/207/1/15. arXiv: 1307.2099 [astro-ph.SR] (cit. on p. 22).

Kraus, Adam L. and Lynne A. Hillenbrand (2009). "The Coevality of Young Binary Systems." In: *APJ* 704.1, pp. 531–547. DOI: 10.1088/0004-637X/704/1/531. arXiv: 0909.0509 [astro-ph.SR] (cit. on p. 84).

Kruse, E. A. et al. (2010). "Chromospheric Variability in Sloan Digital Sky Survey M Dwarfs. II. Short-timescale Hα Variability." In: *APJ* 722.2, pp. 1352–1359. DOI: 10.1088/0004-637X/722/2/1352. arXiv: 0911.2712 [astro-ph.SR] (cit. on p. 3).

Lammer, Helmut, Manuel Güdel, et al. (2012). "Variability of solar/stellar activity and magnetic field and its influence on planetary atmosphere evolution." In: *Earth, Planets, and Space* 64.2, pp. 179–199. DOI: 10.5047/eps.2011.04.002 (cit. on p. 1).

Lammer, Helmut, Herbert I. M. Lichtenegger, et al. (2007). "Coronal Mass Ejection (CME) Activity of Low Mass M Stars as An Important Factor for The Habitability of Terrestrial Exoplanets. II. CME-Induced Ion Pick Up of Earth-like Exoplanets in Close-In Habitable Zones." In: *Astrobiology* 7.1, pp. 185–207. DOI: 10.1089/ast.2006.0128 (cit. on p. 1).

Lamy, P. L. et al. (2019). "Coronal Mass Ejections over Solar Cycles 23 and 24." In: *SSR* 215.5, 39, p. 39. DOI: 10.1007/s11214-019-0605-y (cit. on p. 15).

Leitzinger, Martin, Petra Odert, Robert Greimel, et al. (2014). "A search for flares and mass ejections on young late-type stars in the open cluster Blanco-1." In: *MNRAS* 443.1, pp. 898–910. DOI: 10.1093/mnras/stu1161. arXiv: 1406.2734 [astro-ph.SR] (cit. on pp. 69, 78).

Leitzinger, Martin, Petra Odert, I. Ribas, et al. (2011). "Search for indications of stellar mass ejections using FUV spectra." In: *AAP* 536, A62, A62. DOI: 10.1051/0004-6361/201015985 (cit. on pp. 2, 23).

Luhman, K. L. et al. (2017). "A Survey for New Members of the Taurus Star-forming Region with the Sloan Digital Sky Survey." In: *AJ* 153.1, 46, p. 46. DOI: 10.3847/1538-3881/153/1/46. arXiv: 1610.09412 [astro-ph.GA] (cit. on pp. 54, 84).

Maciel, Walter J (2014). *Stellar Winds: An Overview*. Springer, pp. 127–156 (cit. on pp. 12, 20, 21).

Magara, Tetsuya et al. (1996). "Numerical Simulation of Magnetic Reconnection in Eruptive Flares." In: *APJ* 466, p. 1054. DOI: 10.1086/177575 (cit. on pp. 13, 14).

Masson, S., S. K. Antiochos, and C. R. DeVore (2013). "A Model for the Escape of Solar-flare-accelerated Particles." In: *APJ* 771.2, 82, p. 82. DOI: 10.1088/0004-637X/771/2/82. arXiv: 1301.0654 [astro-ph.SR] (cit. on pp. 15, 16).

McGehee, Peregrine M. (2006). "The Southern Flanking Fields of the 25 Orionis Group." In: *AJ* 131.6, pp. 2959–2966. DOI: 10.1086/504156. arXiv: astro-ph/0603317 [astro-ph] (cit. on pp. 53, 84).

Meadows, A. J. (1978). *Stellar evolution* (cit. on p. 19).

Melis, C. et al. (2012). "Rapid disappearance of a warm, dusty circumstellar disk." In: *Nature* 487, pp. 74–76. DOI: 10.1038/nature11210. arXiv: 1207.1162 [astro-ph.SR] (cit. on p. 24).

Morgan, Dylan P. et al. (2012). "The Effects of Close Companions (and Rotation) on the Magnetic Activity of M Dwarfs." In: *AJ* 144.4, 93, p. 93. DOI: 10.1088/0004-6256/144/4/93. arXiv: 1205.6806 [astro-ph.SR] (cit. on p. 84).

Moschou, Sofia-Paraskevi et al. (2019). "The Stellar CME-Flare Relation: What Do Historic Observations Reveal?" In: *APJ* 877.2, 105, p. 105. DOI: 10.3847/1538-4357/ab1b37. arXiv: 1904.09598 [astro-ph.SR] (cit. on pp. 2, 23, 24).

Newton, Elisabeth R. et al. (2014). "Near-infrared Metallicities, Radial Velocities, and Spectral Types for 447 Nearby M Dwarfs." In: *AJ* 147.1, 20, p. 20. DOI: 10.1088/0004-6256/147/1/20. arXiv: 1310.1087 [astro-ph.SR] (cit. on p. 84).

Odert, Petra, Martin Leitzinger, E. W. Guenther, et al. (2019). "Stellar coronal mass ejections - II. Constraints from spectroscopic observations." In: *SUBMITTED TO MNRAS* (cit. on pp. 70, 71, 77, 78).

Odert, Petra, Martin Leitzinger, A. Hanslmeier, et al. (2017). "Stellar coronal mass ejections - I. Estimating occurrence frequencies and mass-loss rates." In: *MNRAS* 472.1, pp. 876–890. DOI: 10.1093/mnras/stx1969. arXiv: 1707.02165 [astro-ph.SR] (cit. on pp. 2, 78, 79).

Osten, Rachel A. and Scott J. Wolk (2017). "A Framework for Finding and Interpreting Stellar CMEs." In: *Living Around Active Stars*. Ed. by D. Nandy, A. Valio, and P. Petit. Vol. 328. IAU Symposium, pp. 243–251. DOI: 10.1017/S1743921317004252 (cit. on p. 24).

Pettersen, B. R. (1989). "A Review of Stellar Flares and Their Characteristics." In: *SOLPHYS* 121.1-2, pp. 299–312. DOI: 10.1007/BF00161702 (cit. on p. 21).

Pradhan, Anil K. and Sultana N. Nahar (2011). *Atomic Astrophysics and Spectroscopy* (cit. on pp. 6, 10).

Preibisch, T., R. Neuhaeuser, and J. M. Alcala (1995). "A giant X-ray flare on the young star P1724." In: *AAP* 304, p. L13 (cit. on p. 22).

Rebassa-Mansergas, A. et al. (2013). "White dwarf main-sequence binaries from SDSS DR 8: unveiling the cool white dwarf population." In: *MNRAS* 433.4, pp. 3398–3410. DOI: 10.1093/mnras/stt974. arXiv: 1306.0952 [astro-ph.SR] (cit. on p. 52).

Rutten, Robert J. (2003). *Radiative Transfer in Stellar Atmospheres* (cit. on p. 6).
Skiff, B. A. (2014). "VizieR Online Data Catalog: Catalogue of Stellar Spectral Classifications (Skiff, 2009-)." In: *VizieR Online Data Catalog*, B/mk, B/mk (cit. on pp. 27, 43, 50, 84).
Stassun, Keivan G. et al. (2018). "The TESS Input Catalog and Candidate Target List." In: *AJ* 156.3, 102, p. 102. DOI: 10.3847/1538-3881/aad050. arXiv: 1706.00495 [astro-ph.EP] (cit. on p. 84).
Stoughton, Chris et al. (2002). "Sloan Digital Sky Survey: Early Data Release." In: *AJ* 123.1, pp. 485–548. DOI: 10.1086/324741 (cit. on pp. 25, 29, 74).
Suárez, Genaro et al. (2017). "New Low-mass Stars in the 25 Orionis Stellar Group and Orion OB1a Sub-association from SDSS-III/BOSS Spectroscopy." In: *AJ* 154.1, 14, p. 14. DOI: 10.3847/1538-3881/aa733a. arXiv: 1705.02722 [astro-ph.SR] (cit. on p. 54).
Sun, Xudong et al. (2015). "Why Is the Great Solar Active Region 12192 Flare-rich but CME-poor?" In: *APJL* 804.2, L28, p. L28. DOI: 10.1088/2041-8205/804/2/L28. arXiv: 1502.06950 [astro-ph.SR] (cit. on p. 16).
Thalmann, J. K. et al. (2015). "The Confined X-class Flares of Solar Active Region 2192." In: *APJL* 801.2, L23, p. L23. DOI: 10.1088/2041-8205/801/2/L23. arXiv: 1502.05157 [astro-ph.SR] (cit. on pp. 16, 24).
Theissen, Christopher A. et al. (2017). "The Late-Type Extension to MoVeRS (LaTE-MoVeRS): Proper Motion Verified Low-mass Stars and Brown Dwarfs from SDSS, 2MASS, and WISE." In: *AJ* 153.3, 92, p. 92. DOI: 10.3847/1538-3881/153/3/92. arXiv: 1612.05252 [astro-ph.SR] (cit. on p. 84).
Vida, Krisztián, L. Kriskovics, et al. (2016). "Investigating magnetic activity in very stable stellar magnetic fields. Long-term photometric and spectroscopic study of the fully convective M4 dwarf V374 Pegasi." In: *AAP* 590, A11, A11. DOI: 10.1051/0004-6361/201527925. arXiv: 1603.00867 [astro-ph.SR] (cit. on pp. 2, 38).
Vida, Krisztián, Martin Leitzinger, et al. (2019). "The quest for stellar coronal mass ejections in late-type stars. I. Investigating Balmer-line asymmetries of single stars in Virtual Observatory data." In: *AAP* 623, A49, A49. DOI: 10.1051/0004-6361/201834264. arXiv: 1901.04229 [astro-ph.SR] (cit. on pp. 2, 78, 79).
Vourlidas, A. et al. (2010). "Comprehensive Analysis of Coronal Mass Ejection Mass and Energy Properties Over a Full Solar Cycle." In: *APJ* 722.2, pp. 1522–1538. DOI: 10.1088/0004-637X/722/2/1522. arXiv: 1008.3737 [astro-ph.SR] (cit. on p. 14).
Vršnak, B. et al. (2013). "Propagation of Interplanetary Coronal Mass Ejections: The Drag-Based Model." In: *SOLPHYS* 285.1-2, pp. 295–315. DOI: 10.1007/s11207-012-0035-4 (cit. on p. 16).
Watson, C. L., A. A. Henden, and A. Price (2006). "The International Variable Star Index (VSX)." In: *Society for Astronomical Sciences Annual Symposium* 25, p. 47 (cit. on p. 52).

Welsh, B. Y. et al. (2006). "GALEX high time-resolution ultraviolet observations of dMe flare events." In: *AAP* 458.3, pp. 921–930. DOI: 10.1051/0004-6361:20065304. arXiv: astro-ph/0608254 [astro-ph] (cit. on p. 22).

West, Andrew A., Suzanne L. Hawley, John J. Bochanski, et al. (2008). "Constraining the Age-Activity Relation for Cool Stars: The Sloan Digital Sky Survey Data Release 5 Low-Mass Star Spectroscopic Sample." In: *AJ* 135.3, pp. 785–795. DOI: 10.1088/0004-6256/135/3/785. arXiv: 0712.1590 [astro-ph] (cit. on p. 84).

West, Andrew A., Suzanne L. Hawley, Lucianne M. Walkowicz, et al. (2004). "Spectroscopic Properties of Cool Stars in the Sloan Digital Sky Survey: An Analysis of Magnetic Activity and a Search for Subdwarfs." In: *AJ* 128.1, pp. 426–436. DOI: 10.1086/421364. arXiv: astro-ph/0403486 [astro-ph] (cit. on p. 20).

West, Andrew A., Dylan P. Morgan, et al. (2011). "The Sloan Digital Sky Survey Data Release 7 Spectroscopic M Dwarf Catalog. I. Data." In: *AJ* 141.3, 97, p. 97. DOI: 10.1088/0004-6256/141/3/97. arXiv: 1101.1082 [astro-ph.SR] (cit. on pp. 27, 54, 75, 84).

Wiese, WL and JR Fuhr (2009). "Accurate atomic transition probabilities for hydrogen, helium, and lithium." In: *Journal of physical and chemical reference data* 38.3, pp. 565–720 (cit. on p. 69).

Wolff, Sidney C., Ann Merchant Boesgaard, and Theodore Simon (1986). "Activity in F Stars." In: *APJ* 310, p. 360. DOI: 10.1086/164689 (cit. on p. 19).

Wood, Brian E. et al. (2001). "Observational Estimates for the Mass-Loss Rates of α Centauri and Proxima Centauri Using Hubble Space Telescope Lyα Spectra." In: *APJ* 547.1, pp. L49–L52. DOI: 10.1086/318888. arXiv: astro-ph/0011153 [astro-ph] (cit. on p. 21).

Xue, Xiang-Xiang et al. (2014). "The SEGUE K Giant Survey. II. A Catalog of Distance Determinations for the SEGUE K Giants in the Galactic Halo." In: *APJ* 784.2, 170, p. 170. DOI: 10.1088/0004-637X/784/2/170. arXiv: 1211.0549 [astro-ph.GA] (cit. on p. 53).

Yang, Huiqin and Jifeng Liu (2019). "The Flare Catalog and the Flare Activity in the Kepler Mission." In: *APJS* 241.2, 29, p. 29. DOI: 10.3847/1538-4365/ab0d28. arXiv: 1903.01056 [astro-ph.SR] (cit. on p. 22).

Yashiro, Seiji and Nat Gopalswamy (2009). "Statistical relationship between solar flares and coronal mass ejections." In: *Universal Heliophysical Processes*. Ed. by N. Gopalswamy and D. F. Webb. Vol. 257. IAU Symposium, pp. 233–243. DOI: 10.1017/S1743921309029342 (cit. on pp. 2, 15, 23).

Zhang, Z. H. et al. (2010). "Discovery of the first wide L dwarf + giant binary system and eight other ultracool dwarfs in wide binaries." In: *MNRAS* 404.4, pp. 1817–1834. DOI: 10.1111/j.1365-2966.2010.16394.x. arXiv: 1001.3609 [astro-ph.GA] (cit. on p. 84).

Zhong, Jing et al. (2015). "M-giant star candidates identified in LAMOST DR 1." In: *Research in Astronomy and Astrophysics* 15.8, 1154, p. 1154. DOI: 10.1088/1674-4527/15/8/005. arXiv: 1505.07932 [astro-ph.GA] (cit. on p. 84).